DESY–02–039

Leading neutron production in e^+p collisions at HERA

ZEUS Collaboration

Abstract

The production of neutrons carrying at least 20% of the proton beam energy ($x_L > 0.2$) in e^+p collisions has been studied with the ZEUS detector at HERA for a wide range of Q^2, the photon virtuality, from photoproduction to deep inelastic scattering. The neutron-tagged cross section, $ep \to e'Xn$, is measured relative to the inclusive cross section, $ep \to e'X$, thereby reducing the systematic uncertainties. For $x_L > 0.3$, the rate of neutrons in photoproduction is about half of that measured in hadroproduction, which constitutes a clear breaking of factorisation. There is about a 20% rise in the neutron rate between photoproduction and deep inelastic scattering, which may be attributed to absorptive rescattering in the γp system. or $0.64 < x_L < 0.82$, the rate of neutrons is almost independent of the Bjorken scaling variable x and Q^2. However, at lower and higher x_L values, there is a clear but weak dependence on these variables, thus demonstrating the breaking of limiting fragmentation. The neutron-tagged structure function, $F_2^{\mathrm{LN}(3)}(x, Q^2, x_L)$, rises at low values of x in a way similar to that of the inclusive $F_2(x, Q^2)$ of the proton. The total $\gamma\pi$ cross section and the structure function of the pion, $F_2^{\pi}(x_\pi, Q^2)$ where $x_\pi = x/(1 - x_L)$, have been determined using a one-pion-exchange model, up to uncertainties in the normalisation due to the poorly understood pion flux. At fixed Q^2, F_2^{π} has approximately the same x dependence as F_2 of the proton.

The ZEUS Collaboration

S. Chekanov, D. Krakauer, S. Magill, B. Musgrave, A. Pellegrino, J. Repond, R. Yoshida
Argonne National Laboratory, Argonne, Illinois 60439-4815 [n]

M.C.K. Mattingly
Andrews University, Berrien Springs, Michigan 49104-0380

P. Antonioli, G. Bari, M. Basile, L. Bellagamba, D. Boscherini, A. Bruni, G. Bruni, G. Cara Romeo, L. Cifarelli, F. Cindolo, A. Contin, M. Corradi, S. De Pasquale, P. Giusti, G. Iacobucci, G. Levi, A. Margotti, R. Nania, F. Palmonari, A. Pesci, G. Sartorelli, A. Zichichi
University and INFN Bologna, Bologna, Italy [e]

G. Aghuzumtsyan, D. Bartsch, I. Brock, J. Crittenden[1], S. Goers, H. Hartmann, E. Hilger, P. Irrgang, H.-P. Jakob, A. Kappes, U.F. Katz[2], R. Kerger[3], O. Kind, E. Paul, J. Rautenberg[4], R. Renner, H. Schnurbusch, A. Stifutkin, J. Tandler, K.C. Voss,

A. Weber
Physikalisches Institut der Universität Bonn, Bonn, Germany [b]

D.S. Bailey[5], N.H. Brook[5], J.E. Cole, B. Foster, G.P. Heath, H.F. Heath, S. Robins, E. Rodrigues[6], J. Scott, R.J. Tapper, M. Wing
H.H. Wills Physics Laboratory, University of Bristol, Bristol, United Kingdom [m]

M. Capua, A. Mastroberardino, M. Schioppa, G. Susinno
Calabria University, Physics Department and INFN, Cosenza, Italy [e]

J.Y. Kim, Y.K. Kim, J.H. Lee, I.T. Lim, M.Y. Pac[7]
Chonnam National University, Kwangju, Korea [g]

A. Caldwell, M. Helbich,

X. Liu, B. Mellado, S. Paganis, W.B. Schmidke, F. Sciulli
Nevis Laboratories, Columbia University, Irvington on Hudson, New York 10027 [o]

J. Chwastowski, A. Eskreys, J. Figiel, K. Olkiewicz, M.B. Przybycień[8], P. Stopa, L. Zawiejski
Institute of Nuclear Physics, Cracow, Poland [i]

B. Bednarek, I. Grabowska-Bold, K. Jeleń, D. Kisielewska, A.M. Kowal, M. Kowal, T. Kowalski, B. Mindur, M. Przybycień, E. Rulikowska-Zarębska, L. Suszycki, D. Szuba, J. Szuba[9]
Faculty of Physics and Nuclear Techniques, University of Mining and Metallurgy, Cracow, Poland [p]

A. Kotański[10], W. Słomiński[11]
Department of Physics, Jagellonian University, Cracow, Poland

L.A.T. Bauerdick[12], U. Behrens, K. Borras, V. Chiochia, D. Dannheim, M. Derrick[13], G. Drews, J. Fourletova, A. Fox-Murphy, U. Fricke, A. Geiser, F. Goebel, P. Göttlicher[14], O. Gutsche, T. Haas, W. Hain, G.F. Hartner, S. Hillert, U. Kötz, H. Kowalski[15], H. Labes, D. Lelas, B. Löhr, R. Mankel, M. Martínez[12], M. Moritz, D. Notz, I.-A. Pellmann, M.C. Petrucci, A. Polini, U. Schneekloth, F. Selonke[16], B. Surrow[17], H. Wessoleck, R. Wichmann[18], G. Wolf, C. Youngman, W. Zeuner
Deutsches Elektronen-Synchrotron DESY, Hamburg, Germany

A. Lopez-Duran Viani, A. Meyer, S. Schlenstedt
DESY Zeuthen, Zeuthen, Germany

G. Barbagli, E. Gallo, C. Genta, P. G. Pelfer
University and INFN, Florence, Italy [e]

A. Bamberger, A. Benen, N. Coppola, P. Markun, H. Raach, S. Wölfle
Fakultät für Physik der Universität Freiburg i.Br., Freiburg i.Br., Germany [b]

M. Bell, P.J. Bussey, A.T. Doyle, C. Glasman, S. Hanlon, S.W. Lee, A. Lupi, G.J. McCance, D.H. Saxon, I.O. Skillicorn
Department of Physics and Astronomy, University of Glasgow, Glasgow, United Kingdom [m]

I. Gialas
Department of Engineering in Management and Finance, Univ. of Aegean, Greece

B. Bodmann, T. Carli, U. Holm, K. Klimek, N. Krumnack, E. Lohrmann, M. Milite, H. Salehi, S. Stonjek[19], K. Wick, A. Ziegler, Ar. Ziegler
Hamburg University, Institute of Exp. Physics, Hamburg, Germany [b]

C. Collins-Tooth, C. Foudas, R. Gonçalo[6], K.R. Long, F. Metlica, D.B. Miller, A.D. Tapper, R. Walker
Imperial College London, High Energy Nuclear Physics Group, London, United Kingdom [m]

P. Cloth, D. Filges
Forschungszentrum Jülich, Institut für Kernphysik, Jülich, Germany

M. Kuze, K. Nagano, K. Tokushuku[20], S. Yamada, Y. Yamazaki
Institute of Particle and Nuclear Studies, KEK, Tsukuba, Japan [f]

A.N. Barakbaev, E.G. Boos, N.S. Pokrovskiy, B.O. Zhautykov
Institute of Physics and Technology of Ministry of Education and Science of Kazakhstan, Almaty, Kazakhstan

H. Lim, D. Son
Kyungpook National University, Taegu, Korea [g]

F. Barreiro, O. González, L. Labarga, J. del Peso, I. Redondo[21], J. Terrón, M. Vázquez
Departamento de Física Teórica, Universidad Autónoma Madrid,Madrid, Spain [l]

M. Barbi, A. Bertolin, F. Corriveau, A. Ochs, S. Padhi, D.G. Stairs, M. St-Laurent
Department of Physics, McGill University, Montréal, Québec, Canada H3A 2T8 [a]

T. Tsurugai
Meiji Gakuin University, Faculty of General Education, Yokohama, Japan

A. Antonov, V. Bashkirov[22], P. Danilov, B.A. Dolgoshein, D. Gladkov, V. Sosnovtsev, S. Suchkov
Moscow Engineering Physics Institute, Moscow, Russia [j]

R.K. Dementiev, P.F. Ermolov, Yu.A. Golubkov, I.I. Katkov, L.A. Khein, I.A. Korzhavina, V.A. Kuzmin, B.B. Levchenko, O.Yu. Lukina, A.S. Proskuryakov, L.M. Shcheglova, N.N. Vlasov, S.A. Zotkin
Moscow State University, Institute of Nuclear Physics, Moscow, Russia [k]

C. Bokel, J. Engelen, S. Grijpink, E. Koffeman, P. Kooijman, E. Maddox, S. Schagen, E. Tassi, H. Tiecke, N. Tuning, J.J. Velthuis, L. Wiggers, E. de Wolf
NIKHEF and University of Amsterdam, Amsterdam, Netherlands [h]

N. Brümmer, B. Bylsma, L.S. Durkin, J. Gilmore, C.M. Ginsburg, C.L. Kim, T.Y. Ling
Physics Department, Ohio State University, Columbus, Ohio 43210 [n]

S. Boogert, A.M. Cooper-Sarkar, R.C.E. Devenish, J. Ferrando, G. Grzelak, T. Matsushita, M. Rigby, O. Ruske[23], M.R. Sutton, R. Walczak
Department of Physics, University of Oxford, Oxford United Kingdom [m]

R. Brugnera, R. Carlin, F. Dal Corso, S. Dusini, A. Garfagnini, S. Limentani, A. Longhin, A. Parenti, M. Posocco, L. Stanco, M. Turcato
Dipartimento di Fisica dell' Università and INFN, Padova, Italy [e]

L. Adamczyk[24], E.A. Heaphy, B.Y. Oh, P.R.B. Saull[24], J.J. Whitmore[25]
Department of Physics, Pennsylvania State University, University Park, Pennsylvania 16802 [o]

Y. Iga
Polytechnic University, Sagamihara, Japan [f]

G. D'Agostini, G. Marini, A. Nigro
Dipartimento di Fisica, Università 'La Sapienza' and INFN, Rome, Italy [e]

C. Cormack, J.C. Hart, N.A. McCubbin
Rutherford Appleton Laboratory, Chilton, Didcot, Oxon, United Kingdom [m]

C. Heusch
University of California, Santa Cruz, California 95064 [n]

I.H. Park
Seoul National University, Seoul, Korea

N. Pavel
Fachbereich Physik der Universität-Gesamthochschule Siegen, Germany

H. Abramowicz, S. Dagan, A. Gabareen, S. Kananov, A. Kreisel, A. Levy
Raymond and Beverly Sackler Faculty of Exact Sciences, School of Physics, Tel-Aviv University, Tel-Aviv, Israel [d]

T. Abe, T. Fusayasu, T. Kohno, K. Umemori, T. Yamashita
Department of Physics, University of Tokyo, Tokyo, Japan [f]

R. Hamatsu, T. Hirose, M. Inuzuka, S. Kitamura[26], K. Matsuzawa, T. Nishimura
Tokyo Metropolitan University, Deptartment of Physics, Tokyo, Japan [f]

M. Arneodo[27], N. Cartiglia, R. Cirio, M. Costa, M.I. Ferrero, S. Maselli, V. Monaco, C. Peroni, M. Ruspa, R. Sacchi, A. Solano, A. Staiano
Università di Torino, Dipartimento di Fisica Sperimentale and INFN, Torino, Italy [e]

C.-P. Fagerstroem, R. Galea, T. Koop, J.F. Martin, A. Mirea, A. Sabetfakhri
Department of Physics, University of Toronto, Toronto, Ontario, Canada M5S 1A7 [a]

J.M. Butterworth, C. Gwenlan, R. Hall-Wilton, T.W. Jones, J.B. Lane, M.S. Lightwood, J.H. Loizides[28], B.J. West
Physics and Astronomy Department, University College London, London, United Kingdom [m]

J. Ciborowski[29], R. Ciesielski[30], R.J. Nowak, J.M. Pawlak, B. Smalska[31], J. Sztuk[32], T. Tymieniecka[33], A. Ukleja[33], J. Ukleja, J.A. Zakrzewski, A.F. Żarnecki
Warsaw University, Institute of Experimental Physics, Warsaw, Poland [q]

M. Adamus, P. Plucinski
Institute for Nuclear Studies, Warsaw, Poland [q]

Y. Eisenberg, L.K. Gladilin[34], D. Hochman, U. Karshon
Department of Particle Physics, Weizmann Institute, Rehovot, Israel [c]

D. Kçira, S. Lammers, L. Li, D.D. Reeder, A.A. Savin, W.H. Smith
Department of Physics, University of Wisconsin, Madison, Wisconsin 53706 [n]

A. Deshpande, S. Dhawan, V.W. Hughes, P.B. Straub
Department of Physics, Yale University, New Haven, Connecticut 06520-8121 [n]

S. Bhadra, C.D. Catterall, S. Fourletov, M. Khakzad, S. Menary, M. Soares, J. Standage
Department of Physics, York University, Ontario, Canada M3J 1P3 [a]

[1] now at Cornell University, Ithaca/NY, USA
[2] on leave of absence at University of Erlangen-Nürnberg, Germany
[3] now at Ministère de la Culture, de L'Enseignement Supérieur et de la Recherche, Luxembourg
[4] supported by the GIF, contract I-523-13.7/97
[5] PPARC Advanced fellow
[6] supported by the Portuguese Foundation for Science and Technology (FCT)
[7] now at Dongshin University, Naju, Korea
[8] now at Northwestern Univ., Evanston/IL, USA
[9] partly supported by the Israel Science Foundation and the Israel Ministry of Science
[10] supported by the Polish State Committee for Scientific Research, grant no. 2 P03B 09322
[11] member of Dept. of Computer Science, supported by the Polish State Committee for Sci. Res., grant no. 2P03B 06116
[12] now at Fermilab, Batavia/IL, USA
[13] on leave from Argonne National Laboratory, USA
[14] now at DESY group FEB
[15] on leave of absence at Columbia Univ., Nevis Labs., N.Y./USA
[16] retired
[17] now at Brookhaven National Lab., Upton/NY, USA
[18] now at Mobilcom AG, Rendsburg-Büdelsdorf, Germany
[19] supported by NIKHEF, Amsterdam/NL
[20] also at University of Tokyo
[21] now at LPNHE Ecole Polytechnique, Paris, France
[22] now at Loma Linda University, Loma Linda, CA, USA
[23] now at IBM Global Services, Frankfurt/Main, Germany
[24] partly supported by Tel Aviv University
[25] on leave of absence at The National Science Foundation, Arlington, VA/USA
[26] present address: Tokyo Metropolitan University of Health Sciences, Tokyo 116-8551, Japan
[27] also at Università del Piemonte Orientale, Novara, Italy
[28] supported by Argonne National Laboratory, USA
[29] also at Łódź University, Poland
[30] supported by the Polish State Committee for Scientific Research, grant no. 2 P03B 07222
[31] supported by the Polish State Committee for Scientific Research, grant no. 2 P03B 00219
[32] Łódź University, Poland
[33] sup. by Pol. State Com. for Scien. Res., 5 P03B 09820 and by Germ. Fed. Min. for Edu. and Research (BMBF), POL 01/043
[34] on leave from MSU, partly supported by University of Wisconsin via the U.S.-Israel BSF

[a] supported by the Natural Sciences and Engineering Research Council of Canada (NSERC)

[b] supported by the German Federal Ministry for Education and Research (BMBF), under contract numbers HZ1GUA 2, HZ1GUB 0, HZ1PDA 5, HZ1VFA 5

[c] supported by the MINERVA Gesellschaft für Forschung GmbH, the Israel Science Foundation, the U.S.-Israel Binational Science Foundation, the Israel Ministry of Science and the Benozyio Center for High Energy Physics

[d] supported by the German-Israeli Foundation, the Israel Science Foundation, and by the Israel Ministry of Science

[e] supported by the Italian National Institute for Nuclear Physics (INFN)

[f] supported by the Japanese Ministry of Education, Science and Culture (the Monbusho) and its grants for Scientific Research

[g] supported by the Korean Ministry of Education and Korea Science and Engineering Foundation

[h] supported by the Netherlands Foundation for Research on Matter (FOM)

[i] supported by the Polish State Committee for Scientific Research, grant no. 620/E-77/SPUB-M/DESY/P-03/DZ 247/2000-2002

[j] partially supported by the German Federal Ministry for Education and Research (BMBF)

[k] supported by the Fund for Fundamental Research of Russian Ministry for Science and Education and by the German Federal Ministry for Education and Research (BMBF)

[l] supported by the Spanish Ministry of Education and Science through funds provided by CICYT

[m] supported by the Particle Physics and Astronomy Research Council, UK

[n] supported by the US Department of Energy

[o] supported by the US National Science Foundation

[p] supported by the Polish State Committee for Scientific Research, grant no. 112/E-356/SPUB-M/DESY/P-03/DZ 301/2000-2002, 2 P03B 13922

[q] supported by the Polish State Committee for Scientific Research, grant no. 115/E-343/SPUB-M/DESY/P-03/DZ 121/2001-2002, 2 P03B 07022

1 Introduction

Leading baryon production in a process with a hard scale provides a probe of the relationship between the quantum chromodynamics (QCD) of quarks and gluons and the strong interaction of hadrons. The leading baryons are produced with small transverse momentum (p_T), guaranteeing the presence of a soft process with its related long-range correlations. The hard scale can come from large photon virtuality (Q^2) in deep inelastic scattering (DIS), or high transverse energy (E_T) in photoproduction. The observation of events with neutrons or protons carrying a large fraction (x_L) of the incident proton beam energy in positron-proton (e^+p) scattering at HERA [1–6] has led to renewed interest in the QCD evolution and factorisation properties of proton fragmentation to leading baryons in deep inelastic scattering [7–11].

A non-perturbative approach to the strong interaction is needed to calculate the production rates of leading baryons. Some theoretical models retain the QCD building blocks, quarks and gluons, as fundamental entities but add non-perturbative elements, such as soft color interactions [12]. Another approach interprets the production of forward baryons in terms of the exchange of virtual particles [13–23], which accounts for charge-exchange processes ($p \to n$) in hadronic interactions [24–33]. In leading neutron production, the large diffractive peak in the cross section, which is observed in leading proton production [4,5], is absent. Although leading neutrons can be produced indirectly through the production and decay of heavy baryons or through the fragmentation of diffractively dissociating protons, direct production dominates [3]. In the language of particle exchange models, isovector exchange (π, ρ and a_2) is required for direct neutron production, and isoscalar exchange (f and ω) is absent. The production mechanism of leading neutrons is therefore simpler than that of protons and, since the cross section for π exchange is much larger than that for ρ or a_2 exchange, it is predominantly the structure of the pion is probed by the hard process [22].

Comparisons between cross sections for the production of particles in the fragmentation region of a target nucleon provide tests of the concepts of vertex factorisation and limiting fragmentation. Factorisation tests involve comparing semi-inclusive rates, normalised to the respective total cross section, to study whether particle production from a given target is independent of the nature of the incident projectile. Thus, for example, data from γp interactions may be compared with those from pp collisions. The limiting-fragmentation hypothesis [10] states that, in the high-energy limit, the momentum distribution of fragments becomes independent of the incident projectile energy. This has been verified in hadronic interactions [34]. It has not been extensively studied for produced baryons in electroproduction. In this case, the fragmentation spectra should be studied as a function of Q^2 and the photon-proton centre-of-mass energy, W [11].

In electroproduction, the size of the incident projectile (the virtual photon) can be varied. At $Q^2 = 0$, the photon has a typical hadronic size; as Q^2 increases, the photon size decreases. Hence, absorptive rescattering of the produced baryon is expected to decrease and become independent of Q^2 at high Q^2 [35,36]. Such effects, if x_L or p_T dependent, lead to an apparent failure of factorisation and limiting fragmentation for low values of Q^2.

This paper reports studies of the production of leading neutrons using the ZEUS detector and its forward neutron calorimeter (FNC). Leading neutron production can be measured precisely by determining the neutron-tagged cross sections relative to the inclusive ep cross section, which has been measured with high accuracy [37]. The study of ratios reduces the systematic uncertainties arising from both theoretical and experimental sources.

The paper is organized as follows: the kinematics of leading neutron production is defined in Section 2; the one-pion-exchange model is reviewed in Section 3; the detector, the reconstruction of the kinematic variables and the experimental conditions are described in Section 4; the event selection is discussed in Section 5; in Section 6, the advantages of analysing the data using the ratio of the neutron-tagged to the inclusive cross section are outlined; systematic uncertainties are discussed in Section 7. The general features of the neutron energy spectra and the ratio of leading-neutron to total cross sections are discussed in Section 8, where the factorisation and limiting-fragmentation properties of the data are investigated and an estimate of absorptive effects is made. The neutron-tagged structure function is discussed in Section 9. The data are analysed in Section 10 in terms of a one-pion-exchange ansatz and the pion structure function, F_2^π, is extracted up to uncertainties in the normalisation due to the lack of knowledge of the pion flux; theoretical models are compared to F_2^π. Section 11 summarizes the results.

2 Kinematics and cross sections

Figure 1 shows a Mandelstam diagram of semi-inclusive leading neutron production in ep collisions. Four kinematic variables are needed to describe the interaction $ep \to e'Xn$. They are defined in terms of the four-momenta k, P, k' and N, respectively, of the incoming and outgoing particles e, p, e' and n. Two variables are chosen from the Lorentz invariants used in inclusive studies: $Q^2 = -q^2 = -(k-k')^2$, the virtuality of the exchanged photon; $x = Q^2/(2P\cdot q)$, the Bjorken scaling variable; $y = q\cdot P/(k\cdot P) \simeq Q^2/(sx)$, the inelasticity in the proton rest frame; and $W^2 = (P+k-k')^2 = m_p^2 + Q^2(1-x)/x$, the squared mass of the produced hadronic system. In these equations, m_p is the mass of the proton and $\sqrt{s} = 300$ GeV is the ep centre-of-momentum-system (cms) energy.

Two further variables are required to describe the leading neutron. They can be chosen as the laboratory production angle of the neutron, θ_n, and the energy fraction carried by the produced neutron,

$$x_L = \frac{N\cdot k}{P\cdot k} \simeq \frac{E_n}{E_p},$$

where E_p is the proton beam energy and E_n is the neutron energy. The transverse momentum of the neutron is given by $p_T \simeq x_L E_p \theta_n$. In terms of these variables, the squared four-momentum transfer from the target proton is

$$t = (P-N)^2 \simeq -\frac{p_T^2}{x_L} - t_0,$$

where t_0 is the minimum kinematically allowed value of $|t|$ for a given x_L

$$t_0(x_L) = \frac{(1-x_L)}{x_L}\left(m_n^2 - x_L m_p^2\right) \simeq \frac{(1-x_L)^2}{x_L} m_p^2,$$

and m_n is the mass of the neutron.

The differential cross section for inclusive $ep \to e'X$ scattering is written in terms of the proton structure function, $F_2(x, Q^2)$, as

$$\frac{d^2\sigma^{ep\to e'X}}{dx\, dQ^2} = \mathcal{K} F_2(x, Q^2)(1+\delta), \tag{1}$$

where

$$\mathcal{K} = \frac{4\pi\alpha^2}{xQ^4}\left(1 - y + \frac{y^2}{2}\right)$$

and δ is the correction to the Born cross section for photon radiation, Z^0 exchange and the longitudinal structure function, F_L. In analogy to this, the differential cross section for leading neutron production, $ep \to e'Xn$, is written as

$$\frac{d^4\sigma^{ep\to e'Xn}}{dx\, dQ^2\, dx_L\, dp_T} = \mathcal{K} F_2^{\mathrm{LN}(4)}(x, Q^2, x_L, p_T)(1+\delta_{\mathrm{LN}}). \tag{2}$$

The term δ_{LN} is analogous to δ, but for the case of leading neutron production.

In the results presented here, θ_n (and hence p_T^2 and t) is not measured. Integrating Eq. (2) up to the maximum experimentally accessible angle, $\theta_n^{\max}$, corresponding to a $p_T^{\max}$ which varies with x_L, leads to

$$\begin{aligned} \frac{d^3\sigma^{ep\to e'Xn}}{dx\, dQ^2\, dx_L} &\equiv \int_0^{p_T^{\max}} \frac{d^4\sigma^{ep\to e'Xn}}{dx\, dQ^2\, dx_L\, dp_T} dp_T \\ &= \mathcal{K} F_2^{\mathrm{LN}(3)}(x, Q^2, x_L)(1+\delta_{\mathrm{LN}}) \end{aligned} \tag{3}$$

where

$$F_2^{\mathrm{LN}(3)}(x, Q^2, x_L) \equiv \int_0^{p_T^{\max}} F_2^{\mathrm{LN}(4)}(x, Q^2, x_L, p_T) dp_T$$

is the neutron-tagged structure function integrated over the measured range in θ_n.

It is sometimes more convenient to discuss the results in terms of cross sections rather than structure functions. At low x, where $W^2 \simeq Q^2/x$, the following expressions are valid:

$$\sigma_{\mathrm{tot}}^{\gamma^* p}(W, Q^2) = \frac{4\pi^2\alpha}{Q^2} F_2(x, Q^2) \tag{4}$$

$$\begin{aligned} \frac{d\sigma^{\gamma^* p\to Xn}(W, Q^2)}{dx_L} &\equiv \int_0^{p_T^{\max}} \frac{d^2\sigma^{\gamma^* p\to Xn}(W, Q^2)}{dx_L\, dp_T} dp_T \\ &= \frac{4\pi^2\alpha}{Q^2} F_2^{\mathrm{LN}(3)}(x, Q^2, x_L), \end{aligned} \tag{5}$$

where $\sigma_{\mathrm{tot}}^{\gamma^* p}$ is the total virtual photon-proton cross section and $d^2\sigma^{\gamma^* p\to Xn}(W, Q^2)/dx_L dp_T$ is the differential cross section for leading neutron production in a virtual photon-proton collision.

3 One-pion-exchange model

A successful description of the available data [24–33] on charge-exchange processes ($p \to n$) in hadron-hadron interactions has been obtained using the exchange of virtual particles with the quantum numbers of the π, ρ, and a_2 mesons [13–17, 20, 21]. In such processes, the pion, due to its small mass, dominates the $p \to n$ transition amplitude, with its relative contribution increasing as $|t|$ decreases. In contrast to the nucleon, whose partonic structure has been probed directly in deep inelastic scattering, the structure of mesons has been studied only indirectly using hadron-hadron collisions. For the pion, the data from πp interactions yielding prompt photons [38, 39], high-mass muon pairs [40–43] and dijets [44] in the final state have given important information. However, these results are mostly sensitive to the high-x, or valence, structure of the pion: the sea-quark and gluon content of the pion at low x have not yet been measured. The HERA leading neutron data offer an opportunity to probe this low-x structure via the diagram shown in Fig. 1. In the one-pion-exchange (OPE) approximation, the cross section for hadroproduction, $hp \to Xn$, can be written as

$$\frac{d\sigma_{hp\to Xn}}{dx_L\, dt} = f_{\pi/p}(x_L, t)\sigma_{\rm tot}^{h\pi}(s') \tag{6}$$

where the flux factor, $f_{\pi/p}(x_L, t)$, describes the splitting of a proton into a πn system, $s' = s(1 - x_L)$, where s' and s are the squares of the cms energy for the $h\pi$ and hp systems, respectively. Charge-exchange processes at the ISR [27, 28] and Fermilab [29, 30] are well described by such an expression with [15, 16]

$$f_{\pi/p}(x_L, t) = \frac{1}{4\pi}\frac{2g^2_{\pi pp}}{4\pi}\frac{-t}{(t-m^2_\pi)^2}(1-x_L)^{1-2\alpha_\pi(t)}\left[F(x_L, t)\right]^2, \tag{7}$$

where $g^2_{\pi pp}/(4\pi) = 14.5$ is the $\pi^0 pp$ coupling constant and $\alpha_\pi(t) = \alpha' t$ with $\alpha' = 1$ GeV^{-2}. The form-factor $F(x_L, t)$ parametrises the distribution of the pion cloud in the proton and accounts for final-state rescattering of the neutron.

For the hadronic charge-exchange experiments, a good description of most of the $pn \to Xp$ data [26] is obtained using the Bishari [15] flux, which corresponds to Eq. (7) with $F(x_L, t) = 1$. In this case,

$$f_{\rm eff}(x_L, t) = \frac{1}{4\pi}\frac{2g^2_{\pi pp}}{4\pi}\frac{-t}{(t-m^2_\pi)^2}(1-x_L)^{1-2\alpha_\pi(t)}. \tag{8}$$

The flux-factor $f_{\rm eff}$ can therefore be interpreted as an *effective* pion flux that takes into account processes that occur in hadronic charge-exchange processes, such as absorption (Section 10.1), non-pion exchange and off-mass-shell effects.

4 HERA and the ZEUS detector

During 1995–97, the HERA collider operated at $\sqrt{s} \sim 300$ GeV with positrons of $E_e = 27.5$ GeV colliding with protons of $E_p = 820$ GeV. In addition to the 175 ep colliding bunches, 21 unpaired bunches of protons or positrons allowed the determination of beam–related backgrounds.

4.1 The ZEUS detector

The ZEUS central detector is described in detail elsewhere [45]. Here the main components used in the present analysis are described briefly. The central tracking detector (CTD) [46], positioned in a 1.43 T solenoidal magnetic field, was used to establish an interaction vertex with a typical resolution along (transverse to) the beam direction[1] of 0.4 (0.1) cm.

The high-resolution uranium-scintillator calorimeter (CAL) [47] consists of three parts: the forward (FCAL), the barrel (BCAL) and the rear (RCAL) calorimeters. Each part is subdivided transversely into towers and longitudinally into one electromagnetic section (EMC) and either one (in RCAL) or two (in FCAL and BCAL) hadronic sections (HAC). The smallest subdivision of the calorimeter is called a cell. The CAL relative energy resolutions, as measured under test-beam conditions, are $\sigma(E)/E = 0.18/\sqrt{E}$ for electrons and $\sigma(E)/E = 0.35/\sqrt{E}$ for hadrons (E in GeV).

In addition to the CAL, two small electromagnetic sampling calorimeters, situated beside the beam pipe, were used to measure the scattered positron. The beam pipe calorimeter (BPC) [48] was located at $Z = -2.9$ m from the interaction point, and the LUMI calorimeter [49], which forms part of the ZEUS system for monitoring the luminosity, was located at $Z = -35$ m. These additional calorimeters had relative energy resolutions of $\sigma(E)/E = 0.18/\sqrt{E}$.

4.2 The forward neutron calorimeter

A forward neutron calorimeter (FNC) was installed in 1995 [50] in the HERA tunnel at $Z = +106$ m and at zero degrees from the incoming proton direction. Figure 2 shows the layout in relation to the six stations (S1–S6) of the leading proton spectrometer (LPS).

The structure of the calorimeter is shown in Fig. 3. It is a finely segmented, compensating, sampling calorimeter with 134 layers of 1.25 cm-thick lead plates as absorber and 0.26 cm-thick scintillator plates as the active material. The scintillator is read out on each side with wavelength-shifting light guides coupled to photomultiplier tubes (PMTs). It is segmented longitudinally into a front section, seven interaction-lengths deep, and a rear section, three interaction-lengths deep. The front section is divided vertically into 14 towers, each 5 cm high. The relative energy resolution for hadrons, as measured in a test beam, was $\sigma/E = 0.65/\sqrt{E}$. As seen in Fig. 3, the FNC completely surrounds the proton beam, which passes through a 10×10 cm^2 hole in towers 11 and 12. Three planes of scintillation counters, each $70 \times 50 \times 2$ cm^3, are located 70, 78, and 199 cm in front of the calorimeter. These counters completely cover the bottom front face of the calorimeter and are used to identify charged particles and so reject neutrons that interact in front of the FNC in inactive material such as magnet support structures, the beam-pipe wall and the mechanics and supports of the LPS.

The HERA magnet apertures limit the FNC acceptance to neutrons with production angles less than $\theta_n^{\max} = 0.8$ mrad, that is to transverse momenta $p_T^{\max} = E_n \theta_n^{\max} = 0.656\, x_L$ GeV. Only about one quarter of the azimuth extends to $\theta_n^{\max}$, as can be seen from the outline of the aperture shown in Fig. 4. The overall acceptance of the FNC, taking account of beam-line geometry, inactive material, beam tilt and angular spread, as well as the angular distribution of the neutrons, is ∼20% at low x_L, where the p_T range covered is small, but increases monotonically,

---

[1] The ZEUS coordinate system is a right-handed Cartesian system, with the Z axis pointing in the proton beam direction, and the X axis pointing left towards the centre of HERA. The coordinate origin is at the nominal interaction point. The polar angle θ is defined with respect to the positive Z-direction. The pseudorapidity, η, is given by $-\ln(\tan\frac{\theta}{2})$.

exceeding 30% at high x_L, as seen in Table 1. The dominant influence on these values is the lack of complete azimuthal coverage illustrated in Fig. 4. The kinematic region in t and p_T^2 covered by the FNC as a function of x_L is shown in Fig. 5(a) and (b), respectively. Although the acceptance extends to $p_T^2 \simeq 0.4$ GeV^2, the mean value of p_T^2 for the accepted data is less than 0.05 GeV^2 [3].

Charged particles produced at small angles and energies $\lesssim 450$ GeV are swept away vertically by the HERA bending magnets. Higher-energy positively charged particles in the energy range from about 450 GeV to about 600 GeV are bent into the top towers above the beam pipe. Neutrons are easily distinguished from protons, since the latter deposit most of their energy in the top four towers of the FNC. Protons with energies $\gtrsim 600$ GeV do not exit the beam pipe in the vicinity of the FNC.

Photons, which populate only the lower x_L range of the data, are separated from neutrons using the energy-weighted root-mean-square vertical width of the showers. After this separation, the correction for photon contamination in the final neutron sample is negligible.

Timing information from the FNC was also used to eliminate backgrounds. One source of background is due to the random overlap of energetic neutrons from proton beam-gas interactions with genuine DIS events. The rate of FNC energy deposits above 400 GeV was monitored and, from comparisons with the bunch-crossing rate, the overlap was estimated to be less than a few percent [1] and was ignored. This background was also checked using randomly triggered events and events with an energy deposit in the FNC greater than 1000 GeV.

The calibration and monitoring [51] of the FNC followed the methods developed for the test calorimeters [1, 52]. The gain of each PMT was obtained by scanning the FNC with a ^{60}Co radioactive source. Changes in gain during data taking were monitored using energy deposits from interactions of the HERA proton beam with residual gas in the beam pipe. The overall energy scale was set from the kinematic end-point of 820 GeV by fitting data from proton beam-gas interactions with energy greater than 600 GeV to the shape of the spectrum expected from one-pion exchange [15, 53]. The accuracy (± 2%) of the energy-scale determination was limited by the uncertainty of the shape of the beam-gas spectrum at the kinematic endpoint.

4.3 Experimental conditions

The data were taken in three ranges of Q^2. The first, consisting of photoproduced events where the scattered positron was detected in the LUMI calorimeter, is characterised by photon virtuality $Q^2 < 0.02$ GeV^2; the second, consisting of intermediate-Q^2 events where the scattered positron was detected in the BPC detector, is characterised by photon virtuality $0.1 < Q^2 < 0.74$ GeV^2; and the third, originating from deep inelastic scattering, where the scattered positron was detected in the CAL, is characterised by photon virtuality $Q^2 > 4$ GeV^2. The three samples are denoted, respectively, as PHP, intermediate-Q^2 and DIS.

The data for the PHP sample come from four short dedicated runs in 1996, taken with a minimum-bias trigger, and correspond to an integrated luminosity of 49 nb^{-1} covering the full x_L range. For $x_L \gtrsim 0.5$, 2 pb^{-1} of data were also taken in 1995 with the FNC included in the trigger. The other data samples were taken in 1995-97, and correspond to integrated luminosities of approximately 14 pb^{-1} for the intermediate-Q^2 and 41 pb^{-1} for the DIS samples.

4.4 Trigger conditions

A three-level trigger was used to select the events. The trigger decision relied primarily on the energies deposited in the CAL, the BPC or the LUMI and was based on electromagnetic energy, total transverse energy and missing transverse momentum. CAL timing cuts were used to reject beam-gas interactions and cosmic rays. No FNC requirements were placed on the trigger, except for part of the PHP sample in which events were triggered by energy deposits in the FNC, LUMI and RCAL. This data sample is useful only for $x_L > 0.52$, where the FNC triggering efficiency is better than 50%. The efficiency is 100% for $x_L \gtrsim 0.7$.

4.5 Reconstruction of kinematic variables

The reconstruction of the lepton variables depends on the device in which the scattered positron was detected. The LUMI measures only the energy and the horizontal deflection of the scattered positron: such particles have scattering angles $\theta_e < 6$ mrad, so that the virtuality of the exchanged photon is limited to $Q^2 < 0.02$ GeV^2, with a mean value $\approx 2 \cdot 10^{-3}$ GeV^2. In the BPC, both the energy and the position of the scattered positron were measured, and the kinematic variables estimated from these measurements [48]. When the positron was detected in the CAL, the double angle (DA) method [54] was used to reconstruct the DIS variables from the scattering angles of the positron and the hadronic system. The latter was determined from the hadronic energy flow measured in the CAL.

The impact position of the neutron on the FNC was not measured with sufficient accuracy to be used event-by-event. All distributions were obtained by integrating over the angle of the produced neutrons up to the maximum observable angle, $\theta_n^{\max}= 0.8$ mrad.

5 Data selection

The PHP, intermediate-Q^2 and DIS samples were first selected without any FNC requirement. The PHP events had to satisfy criteria on the CAL energy deposits or CTD tracks [49] and required a scattered positron in the LUMI detector with $10 < E'_e < 18$ GeV, where E'_e is the energy of the scattered positron. The intermediate-Q^2 and DIS events had to satisfy $35 \leq \delta \leq 65$ GeV, where $\delta = \sum(E - P_Z) = \sum E(1 - \cos\theta)$, with the sum running over all calorimeter cells; E and θ are the energy and polar angle, respectively, for a CAL cell. For the intermediate-Q^2 data, δ also includes $2E'_e$. The events also had to have a reconstructed vertex with $-40 < Z < 100$ cm for the intermediate-Q^2 sample and $|Z| < 40$ cm for the DIS events. The intermediate-Q^2 events had to have a scattered positron of $E'_e > 7$ GeV within the fiducial volume of the BPC [48], while the DIS events had to have a scattered positron of $E'_e > 10$ GeV within the fiducial volume of the CAL [37, 55].

The final event selection required, in addition to a good LUMI, BPC or CAL positron as defined above, a good FNC neutron candidate satisfying the following conditions:

- between 164 GeV and 820 GeV ($0.2 < x_L < 1.0$) of deposited energy in the FNC;

- energy less than that corresponding to one minimum-ionising particle deposited in the counter farthest[2] from the front of the FNC, to reject neutrons that shower in front of the calorimeter;
- no signal from the veto counter consistent with a shower from a previous bunch to reject pile-up energy deposits;
- the maximum energy deposit should be in towers 6-9 in the bottom front section of the FNC, to reject protons that are bent into the top towers by the vertical bending-magnets in the proton beam line;
- a shower with both energy and vertical width consistent with that of a hadron, to reject electromagnetic energy deposits[3].

The final neutron-tagged sample consisted of 912 PHP, 8168 intermediate-Q^2 and 60102 DIS events selected from 56960, 100599 and 642015 inclusive events, respectively.

The data were divided into x_L bins in the range $0.2 < x_L < 1.0$, as shown in Table 1. In each bin, the acceptance extends from 0 to 0.8 mrad in neutron production angle, representing a p_T range from 0 to $0.656\,x_L$ GeV.

Different binnings were used for the three data sets. For the PHP data, a single bin was chosen with $Q^2 < 0.02$ GeV^2 and $0.345 < y < 0.636$, corresponding to a W range of $176 < W < 240$ GeV with a mean $< W > = 209$ GeV. For the intermediate-Q^2 data ($0.1 < Q^2 < 0.74$ GeV^2), the same 34 bins were used as for the ZEUS inclusive $\gamma^* p$ cross-section measurements [48]. For the DIS data ($Q^2 > 4$ GeV^2), 25 bins were used, as shown in Appendix I.

6 The ratio method

To minimise systematic uncertainties, it is advantageous to use the ratio of cross sections rather than the absolute cross sections themselves. The primary measurement, the fraction of events with a leading neutron, is experimentally robust: a luminosity measurement is not required; uncertainties due both to the finite acceptance of the central calorimeter and to triggering inefficiencies are minimised; accurate Monte Carlo modeling of the inclusive hadronic final state is not needed; and the effects of radiative corrections are reduced.

The measured events were binned in Q^2. Depending on the Q^2 region, the events were further binned in x or y. The ratio $r(x, Q^2, x_L)$ is defined as

$$r(x, Q^2, x_L) = \frac{d^3\sigma^{ep\to e'Xn}/dx\, dQ^2\, dx_L}{d^2\sigma^{ep\to e'X}/dx\, dQ^2}\Delta x_L = \frac{n_{\rm obs}(x, Q^2, x_L)}{A(x_L) N_{\rm obs}(x, Q^2)}, \tag{9}$$

where $N_{\rm obs}(x, Q^2)$ is the number of events observed in a bin of (x, Q^2) and $n_{\rm obs}(x, Q^2, x_L)$ is that subset of events with a neutron in an x_L bin of width Δx_L; $A(x_L)$ is the acceptance and reconstruction efficiency for leading neutrons and is discussed in the next section.

---

[2] The farthest counter, 199 cm from the FNC, was chosen to minimise backsplash (albedo) corrections.

[3] This cut is possible since the two-dimensional distribution of energy and shower width shows a clear separation between the wide, high-energy hadronic showers and narrower lower-energy deposits arising from photon-induced showers.

Inspection of Eqs. (1), (3) and (9) shows that, after appropriate bin centering,

$$F_2^{\mathrm{LN}(3)}(x,Q^2,x_L)=\frac{r(x,Q^2,x_L)}{\Delta x_L}F_2(x,Q^2)(1+\Delta), \tag{10}$$

where

$$\Delta \simeq \delta - \delta_{\mathrm{LN}} - \delta_{\mathrm{det}}.$$

The additional correction term, δ_{det}, is the difference between the acceptance of the main detector for all events and for the subset of events with a leading neutron. The overall correction, Δ, is small and was neglected (see Section 7.3).

Equation (10) can be expressed in terms of cross sections by using Eqs. (4) and (5):

$$\frac{d\sigma^{\gamma^* p\to Xn}(W,Q^2)}{dx_L}=\frac{r(W,Q^2,x_L)}{\Delta x_L}\sigma_{\mathrm{tot}}^{\gamma^* p}(W,Q^2). \tag{11}$$

This equation is also valid for photoproduction (Q^2=0). It is evident from Eq. (9) that, within an (x, Q^2) bin, r is the ratio of the cross section for producing a leading neutron with $\theta_n < \theta_n^{\max}$ in a given x_L bin to the total cross section.

7 Corrections and systematic uncertainties

7.1 Acceptance and corrections

For the most part, trigger inefficiencies and acceptance uncertainties in the main ZEUS detector are unimportant for the present analysis since ratios of FNC-tagged events to inclusive events are measured. The observed distributions integrated over the (x,Q^2) plane are not a faithful reproduction the true distributions because of varying trigger configurations and finite acceptances. Therefore, when integrated distributions were studied, the events were weighted, bin-by-bin, by the inclusive cross section, to produce the correct Q^2 and x (or y) distributions. Since the ratio of the neutron-tagged sample to the inclusive sample is not strongly dependent on x or Q^2 (see below), this weighting procedure does not significantly change the shape of any of the distributions of the ratio. However, the statistical uncertainty is increased since low-Q^2 events are under-represented in comparison to high-Q^2 events.

The intermediate-Q^2 and DIS data, triggered by the scattered positron, have a trigger efficiency that is independent of the details of the final state. However, the photoproduction data must also be corrected for the CAL trigger efficiency, which is dependent on the final state. For example, exclusive vector meson production, $ep \to eVp$, has a low trigger efficiency and no neutrons in the final state. As a result, the measured fraction of events tagged with a leading neutron for photoproduction must be corrected downwards. A study of each exclusive final state and its corresponding trigger efficiency showed that the measured fraction of tagged events in photoproduction should be reduced by $(5 \pm 2.5)\%$. This reduction was applied to the photoproduction data presented in this paper.

The acceptance and reconstruction efficiency, $A(x_L)$, of the FNC was obtained using the full simulation of the ZEUS detector based on GEANT 3.13 [56]. The simulation includes the effect of inactive material along the neutron path. The tilt ($\lesssim 70\,\mu$rad in X and Y, but varying from year to year) and divergence (≈ 70 (100) μrad in the X (Y) direction) of the proton beam were also simulated.

The relative uncertainty on the absolute energy scale of the FNC is ±2% [51]. This introduces the normalisation uncertainties shown in Table 1.

Because of the poor position resolution of the FNC, the angular distribution of the neutrons could not be measured directly. Instead, it was constrained by the distribution of measured X positions of the neutrons. The X position of energy deposits in the FNC was determined from the ratio of pulse heights in the two readout channels. For the 1995 data taking, the corresponding rms resolution was 3.2 cm. The resolution degraded in subsequent years because of radiation damage to the scintillator. For fixed x_L, the p_T^2 distribution was expressed as

$$\frac{dN}{dp_T^2} \propto e^{-b(x_L)p_T^2}. \tag{12}$$

The slope b that best represents the data was determined by binning the X-position data in x_L and comparing it to the Monte Carlo expectation for different b slopes. The results for the 1995 DIS data set, given in Table 2 and shown in Fig. 6, indicate that the exponential p_T^2 slope for neutron production rises with increasing x_L and may be parameterised by $b(x_L) = (16.3\ x_L - 4.25)$ GeV^{-2}, as indicated by the solid line (for $x_L < 0.26$, $b = 0$ was used for the the acceptance corrections). Also shown in Fig. 6, as the dashed curve, is the slope parameter resulting from the effective OPE flux of Eq. (8). The predicted slopes are in reasonable accord with the data.

The polar-angle acceptance of the FNC extends from 0 to 0.8 mrad with an azimuthal acceptance shown in Fig. 4. All of the results presented in this paper have been corrected for this azimuthal acceptance. Since $p_T^{\max} = 0.656\, x_L$ GeV, the sensitivity of the acceptance to the b slope decreases rapidly as x_L decreases. As a systematic check, the above value of $b(x_L)$ was varied by ±2 GeV^{-2}, which is the approximate uncertainty in b. The uncertainty on the acceptance reaches 6% at the highest x_L values. The acceptances and their uncertainties, which are highly correlated between all of the bins, are summarised in Table 1.

7.2 Systematic uncertainties

The corrections applied to the acceptance lead to normalisation uncertainties. The largest corrections and their typical values and uncertainties are:

- the increased acceptance of the FNC when the LPS is not inserted into the beam, since less material is present ($-5 \pm 1\%$);
- the veto cut, which avoids pile-up effects but removes events that should have been counted ($+7 \pm 2\%$);
- shower albedo from the face of the FNC, which triggers the veto counters and eliminates good events ($+1.5 \pm 1\%$);
- noise in the veto counters associated with the beam ($+3 \pm 1.5\%$);

- veto-counter inefficiency ($-1.5 \pm 1.5\%$);
- the random overlap of beam-gas events with *ep* interactions ($-2.4 \pm 0.2\%$).

The total normalisation uncertainty for the intermediate-Q^2 and DIS data is $\pm 4\%$. The corresponding uncertainty for the PHP data is $\pm 5\%$, which is highly correlated with the DIS uncertainty.

The photoproduction data taken with the FNC trigger were corrected for the trigger inefficiency and were used only for $x_L > 0.52$, the region where the trigger efficiency is above 50%. In this region, they were normalised to the data collected without the FNC-trigger requirement. This leads to an additional normalisation uncertainty for these data of $\pm 4\%$.

7.3 Relative corrections

The relative-correction term, Δ, of Eq. (10) accounts for differences in the corrections for the neutron-tagged and inclusive samples. Only the difference between the radiative correction for the neutron-tagged sample and that for the inclusive sample, ($\delta - \delta_{\rm LN}$, is relevant in this analysis[4]. The program HECTOR [57], which provides a leading-logarithmic estimate of the radiative correction to the Born term in *ep* scattering, was used to calculate the relative-correction term by modeling inclusive neutron production at large x_L via one-pion exchange. The difference in the neutron-tagged and inclusive correction terms increases with x and x_L, but remains small throughout most of the kinematic region, reaching (3-4)% at $x = 0.06$ for $x_L \gtrsim 0.9$ and at $x = 0.1$ for $x_L \gtrsim 0.8$.

The final term in Δ is due to the correction factor, $\delta_{\rm det}$, which accounts for the differences in the central-detector acceptance, migrations and bin-centering for all events and for those events with a tagged neutron.

Since Δ is smaller than the overall systematic uncertainties of the FNC, it is neglected in the present analysis.

8 General characteristics of the data

8.1 Neutron energy spectra

The neutron yields in bins of x_L and Q^2 are given in Table 3 for the three data samples. The data are corrected for the azimuthal acceptance and are integrated over production angles $0 < \theta_n < \theta_n^{\rm max}$, where $\theta_n^{\rm max} = 0.8$ mrad. As discussed earlier, this fixed angular range corresponds to a p_T range which is x_L dependent. The spectra are normalised to the measured number of events in the same (x, Q^2) bin but without the leading-neutron requirement. Modifying Eq. (9) to take corrections into account yields

$$r(x, Q^2, x_L) \equiv \frac{1}{A(x_L)} \frac{\sum_x \sum_{Q^2} n_{\rm corr}(x, Q^2, x_L)}{\sum_x \sum_{Q^2} N_{\rm corr}(x, Q^2)},$$

---

[4] Possible effects due to the longitudinal structure function and Z^0 exchange are also assumed to be negligible.

where the subscript indicates that the observed number of events has been corrected bin by bin for the effect of the trigger configurations discussed in Section 7. The sum is over the chosen range of Q^2 and all measured bins of x in that range.

Figure 7(a) shows the x_L spectra, as dr/dx_L, for the PHP, intermediate-Q^2 and DIS regions. Between 5% and 10% of the inclusive events have a leading neutron in the measured kinematic range. The ratios are similar in shape for these three kinematic regions, although the fractional yield of neutrons slowly increases with Q^2. The neutron spectra increase slowly with x_L (mostly due to the increased p_T acceptance), reach a broad peak near $x_L = 0.75$, and then rapidly decrease to zero at $x_L = 1$. The neutron rate increases by about 20% between the PHP and DIS data.

Figure 7(b) shows the DIS neutron spectra in three bins of Q^2. Although, for $x_L < 0.8$, the high-Q^2 data tend to lie above the low-Q^2 data, the increase in neutron yield with Q^2 is much less pronounced than that seen in Fig. 7(a). In the region $0.64 < x_L < 0.82$, the neutron yield in DIS is approximately independent of Q^2. For the highest-x_L points, the high-Q^2 data lie below the low-Q^2 data.

8.2 Determination of $\sigma^{\gamma p \to Xn}$

Figure 8(a) shows the differential cross section, $d\sigma^{\mathrm{LN}}/dx_L$, for the photoproduction reaction $\gamma p \to Xn$ at a mean γp cms energy $\langle W \rangle = 207$ GeV. This result is obtained using Eq. (11) with $\sigma_{\mathrm{tot}}^{\gamma p} = 174 \pm 1 \pm 13$ μb at $\langle W \rangle = 209$ GeV [58]. Integrating r over the range $0.2 < x_L < 1.0$ gives

$$r = 5.72 \pm 0.12(stat.) \pm 0.41(syst.)\ \%,$$

corresponding to an observed cross section in the above kinematic range of

$$\sigma^{\gamma p \to Xn} = 10.0 \pm 0.2(stat.) \pm 1.0(syst.)\ \mu\mathrm{b}.$$

The curves in Fig. 8(a) are based on the effective flux of Eq. (8). For photoproduction, the x_L dependence of the leading-neutron cross section in this model can be expressed as the integral over t (or p_T^2) of Eq. (6):

$$\frac{1}{\sigma}\frac{d\sigma^{\mathrm{LN}}}{dx_L} \propto (1 - x_L)^{\alpha_{I\!P}(0)-1} \int f_{\mathrm{eff}}(x_L, t)dt,$$

where it has been assumed that the $\gamma\pi$ total cross section has the same slow energy dependence as observed for other hadronic cross sections, characterised by the Pomeron intercept, $\alpha_{I\!P}(0)) \sim 1.08$ [59].

The solid histogram in Fig. 8(a) shows the result of a fit using the shape given by Eq. (8) plus a background term proportional to $(1 - x_L)$. The fit[5] uses only statistical uncertainties and gives a good description of the data. Background terms of higher order in $(1 - x_L)$ are not necessary.

The H1 collaboration also finds agreement between their leading-neutron data [2] in the DIS regime and an OPE model. Simple leading-order OPE models (POMPYT and RAPGAP) also

---

[5] The highest-x_L bin was excluded from the fit because of the large systematic uncertainty arising from the energy scale.

give a good description of the ZEUS data on dijets with a leading neutron in photoproduction [3]. A recent NLO calculation [60] based on OPE is also in good agreement with the neutron-tagged dijet data.

8.3 Vertex factorisation

Leading baryon production in hadronic reactions has often been analysed in the context the Triple Regge expansion [16, 61]. If the pion trajectory dominates leading neutron production, as the data reported in this paper suggest, and if the $s\prime$ values are sufficiently high, then the π-π-Pomeron triple-Regge vertex will dominate. This is a reasonable approximation since s' is typically 80 GeV and factorisation should hold. The cross-section ratios are therefore given by

$$\frac{d^2\sigma^{ap\to Xn}(x_L, p_T^2)}{dx_L\, dp_T^2} \Bigg/ \frac{d^2\sigma^{bp\to Xn}(x_L, p_T^2)}{dx_L\, dp_T^2} = \frac{\sigma^{ap}_{\mathrm{tot}}}{\sigma^{bp}_{\mathrm{tot}}},$$

or, with $a = \gamma$ and $b = p$,

$$\frac{1}{\sigma^{\gamma p}_{\mathrm{tot}}} \frac{d^2\sigma^{\gamma p\to Xn}(x_L, p_T^2)}{dx_L\, dp_T^2} = \frac{1}{\sigma^{pp}_{\mathrm{tot}}} \frac{d^2\sigma^{pp\to Xn}(x_L, p_T^2)}{dx_L\, dp_T^2}. \tag{13}$$

To test this relation, the PHP data were integrated over p_T^2, assuming that the functional form of Eq. (12) also applies to photoproduction. The results for the PHP sample, expressed as the normalised cross section at $p_T^2 = 0$, are shown in Fig. 8(b). These data are compared with ISR data [28] from the reaction $pp \to Xn$. The shapes of the two distributions are similar but the PHP data are about a factor of two below the ISR pp results for $x_L > 0.3$. These distributions, when integrated over all p_T^2 and x_L, represent the average number of neutrons per event, $< n >$. Using Eq. (12) to integrate over all p_T^2, the ZEUS PHP data yield $< n > \approx 0.18$ for the region $x_L > 0.28$. The value 0.375 ± 0.075 for $\theta_n < 150$ mrad per hemisphere per inelastic pp collision was obtained at the ISR [27] and is a factor of two larger than the value obtained in the current analysis.

The curve in Fig. 8(b), based on the OPE model with the effective flux of Eq. (8), gives a good representation of the shape of the ZEUS PHP data for $x_L > 0.6$. In summary, while the shapes of the γp and pp distributions are similar, the cross-section scaling expressed in Eq. (13) is broken by about a factor of two. This breaking suggests that other Regge trajectories, with their associated interferences, are contributing differently to the photo- and hadroproduction reactions.

8.4 Absorptive effects

In $\gamma^* p$ scattering, the transverse size of the virtual photon decreases with increasing Q^2, reducing the likelihood that the produced neutron rescatters on the hadronic component of the photon.

At very high Q^2, the virtual photon acts as a point-like probe. The HERA data thus offer the opportunity to study scattering with a target of fixed size (the proton) and a projectile of variable size (the photon). Figure 7(a) shows a clear reduction in the relative yield of neutrons in PHP and in the intermediate-Q^2 region compared to that in DIS at higher Q^2. This reduction, which is displayed as a function of Q^2 in Fig. 9 for $0.64 < x_L < 0.82$, may be attributed to absorptive effects. Recently, a similar rise in the leading-proton yield as Q^2 is increased from the PHP region to $Q^2 > 2.5$ GeV^2 has been observed by the H1 collaboration [6].

The x_L dependence of this effect is shown in Fig. 10, where the ratio $R_{\rm abs}(x_L)$ is defined as

$$R_{\rm abs}(x_L) \equiv \frac{r(Q^2 < 0.02\ {\rm GeV}^2, x_L)}{r(Q^2 > 4\ {\rm GeV}^2, x_L)}.$$

In order to minimise sensitivity to drifts in the relative energy scales, which particularly affects the higher values of x_L, only PHP and DIS data taken simultaneously were used to evaluate the seven $R_{\rm abs}$ points highest in x_L. Figure 10 shows that $R_{\rm abs}$ is approximately constant, although some variation is observed for the higher x_L values.

The curves in Fig. 10 are theoretical predictions based on OPE models [35,36] for the difference in absorption between $Q^2 > 10$ GeV^2 and photoproduction. The t dependence of the absorptive correction has been evaluated over a kinematic region similar to that of the present analysis to give the t-averaged correction. The calculations [35, 36] predict that absorption at the level of $\sim$10% may still be present for $Q^2 > 10$ GeV^2.

In conclusion, the characteristics of the production of leading neutrons in the range $0.64 < x_L < 0.82$, i.e. the rapid rise in rate with Q^2 and the saturation for the DIS data, are in broad agreement with the expectation from absorptive effects.

8.5 Tests of limiting fragmentation and factorisation in x and Q^2

The hypothesis of limiting fragmentation [10] states that, in the high-energy limit, the cross section for the inclusive production of particle c in the fragmentation region of b in the reaction $a + b \to c + X$ will approach a constant value. This suggestion, which was based on rather general geometrical arguments, was supported by measurements made at the ISR [34]. The expectation at HERA is that neutron production in the proton-fragmentation region of ep collisions will be independent of Q^2 and W [11].

A more differential form of factorisation than that discussed in Section 8.3 states that the dependence of the cross section on the lepton variables (x and Q^2) should be independent of the baryon variables (x_L and p_T^2). In terms of the structure function $F_2^{\rm LN(4)}$, this can be written as

$$F_2^{\rm LN(4)}(x, Q^2, x_L, p_T) = f(x_L, p_T) \cdot F(x, Q^2),$$

where f and F are arbitrary functions. The quantity $F_2^{\rm LN(3)}$ is then given by

$$F_2^{\rm LN(3)}(x, Q^2, x_L) = \tilde{f}(x_L) \cdot F(x, Q^2), \qquad (14)$$

where

$$\tilde{f}(x_L) = \int_0^{p_T^{\rm max}(x_L)} f(x_L, p_T) dp_T.$$

To investigate the W dependence, the data may be studied as a function of y, or x, for fixed Q^2. Figure 11 compares the cross-section ratio, r, as a function of Q^2 at fixed y by choosing three bins of y for a low $(0.20 < x_L < 0.64)$, a medium $(0.64 < x_L < 0.82)$ and a high $(0.82 < x_L < 1.0)$ x_L range. At low x_L and fixed y, r rises with Q^2, approximately doubling over the kinematic range of five orders of magnitude in Q^2. As x_L increases, the slope of r as a function of Q^2 decreases and becomes negative in the high-x_L range.

Figure 12 shows the values of r for the intermediate-Q^2 data, separately for the low, medium and high ranges of x_L. There is little variation of the ratio, r, as a function of y. The dotted horizontal lines in the figures, which show the average values of the points in each x_L bin, are a satisfactory representation of the data.

Figure 13 shows r for the DIS data as a function of x in bins of Q^2 and x_L. The same trends as in Fig. 11 are observed. At fixed Q^2, there is a small, but systematic, dependence of r on x. At low x_L, the ratio rises with x; for $0.64 < x_L < 0.82$, the ratio is approximately independent of x; at high x_L, it falls with increasing x. The dotted lines show the results of fits of the form $(x_1/x)^\lambda$, where x_1 and λ are fit parameters. Each x_L range is fitted separately.

These fits provide a good representation of the data except at the highest x_L at high Q^2. The data can also be fit to the form $a + b\ln(x/x_0) + c\ln(Q^2/Q_0^2)$, where a, b and c are fit parameters and Q_0^2 and x_0 are arbitrary scales. This gives a good representation of the data in all x_L bins, as shown by the solid lines.

In summary, the observed weak, logarithmic, variation as the size of the virtual photon changes represents a breakdown of limiting fragmentation and the factorisation as expressed in Eq. (14). However, in the interval $0.64 < x_L < 0.82$, r for the DIS data is, to a good approximation, independent of the leptonic variables and is only a function of x_L. For this x_L range, Eq. (10) implies that

$$F_2^{\mathrm{LN(3)}}(x, Q^2, x_L) \propto F_2(x, Q^2)\,. \tag{15}$$

9 Determination of $F_2^{\mathrm{LN(3)}}$

The neutron-tagged structure function, $F_2^{\mathrm{LN(3)}}$, was determined using Eq. (10). The $F_2(x, Q^2)$ values were taken from the ZEUS Regge fit [62] in the intermediate-Q^2 region, $Q^2 < 1$ GeV^2, and from the ZEUS NLO QCD fit [63] for $Q^2 > 1$ GeV^2. Figures 14 (intermediate-Q^2 data) and 15 (DIS data) show $F_2^{\mathrm{LN(3)}}$ for three representative ranges of x_L as a function of x at fixed values of Q^2. The normalisation of the three sets of fixed-x_L data varies because the range of p_T^2 changes with x_L when integrating over a fixed θ_n range. To guide the eye, the line shows the ZEUS Regge or NLO fit appropriately scaled by r in each x_L bin divided by Δx_L. The x and Q^2 dependence of $F_2^{\mathrm{LN(3)}}$ is similar to that of F_2, as expected since, as shown in Figs. 11 and 13, the ratio r has only a weak dependence on x and Q^2 at fixed x_L.

The H1 Collaboration has published values of $F_2^{\mathrm{LN(3)}}$ in the kinematic region $2 \leq Q^2 \leq 50$ GeV^2 and $6 \cdot 10^{-5} \leq x \leq 6 \cdot 10^{-3}$ [2]. This region overlaps that covered by the ZEUS data for $Q^2 > 4$ GeV^2. Although the H1 data cover the ZEUS range in x_L, the distribution of the neutrons is integrated only up to $p_T^{\mathrm{max}} = 0.2$ GeV, so the ZEUS and H1 data can only be directly compared at $x_L = 0.3$, corresponding to $p_T^{\mathrm{max}} = 0.197$ GeV. For higher x_L, the ZEUS values must be reduced to account for the smaller p_T range measured by H1. Figure 16(a) compares the ZEUS and H1 values for $F_2^{\mathrm{LN}(3)}$ at $x_L = 0.3$ for the three bins of Q^2 where the data overlap. Figure 16(b) shows the same comparison at $x_L = 0.7$, where the ZEUS data have been adjusted to the transverse-momentum range $p_T^{\mathrm{max}} = 0.2$ GeV using the form of Eq. (12). The shapes of the distributions are in good agreement, as is the normalisation for the higher-x_L selection. At low x_L, although the H1 values lie systematically above the corresponding ZEUS measurements, the H1 uncertainties are highly correlated. In addition, contributions from photon showers, which populate the low x_L region, have not been subtracted from the H1 data.

10 OPE and the pion structure function

In a one-pion-exchange model, the structure function $F_2^{\mathrm{LN}(4)}$ can be written as

$$F_2^{\mathrm{LN}(4)}(x, Q^2, x_L, t) = f_{\pi/p}(x_L, t) F_2^{\pi}(x/(1-x_L), Q^2, t)(1 - \Delta_{\mathrm{abs}}(Q^2, x_L, t)), \tag{16}$$

where $f_{\pi/p}$ is the flux of pions in the proton, F_2^{π} is the structure function of the pion at a virtuality t, and Δ_{abs} is the absorptive correction before a t-integration is performed.

There is now no simple factorisation of $F_2^{\mathrm{LN}(4)}$, although if F_2^{π} can be expressed as a power law in x_π, where the Bjorken variable of the pion is defined as $x_\pi = x/(1-x_L)$, as is the case for F_2 of the proton with respect to x [63], the approximate factorisation of Eq. (14) will be restored.

Comparison of Eq. (14) with Eq. (10) (neglecting Δ) shows that if F is identified with F_2, then $r/\Delta x_L$ may be identified with $\tilde{f}$. Given that r for the DIS data with $0.64 < x_L < 0.82$ (where OPE dominates, see Section 10.1) is only a function of x_L, as described in Section 8.5, Eqs. (15) and (16) imply that

$$F_2^{\pi}(x_\pi, Q^2) \propto F_2(x, Q^2)\,.$$

10.1 Competing processes to OPE

Several processes which compete with pion exchange as the mechanism for leading neutron production were ignored in Eq. (16), namely:

- diffractive dissociation in which the dissociated system decays to a state including a neutron

  Diffractively produced events can be selected by requiring the presence of a large rapidity gap in the hadronic final state. For such events, the mass of the dissociated proton system is restricted to low values, $M_{\mathrm{N}} \lesssim 4$ GeV.

  An event is said to have a large rapidity gap (LRG) in the ZEUS detector if the pseudorapidity of the most-forward energy deposit with energy greater than 400 MeV (η_{max}) is less than 1.8 [64]. Figure 17(a) shows the η_{max} distributions for both the neutron-tagged and inclusive DIS samples, where the latter has been normalised to the neutron-tagged sample for $\eta_{\mathrm{max}} > 1.8$. For both $\eta_{\mathrm{max}} < 1.8$ and $\eta_{\mathrm{max}} > 1.8$, the shape of the neutron-tagged distribution is similar to that of the inclusive distribution; however, there are relatively fewer LRG events in the neutron-tagged sample. The LRG events represent only 4% of the total number of DIS events with neutrons in the measured kinematic region, but are 7% of the total number of DIS events. A reduction in the fraction of LRG events with a final-state neutron is expected since only proton diffractive dissociation or diffractive meson exchange (the Deck effect [65]) can contribute.

  To investigate a possible x_L-dependence of the contribution of diffractive events, Fig. 17(b) shows the ratio, R_{LRG}, of the neutron-tagged DIS events, selected by the LRG criterion, to all neutron-tagged DIS events, as a function of x_L. The rise by a factor of three over the x_L range shows that the LRG neutron-tagged events have a harder neutron energy spectrum than that of the inclusive neutron-tagged sample. It is clear that diffractive events are not a major source of leading neutrons at any value of x_L. For the region $0.64 < x_L < 0.82$, R_{LRG} is 0.039 ± 0.001 (*stat.*);

- ρ and a_2 exchange

  Theoretical studies of neutron production in *ep* collisions [18, 53] suggest that isovector exchanges other than the pion contribute less than 10% to neutron production at $x_L = 0.73$ and for the p_T range of the present data. This is quite different than for leading proton production, where isoscalar Regge exchange provides the dominant contribution [2, 19];

- isovector exchange leading to Δ production

  The $p \to \Delta(1236)$ transition, formed by π, ρ and a_2 exchange, can also contribute to neutron production [18, 53, 66–68]. In this case, the neutron, which comes from the decay $\Delta^0 \to n\pi^0$ or $\Delta^+ \to n\pi^+$, no longer has an energy determined by the energy of the exchanged meson. The neutron energy spectrum peaks near $x_L \approx 0.5$ and extends only to $x_L \approx 0.7$ [19]. It thus gives a small contribution in the $0.64 < x_L < 0.82$ bin. A comparison of the data on $p \to n$ and $p \to \Delta^{++}$ [69–72] in charge-exchange reactions at Fermilab indicates that only about 6% of the forward neutrons come from the Δ channel. This observation agrees with theoretical estimates of the $\Delta\pi$ contribution to the Fock state of the proton, which is approximately half that of $n\pi$ [53, 66]. A calculation [67] shows that the contribution of ρ/a_2 exchange, plus the Δ contribution, to the hadronic charge-exchange reaction $pp \to Xn$ could be as high as 30%. Since no analogous calculation exists for DIS, this only provides an indication of a possible background to the neutron production discussed in this paper;

- models other than one-particle exchange

  Monte Carlo studies, using standard DIS generators, show [1] that these processes have a rate of neutron production a factor of three lower than the data and produce a neutron energy spectrum with the wrong shape, peaking at values of x_L below 0.3.

In summary, the expectation for the processes listed above at $\langle x_L \rangle = 0.73$ and $\langle {p_T}^2 \rangle = 0.08$ GeV^2 is that they contribute of the order of 20% of the leading neutron production. This estimate can be checked using the measured neutron-energy spectrum. The OPE fit to the differential cross-section $d\sigma/dx_L$ shown in Fig. 8(a) suggests that, at $x_L = 0.73$, the residual background to OPE is $\lesssim$ 10%, in reasonable accord with the studies discussed above.

10.2 The pion structure function and the photon-pion total cross section

Having established that the leading neutron data are dominated by pion exchange in the range $0.64 < x_L < 0.82$, the OPE model can be used to determine the structure function of the pion, F_2^π. The quantity $F_2^{\rm LN(3)}$, defined in Section 2, was obtained by integrating $F_2^{\rm LN(4)}$ over t (or θ_n). The t dependence of F_2^π is absorbed into the flux factor that describes the hadronic charge-exchange data [24–33]; the structure function of the real pion is then given by $F_2^\pi(x_\pi, Q^2) \equiv F_2^\pi(x_\pi, Q^2, t = m_\pi^2)$.

Integrating Eq. (16) over t and rearranging leads to

$$F_2^\pi(x_\pi, Q^2) = \Gamma(Q^2, x_L) F_2^{\rm LN(3)}(x, Q^2, x_L), \tag{17}$$

where $\Gamma(Q^2, x_L)$ is the inverse of the pion flux factor integrated over the measured t region and corrected for the t-averaged absorptive effect, $\delta_{\rm abs}$:

$$\Gamma(Q^2, x_L) = \frac{1}{(1 - \delta_{\rm abs}(x_L, Q^2)) \int_{t_{\rm min}}^{t_{\rm max}} f_{\pi/p}(x_L, t) dt}.$$

As discussed in Section 8.4, the theoretical expectation [36] is that $\delta_{\rm abs}(x_L, Q^2)$ is less than 10% for $Q^2 > 10$ GeV^2.

Thus, Eq. (17) shows that, for the DIS region, $F_2^\pi(x_\pi, Q^2)$ is approximately proportional to $F_2^{\rm LN(3)}(x, Q^2, x_L)$ for a fixed x_L. In analogy to Eq. (17), the photon-pion total cross section can be written as

$$\sigma_{\rm tot}^{\gamma\pi}(W\sqrt{1 - x_L}) = \Gamma(Q^2 = 0, x_L) \cdot \frac{d\sigma^{\gamma p \to Xn}(W, Q^2 = 0)}{dx_L}. \tag{18}$$

10.3 The pion-flux normalisation

To determine the normalisation of the pion flux, and hence F_2^π and $\sigma_{tot}^{\gamma\pi}$, a theoretical model is necessary for the form factor $F(x_L, t)$ in the effective flux factor of Eq. (7). Unfortunately, there is no consensus as to which of the competing models [73] is most appropriate. As examples of the extremes from the available range of the models, two possibilities are considered here. The evaluation of the normalisation is made at $x_L = 0.73$, where the ratio r is approximately independent of x and Q^2 and OPE is expected to dominate.

1. One possibility is to use the same flux as is employed in hadronic reactions. The data on the hadron charge-exchange reactions $pn \to Xp$, $pp \to Xn$ and $\pi n \to Xp$ [24–33] are in good agreement with OPE and the Bishari flux factor [15] given by Eq. (8). Using Eq. (6), the cross section may be written as

   $$\sigma^{pn \to Xp} = \int\int f_{\rm eff}(x_L, t) \sigma_{\rm tot}^{\pi p} dt\, dx_L,$$

   where $\sigma_{\rm tot}^{\pi p}$ is the πp total cross section and the integration is over the kinematic range of the $pn \to Xp$ measurement. The flux factor, $f_{\rm eff}$, can again be interpreted as an *effective* pion flux which already incorporates the effects of absorption, processes other than OPE and off-mass-shell effects.

Assuming that all of these effects are the same for the photoproduction reaction $\gamma p \to Xn$ as for the hadronic processes $pn \to Xp$ and $pp \to Xn$ then

$$\Gamma(Q^2=0, \langle x_L \rangle = 0.73) = \frac{\Delta x_L}{\int \int_{t_{\min}}^{t_{\max}} f_{\mathrm{eff}}(\langle x_L \rangle = 0.73, t) dt\, dx_L} = \frac{0.18}{0.0775} = 2.32,$$

for the range $0.64 < x_L < 0.82$.

Using Eq. (18) with $d\sigma^{\gamma p \to Xn}/dx_L$ evaluated from Fig. 8(a) at $x_L = 0.73$, $\sigma^{\gamma\pi}_{\mathrm{tot}}(W = 107 \text{ GeV})$ is 50 ± 2 μb. Assuming a Regge dependence such that $\sigma \propto (W^2)^{\alpha_{I\!P}(0)-1}$ with $\alpha_{I\!P}(0) = 1.08$ [59] yields $\sigma^{\gamma\pi}_{\mathrm{tot}}(W = 207 \text{ GeV}) = 56 \pm 2$ μb. Given that $\sigma^{\gamma p}_{\mathrm{tot}}(W = 209 \text{ GeV}) = 174 \pm 13$ μb [58], $\sigma^{\gamma\pi}_{\mathrm{tot}}/\sigma^{\gamma p}_{\mathrm{tot}}$ is then 0.32 ± 0.03.

Using Fig. 9 to estimate the difference in the absorption for DIS and photoproduction as 22% leads, for $Q^2 > 4$ GeV^2, to

$$F_2^{\pi}(x_\pi, Q^2) = 1.81\, F_2^{\mathrm{LN}(3)}(x, Q^2, \langle x_L \rangle = 0.73),$$

or, combining Eqs. (10) and (17),

$$F_2^{\pi}(x_\pi, Q^2) = 10.05 \cdot r(x, Q^2, \langle x_L \rangle = 0.73) \cdot F_2(x, Q^2). \tag{19}$$

2. As a second possibility, the additive quark model [74] can be used, which predicts that, at $x_L = 0.73$,

$$\frac{\sigma^{\gamma\pi}_{\mathrm{tot}}(W\sqrt{1-x_L})}{\sigma^{\gamma p}_{\mathrm{tot}}(W)} = \frac{2}{3}(1-x_L)^{\alpha_{I\!P}(0)-1} = 0.60, \tag{20}$$

provided that $\sigma^{\gamma\pi}_{\mathrm{tot}}$ and $\sigma^{\gamma p}_{\mathrm{tot}}$ have the same energy dependence at high energies, governed by the Pomeron intercept, $\alpha_{I\!P}(0) = 1.08$. Combining Eq. (11) with Eqs. (18) and (20) and using Table 3 gives

$$\Gamma(Q^2=0, \langle x_L \rangle = 0.73) = \frac{2}{3}(1-0.73)^{\alpha_{I\!P}(0)-1} \frac{\Delta x_L}{r(Q^2=0, \langle x_L \rangle = 0.73)} = \frac{0.60}{0.1251} = 4.8.$$

Using R_{abs} to adjust for the difference in absorptive effects between photoproduction and DIS, thereby reducing Γ, yields, for $Q^2 > 4$ GeV^2:

$$\begin{aligned} F_2^{\pi}(x_\pi, Q^2) &= 3.74 F_2^{\mathrm{LN}(3)}(x, Q^2, \langle x_L \rangle = 0.73) \\ &= 20.78 \cdot r(x, Q^2, \langle x_L \rangle = 0.73) \cdot F_2(x, Q^2). \end{aligned} \tag{21}$$

In summary, methods 1 and 2 differ in normalisation by about a factor of two. This is approximately the same factor that was observed in Fig. 8(b) when comparing the neutron rates presented here and the *pp* data from the ISR.

Other methods give factors between those described above. For example, models of the pion flux factor based on $\bar{d}/\bar{u}$ data give form factors, $F(x_L, t) < 1$ [73,75] and, therefore, a value of Γ that is higher than that given by method 1. Normalisation of F_2^{π} using existing measurements at high x_π [38–44], as parameterised, for example, by Glück, Reya and Vogt [76], gives a Γ value that is lower than that from method 2.

10.4 Results and comparison with models

Figure 18 shows $F_2^{\pi,EF}(x_\pi, Q^2)$, which is $F_2^\pi(x_\pi, Q^2)$ as a function of x_π evaluated from Eq. (19). This evaluation has been made for the range $0.64 < x_L < 0.82$ where OPE is expected to dominate and where the fraction of events with a leading neutron is observed to be approximately independent of x and Q^2. Evaluations for nearby ranges of x_L give consistent results. Although the normalisation of F_2^π is uncertain to a factor of two, the x and Q^2 dependence is well measured. The dotted lines show the shape of F_2 of the proton, scaled by 0.361. It is striking that F_2^π has approximately the same x and Q^2 dependence as F_2 of the proton.

Figure 19 shows $F_2^{\pi,AQM}$ using the additive quark model to normalise the cross section. The comparison of these results with the solid curves, which represent the absolute predictions of Glück, Reya and Vogt (GRV) [76], shows that the normalisation is such that the curves are closer to the data than when using the effective flux shown in Fig. 18, although the data are still higher than the predictions, particularly at the lower values of Q^2.

There have been several recent attempts to understand the quark structure of the pion on the basis of simple theoretical ideas:

1. In the model of Glück, Reya and Vogt [76], the pion sea is generated dynamically by the QCD evolution equations from the valence-quark and valence-gluon distributions of the pion at a low scale $\mu^2 \approx 0.3$ GeV^2. The valence gluon is, by assumption, proportional to the valence quark. The valence quarks are taken from fits to experimental data [38–44] at high x_π. This model qualitatively describes the shape of the measurement of F_2^π as seen in Figs 18 and 19;

2. The prediction for F_2^π from Sutton et al. (SMRS) [77] is also shown in Figure 19. This analysis is an NLO QCD fit to Drell-Yan and prompt-photon data from fixed-target experiments.

   Since the data corresponds to $x_\pi > 0.2$, the predictions for the sea region are uncertain. However, the SMRS fits, when used in an OPE Monte Carlo simulation, gave a good description of the ZEUS data on leading neutrons plus dijets in photoproduction [3]. The latter correspond to the region $x_\pi > 10^{-2}$, whereas the present data extend to much lower x_π and show a very different shape than the F_2^π from the SMRS parameterisation;

3. In the constituent model of Altarelli et al [78], the structure function of any hadron is determined by that of its constituent quarks, and, in particular, the pion structure function can be predicted from the known nucleon structure function [79]. The structure function of a hadron h, F_2^h, at low x, where the contribution of the constituent valence quarks is negligible, is given by

   $$F_2^h(x, Q^2) = \int_x^1 f_h(z) F_2^q(x/z, Q^2) dz,$$

   where $f_h(z)$ is the density of quarks carrying momentum fraction z of the hadron h, and F_2^q is the structure function of the valence quarks. It is assumed that, at low x, the structure function F_2^q is independent of the flavour. If, as $x \to 0$, $F_2^q(x) \sim x^{-\lambda(Q^2)}$, where $\lambda(Q^2)$ is independent of x [63], all of the F_2^h structure functions are proportional to the same function at low x. This prediction is in agreement with the present data since $F_2^\pi \propto F_2$. This model gives a normalisation for F_2^π close to $F_2^{\pi,AQM}$;

4. Nikolaev, Speth and Zoller have explicitly studied the small-x behavior of F_2^π using a colour-dipole BFKL-Regge expansion [80]. They find that a good approximation is:

$$F_2^\pi(x,Q^2) \simeq \frac{2}{3} F_2^p \left(\frac{2}{3}x, Q^2\right).$$

   Since F_2 has a power-law behaviour in x for the ZEUS kinematic region, the predicted shape is in reasonable agreement with the data.

Thus, the data presented in this paper provide additional constraints on the shape of the pion structure function for values of $x_\pi < 10^{-2}$.

11 Conclusions

Leading neutron production for $x_L > 0.2$ and $\theta_n < 0.8$ mrad has been studied in neutral current ep collisions at HERA over a kinematic range of over five orders of magnitude in Q^2. The cross section for the production of leading neutrons has been determined as a ratio r relative to the inclusive neutral current cross section, thereby reducing the systematic uncertainty considerably.

For the above angular range, which defines a transverse-momentum acceptance of $p_T < 0.656\, x_L$ GeV, the neutron energy spectrum exhibits a broad peak at $x_L \approx 0.75$. It is approximately one third of its maximum at $x_L = 0.2$, and falls to zero approaching the kinematic limit at $x_L = 1$. The rate of neutron production in the measured phase space in photoproduction is about half the rate observed in hadroproduction and thus the simplest form of vertex factorisation is broken. A comparison of the neutron yield in the three kinematic regions of photoproduction, intermediate Q^2 and DIS shows an increase of about 20% between photoproduction and DIS, saturating for $Q^2 > 4$ GeV^2. This can be attributed to the decrease in absorptive effects as the transverse size of the incident photon decreases.

Generally, there is no strong dependence of the ratio r on x and Q^2; however, at low x_L and fixed y, the ratio r rises with Q^2, approximately doubling over the kinematic range of five orders of magnitude in Q^2. For the high-x_L range, there is a tendency for r to decrease at fixed y. Thus, limiting fragmentation and factorisation do not hold.

The structure-function $F_2^{\mathrm{LN}(3)}$ has been measured over three orders of magnitude in x and Q^2 and for the range $0.2 < x_L < 0.8$ with $\theta_n < 0.8$ mrad. The structure function of the pion, F_2^π, has been extracted, up to uncertainties in the overall normalisation, in the framework of a one-pion-exchange model in the range $0.64 < x_L < 0.82$, where one-pion-exchange dominates. It has approximately the same x and Q^2 dependence as F_2 of the proton. The data provide new constraints on the shape of the pion structure function for $x_\pi < 10^{-2}$.

Acknowledgements

We are especially grateful to the DESY Directorate whose encouragement and financial support made possible the construction and installation of the FNC. We are also happy to acknowledge the efforts and forbearance of the DESY accelerator group, whose machine components are crowded by the FNC, and the support of the DESY computing staff.

We thank G. Altarelli, L. Frankfurt, N. Nikolaev, M. Strikman and A. Szczurek for their help with many of the theoretical issues involved in this study.

This study was only made possible by the physics insight and hard work of G. Levman, to whom we owe a great debt of gratitude.

Appendix I: Tables of relative cross sections

This appendix presents tables of the relative cross sections for leading neutron production in neutral current interactions, $ep \to e'Xn$. The cross sections are measured relative to the total inclusive neutral current cross section, $ep \to e'X$.

The x_L bins, the acceptance and the acceptance and energy-scale uncertainties for each bin are given in Table 1. Only for $0.88 < x_L < 1$ is the centroid of the bin, 0.92, significantly different from the bin centre, 0.94.

The values of b, the exponential slope of the p_T^2 distribution, are given in Table 2.

Table 3 gives the relative differential cross section in x_L, $(1/\sigma)(d\sigma^{\mathrm{LN}}/dx_L)$, for leading neutron production integrated over x and Q^2 for the three kinematic regimes: a) photoproduction ($Q^2 < 0.02$ GeV^2), (b) the intermediate-Q^2 region ($0.1 < Q^2 < 0.74$ GeV^2), and (c) DIS ($Q^2 > 4$ GeV^2).

A change in the energy scale represents a stretch or compression (dilation) of the energy distribution. Although the dilation is only ±2%, it becomes the dominant normalisation systematic uncertainty at high x_L, where the energy spectrum is falling quickly (Table 3).

The next twelve tables give the fraction of events with a leading neutron in DIS ($Q^2 > 4$ GeV^2) in bins of Q^2 and x, while the final three tables give the fraction of events with a leading neutron in the intermediate-Q^2 region ($0.1 < Q^2 < 0.74$ GeV^2) in bins of Q^2 and y.

x_L range	$< x_L >$	Acceptance (%)	Acceptance uncertainty (%)	Energy-scale uncertainty contribution (%)
0.20 - 0.28	0.24	21.5	+2/-2	-5/+4
0.28 - 0.34	0.31	21.2	+2/-2	-5/+4
0.34 - 0.40	0.37	21.7	+2/-3	-5/+4
0.40 - 0.46	0.43	22.2	+3/-3	-5/+4
0.46 - 0.52	0.49	22.5	+3/-3	-4/+5
0.52 - 0.58	0.55	21.9	+4/-3	-4/+5
0.58 - 0.64	0.61	23.0	+4/-4	-4/+4
0.64 - 0.70	0.67	22.9	+5/-5	-4/+4
0.70 - 0.76	0.73	23.3	+5/-5	-2/+2
0.76 - 0.82	0.79	23.7	+5/-6	+2/-1
0.82 - 0.88	0.85	25.4	+6/-6	+5/-8
0.88 - 1.00	0.92	32.1	+6/-6	+25/-26

Table 1: The x_L bins, their acceptance, and the acceptance uncertainty. The right hand column shows the contribution from the energy-scale uncertainty. Note that the energy-scale uncertainty is completely correlated between bins.

$\langle x_L \rangle$	b GeV^{-2}	$\pm(stat.)$ GeV^{-2}
0.49	4.10	1.10
0.54	4.47	1.00
0.58	3.80	1.10
0.62	6.33	1.00
0.65	8.12	0.90
0.69	8.56	0.90
0.73	6.06	0.80
0.76	9.46	0.90
0.80	8.78	0.80
0.84	12.81	1.10
0.88	9.65	0.90
0.95	8.63	1.10

Table 2: The values of the b slopes and their statistical errors in bins of x_L for the 1995 DIS data.

x_L range	$< x_L >$	$Q^2 < 0.02$ GeV^2 *meas.* ± *stat.*	$0.1 < Q^2 < 0.74$ GeV^2 *meas.* ± *stat.* (%)	$Q^2 > 4$ GeV^2 *meas.* ± *stat.* (%)
0.20 - 0.28	0.24	4.12 ± 0.60	4.70 ± 0.36	5.57 ± 0.13
0.28 - 0.34	0.31	4.40 ± 0.71	6.37 ± 0.46	7.19 ± 0.17
0.34 - 0.40	0.37	4.64 ± 0.72	5.83 ± 0.42	8.51 ± 0.18
0.40 - 0.46	0.43	6.31 ± 0.84	7.66 ± 0.50	9.44 ± 0.19
0.46 - 0.52	0.49	6.90 ± 0.87	7.72 ± 0.49	10.38 ± 0.20
0.52 - 0.58	0.55	7.94 ± 0.34	10.64 ± 0.57	12.38 ± 0.22
0.58 - 0.64	0.61	9.40 ± 0.34	11.03 ± 0.59	13.43 ± 0.22
0.64 - 0.70	0.67	11.15 ± 0.38	12.69 ± 0.62	15.28 ± 0.24
0.70 - 0.76	0.73	12.51 ± 0.41	14.06 ± 0.64	15.83 ± 0.24
0.76 - 0.82	0.79	12.15 ± 0.39	14.41 ± 0.67	14.85 ± 0.23
0.82 - 0.88	0.85	9.18 ± 0.31	11.11 ± 0.56	11.66 ± 0.20
0.88 - 1.00	0.92	2.59 ± 0.09	3.25 ± 0.19	3.74 ± 0.07

Table 3: Values in percent of $(1/\sigma)(d\sigma^{LN}/dx_L) = dr/dx_L$ for leading neutrons with $\theta_n < 0.8$ mrad. For the PHP data, $Q^2 < 0.02$ GeV^2, the normalisation uncertainty is ±5%, and for $x_L > 0.52$ there is a further normalisation uncertainty of ±4%. The statistical error for the PHP data with $x_L > 0.52$ includes a contribution from the uncertainty in the FNC-trigger efficiency. For the intermediate-Q^2 and DIS data, the normalisation uncertainty is ±4%.

$$0.2 < x_L < 0.28$$

Q^2 GeV^2	Q^2 range	$x_{\rm BJ}$	$x_{\rm BJ}$ range	*ratio* (%) *meas.* ± *stat*
7	4 - 10	1.1 $\cdot 10^{-4}$	8.0 - 15.0 $\cdot 10^{-5}$	0.48 ± 0.04
		2.1 $\cdot 10^{-4}$	1.5 - 3.0 $\cdot 10^{-4}$	0.40 ± 0.03
		4.2 $\cdot 10^{-4}$	3.0 - 6.0 $\cdot 10^{-4}$	0.43 ± 0.03
		8.5 $\cdot 10^{-4}$	6.0 - 12.0 $\cdot 10^{-4}$	0.46 ± 0.04
		17.0 $\cdot 10^{-4}$	1.2 - 2.4 $\cdot 10^{-3}$	0.50 ± 0.05
15	10 - 20	2.1 $\cdot 10^{-4}$	1.5 - 3.0 $\cdot 10^{-4}$	0.40 ± 0.05
		4.2 $\cdot 10^{-4}$	3.0 - 6.0 $\cdot 10^{-4}$	0.39 ± 0.03
		8.5 $\cdot 10^{-4}$	6.0 - 12.0 $\cdot 10^{-4}$	0.42 ± 0.03
		17.0 $\cdot 10^{-4}$	1.2 - 2.4 $\cdot 10^{-3}$	0.43 ± 0.04
		49.0 $\cdot 10^{-4}$	2.4 - 10.0 $\cdot 10^{-3}$	0.42 ± 0.03
30	20 - 40	4.2 $\cdot 10^{-4}$	3.0 - 6.0 $\cdot 10^{-4}$	0.55 ± 0.06
		8.5 $\cdot 10^{-4}$	6.0 - 12.0 $\cdot 10^{-4}$	0.50 ± 0.04
		17.0 $\cdot 10^{-4}$	1.2 - 2.4 $\cdot 10^{-3}$	0.43 ± 0.03
		49.0 $\cdot 10^{-4}$	2.4 - 10.0 $\cdot 10^{-3}$	0.49 ± 0.03
60	40 - 80	8.5 $\cdot 10^{-4}$	6.0 - 12.0 $\cdot 10^{-4}$	0.49 ± 0.08
		17.0 $\cdot 10^{-4}$	1.2 - 2.4 $\cdot 10^{-3}$	0.46 ± 0.05
		49.0 $\cdot 10^{-4}$	2.4 - 10.0 $\cdot 10^{-3}$	0.39 ± 0.03
		32.0 $\cdot 10^{-3}$	1.0 - 10.0 $\cdot 10^{-2}$	0.42 ± 0.04
120	80 - 160	17.0 $\cdot 10^{-4}$	1.2 - 2.4 $\cdot 10^{-3}$	0.53 ± 0.12
		49.0 $\cdot 10^{-4}$	2.4 - 10.0 $\cdot 10^{-3}$	0.42 ± 0.05
		32.0 $\cdot 10^{-3}$	1.0 - 10.0 $\cdot 10^{-2}$	0.53 ± 0.05
240	160 - 320	49.0 $\cdot 10^{-4}$	2.4 - 10.0 $\cdot 10^{-3}$	0.42 ± 0.09
		32.0 $\cdot 10^{-3}$	1.0 - 10.0 $\cdot 10^{-2}$	0.56 ± 0.07
480	320 - 640	32.0 $\cdot 10^{-3}$	1.0 - 10.0 $\cdot 10^{-2}$	0.44 ± 0.09
1000	640 - 10000	32.0 $\cdot 10^{-3}$	1.0 - 10.0 $\cdot 10^{-2}$	0.37 ± 0.11

Acceptance uncertainty: +2/-2 %

Energy scale uncertainty of ±2 %: -5/+4 %

Normalization error: 4 %

Table 4: The fraction of events with a leading neutron at $x_L = 0.24$ in bins of x and Q^2.

$$0.28 < x_L < 0.34$$

Q^2 GeV^2	Q^2 range	$x_{\rm BJ}$	$x_{\rm BJ}$ range	*ratio* (%) *meas.* ± *stat*
7	4 - 10	$1.1 \cdot 10^{-4}$	$8.0 - 15.0 \cdot 10^{-5}$	0.34 ± 0.04
		$2.1 \cdot 10^{-4}$	$1.5 - 3.0 \cdot 10^{-4}$	0.37 ± 0.03
		$4.2 \cdot 10^{-4}$	$3.0 - 6.0 \cdot 10^{-4}$	0.41 ± 0.03
		$8.5 \cdot 10^{-4}$	$6.0 - 12.0 \cdot 10^{-4}$	0.50 ± 0.04
		$17.0 \cdot 10^{-4}$	$1.2 - 2.4 \cdot 10^{-3}$	0.46 ± 0.04
15	10 - 20	$2.1 \cdot 10^{-4}$	$1.5 - 3.0 \cdot 10^{-4}$	0.40 ± 0.05
		$4.2 \cdot 10^{-4}$	$3.0 - 6.0 \cdot 10^{-4}$	0.40 ± 0.03
		$8.5 \cdot 10^{-4}$	$6.0 - 12.0 \cdot 10^{-4}$	0.45 ± 0.03
		$17.0 \cdot 10^{-4}$	$1.2 - 2.4 \cdot 10^{-3}$	0.38 ± 0.04
		$49.0 \cdot 10^{-4}$	$2.4 - 10.0 \cdot 10^{-3}$	0.45 ± 0.04
30	20 - 40	$4.2 \cdot 10^{-4}$	$3.0 - 6.0 \cdot 10^{-4}$	0.47 ± 0.06
		$8.5 \cdot 10^{-4}$	$6.0 - 12.0 \cdot 10^{-4}$	0.49 ± 0.04
		$17.0 \cdot 10^{-4}$	$1.2 - 2.4 \cdot 10^{-3}$	0.51 ± 0.04
		$49.0 \cdot 10^{-4}$	$2.4 - 10.0 \cdot 10^{-3}$	0.50 ± 0.03
60	40 - 80	$8.5 \cdot 10^{-4}$	$6.0 - 12.0 \cdot 10^{-4}$	0.37 ± 0.07
		$17.0 \cdot 10^{-4}$	$1.2 - 2.4 \cdot 10^{-3}$	0.38 ± 0.04
		$49.0 \cdot 10^{-4}$	$2.4 - 10.0 \cdot 10^{-3}$	0.52 ± 0.04
		$32.0 \cdot 10^{-3}$	$1.0 - 10.0 \cdot 10^{-2}$	0.51 ± 0.05
120	80 - 160	$17.0 \cdot 10^{-4}$	$1.2 - 2.4 \cdot 10^{-3}$	0.24 ± 0.08
		$49.0 \cdot 10^{-4}$	$2.4 - 10.0 \cdot 10^{-3}$	0.43 ± 0.05
		$32.0 \cdot 10^{-3}$	$1.0 - 10.0 \cdot 10^{-2}$	0.56 ± 0.05
240	160 - 320	$49.0 \cdot 10^{-4}$	$2.4 - 10.0 \cdot 10^{-3}$	0.43 ± 0.09
		$32.0 \cdot 10^{-3}$	$1.0 - 10.0 \cdot 10^{-2}$	0.40 ± 0.06
480	320 - 640	$32.0 \cdot 10^{-3}$	$1.0 - 10.0 \cdot 10^{-2}$	0.55 ± 0.11
1000	640 - 10000	$32.0 \cdot 10^{-3}$	$1.0 - 10.0 \cdot 10^{-2}$	0.45 ± 0.12

Acceptance uncertainty: +2/-2 %

Energy scale uncertainty of ±2 %: -5/+4 %

Normalization error: 4 %

Table 5: The fraction of events with a leading neutron at $x_L = 0.31$ in bins of x and Q^2.

$0.34 < x_L < 0.4$

Q^2 GeV^2	Q^2 range	x_{BJ}	x_{BJ} range	*ratio* (%) *meas.* ± *stat*
7	4 - 10	$1.1 \cdot 10^{-4}$	$8.0 - 15.0 \cdot 10^{-5}$	0.45 ± 0.04
		$2.1 \cdot 10^{-4}$	$1.5 - 3.0 \cdot 10^{-4}$	0.46 ± 0.03
		$4.2 \cdot 10^{-4}$	$3.0 - 6.0 \cdot 10^{-4}$	0.52 ± 0.03
		$8.5 \cdot 10^{-4}$	$6.0 - 12.0 \cdot 10^{-4}$	0.50 ± 0.04
		$17.0 \cdot 10^{-4}$	$1.2 - 2.4 \cdot 10^{-3}$	0.55 ± 0.05
15	10 - 20	$2.1 \cdot 10^{-4}$	$1.5 - 3.0 \cdot 10^{-4}$	0.42 ± 0.05
		$4.2 \cdot 10^{-4}$	$3.0 - 6.0 \cdot 10^{-4}$	0.52 ± 0.03
		$8.5 \cdot 10^{-4}$	$6.0 - 12.0 \cdot 10^{-4}$	0.54 ± 0.04
		$17.0 \cdot 10^{-4}$	$1.2 - 2.4 \cdot 10^{-3}$	0.48 ± 0.04
		$49.0 \cdot 10^{-4}$	$2.4 - 10.0 \cdot 10^{-3}$	0.59 ± 0.04
30	20 - 40	$4.2 \cdot 10^{-4}$	$3.0 - 6.0 \cdot 10^{-4}$	0.45 ± 0.06
		$8.5 \cdot 10^{-4}$	$6.0 - 12.0 \cdot 10^{-4}$	0.49 ± 0.04
		$17.0 \cdot 10^{-4}$	$1.2 - 2.4 \cdot 10^{-3}$	0.55 ± 0.04
		$49.0 \cdot 10^{-4}$	$2.4 - 10.0 \cdot 10^{-3}$	0.58 ± 0.03
60	40 - 80	$8.5 \cdot 10^{-4}$	$6.0 - 12.0 \cdot 10^{-4}$	0.56 ± 0.09
		$17.0 \cdot 10^{-4}$	$1.2 - 2.4 \cdot 10^{-3}$	0.53 ± 0.05
		$49.0 \cdot 10^{-4}$	$2.4 - 10.0 \cdot 10^{-3}$	0.51 ± 0.04
		$32.0 \cdot 10^{-3}$	$1.0 - 10.0 \cdot 10^{-2}$	0.58 ± 0.05
120	80 - 160	$17.0 \cdot 10^{-4}$	$1.2 - 2.4 \cdot 10^{-3}$	0.52 ± 0.12
		$49.0 \cdot 10^{-4}$	$2.4 - 10.0 \cdot 10^{-3}$	0.51 ± 0.05
		$32.0 \cdot 10^{-3}$	$1.0 - 10.0 \cdot 10^{-2}$	0.54 ± 0.05
240	160 - 320	$49.0 \cdot 10^{-4}$	$2.4 - 10.0 \cdot 10^{-3}$	0.52 ± 0.10
		$32.0 \cdot 10^{-3}$	$1.0 - 10.0 \cdot 10^{-2}$	0.59 ± 0.07
480	320 - 640	$32.0 \cdot 10^{-3}$	$1.0 - 10.0 \cdot 10^{-2}$	0.63 ± 0.11
1000	640 - 10000	$32.0 \cdot 10^{-3}$	$1.0 - 10.0 \cdot 10^{-2}$	0.54 ± 0.13

Acceptance uncertainty: +2/-3 %

Energy scale uncertainty of ±2 %: -5/+4 %

Normalization error: 4 %

Table 6: The fraction of events with a leading neutron at $x_L = 0.37$ in bins of x and Q^2.

$0.4 < x_L < 0.46$

Q^2 GeV^2	Q^2 range	$x_{\rm BJ}$	$x_{\rm BJ}$ range	*ratio* (%) *meas.* ± *stat*
7	4 - 10	$1.1 \cdot 10^{-4}$	8.0 - $15.0 \cdot 10^{-5}$	0.51 ± 0.04
		$2.1 \cdot 10^{-4}$	1.5 - $3.0 \cdot 10^{-4}$	0.55 ± 0.03
		$4.2 \cdot 10^{-4}$	3.0 - $6.0 \cdot 10^{-4}$	0.55 ± 0.04
		$8.5 \cdot 10^{-4}$	6.0 - $12.0 \cdot 10^{-4}$	0.55 ± 0.04
		$17.0 \cdot 10^{-4}$	1.2 - $2.4 \cdot 10^{-3}$	0.62 ± 0.05
15	10 - 20	$2.1 \cdot 10^{-4}$	1.5 - $3.0 \cdot 10^{-4}$	0.52 ± 0.05
		$4.2 \cdot 10^{-4}$	3.0 - $6.0 \cdot 10^{-4}$	0.55 ± 0.03
		$8.5 \cdot 10^{-4}$	6.0 - $12.0 \cdot 10^{-4}$	0.55 ± 0.04
		$17.0 \cdot 10^{-4}$	1.2 - $2.4 \cdot 10^{-3}$	0.66 ± 0.05
		$49.0 \cdot 10^{-4}$	2.4 - $10.0 \cdot 10^{-3}$	0.60 ± 0.04
30	20 - 40	$4.2 \cdot 10^{-4}$	3.0 - $6.0 \cdot 10^{-4}$	0.41 ± 0.05
		$8.5 \cdot 10^{-4}$	6.0 - $12.0 \cdot 10^{-4}$	0.46 ± 0.03
		$17.0 \cdot 10^{-4}$	1.2 - $2.4 \cdot 10^{-3}$	0.54 ± 0.04
		$49.0 \cdot 10^{-4}$	2.4 - $10.0 \cdot 10^{-3}$	0.65 ± 0.03
60	40 - 80	$8.5 \cdot 10^{-4}$	6.0 - $12.0 \cdot 10^{-4}$	0.48 ± 0.08
		$17.0 \cdot 10^{-4}$	1.2 - $2.4 \cdot 10^{-3}$	0.64 ± 0.06
		$49.0 \cdot 10^{-4}$	2.4 - $10.0 \cdot 10^{-3}$	0.53 ± 0.04
		$32.0 \cdot 10^{-3}$	1.0 - $10.0 \cdot 10^{-2}$	0.67 ± 0.06
120	80 - 160	$17.0 \cdot 10^{-4}$	1.2 - $2.4 \cdot 10^{-3}$	0.65 ± 0.14
		$49.0 \cdot 10^{-4}$	2.4 - $10.0 \cdot 10^{-3}$	0.59 ± 0.06
		$32.0 \cdot 10^{-3}$	1.0 - $10.0 \cdot 10^{-2}$	0.64 ± 0.06
240	160 - 320	$49.0 \cdot 10^{-4}$	2.4 - $10.0 \cdot 10^{-3}$	0.77 ± 0.12
		$32.0 \cdot 10^{-3}$	1.0 - $10.0 \cdot 10^{-2}$	0.70 ± 0.08
480	320 - 640	$32.0 \cdot 10^{-3}$	1.0 - $10.0 \cdot 10^{-2}$	0.77 ± 0.12
1000	640 - 10000	$32.0 \cdot 10^{-3}$	1.0 - $10.0 \cdot 10^{-2}$	0.75 ± 0.16

Acceptance uncertainty: +3/-3 %

Energy scale uncertainty of ±2 %: -5/+4 %

Normalization error: 4 %

Table 7: The fraction of events with a leading neutron at $x_L = 0.43$ in bins of x and Q^2.

$$0.46 < x_L < 0.52$$

Q^2 GeV^2	Q^2 range	$x_{\rm BJ}$	$x_{\rm BJ}$ range	*ratio* (%) *meas.* ± *stat*
7	4 - 10	$1.1 \cdot 10^{-4}$	8.0 - $15.0 \cdot 10^{-5}$	0.51 ± 0.04
		$2.1 \cdot 10^{-4}$	1.5 - $3.0 \cdot 10^{-4}$	0.59 ± 0.03
		$4.2 \cdot 10^{-4}$	3.0 - $6.0 \cdot 10^{-4}$	0.57 ± 0.04
		$8.5 \cdot 10^{-4}$	6.0 - $12.0 \cdot 10^{-4}$	0.67 ± 0.05
		$17.0 \cdot 10^{-4}$	1.2 - $2.4 \cdot 10^{-3}$	0.69 ± 0.05
15	10 - 20	$2.1 \cdot 10^{-4}$	1.5 - $3.0 \cdot 10^{-4}$	0.55 ± 0.05
		$4.2 \cdot 10^{-4}$	3.0 - $6.0 \cdot 10^{-4}$	0.59 ± 0.03
		$8.5 \cdot 10^{-4}$	6.0 - $12.0 \cdot 10^{-4}$	0.65 ± 0.04
		$17.0 \cdot 10^{-4}$	1.2 - $2.4 \cdot 10^{-3}$	0.67 ± 0.05
		$49.0 \cdot 10^{-4}$	2.4 - $10.0 \cdot 10^{-3}$	0.62 ± 0.04
30	20 - 40	$4.2 \cdot 10^{-4}$	3.0 - $6.0 \cdot 10^{-4}$	0.50 ± 0.06
		$8.5 \cdot 10^{-4}$	6.0 - $12.0 \cdot 10^{-4}$	0.51 ± 0.04
		$17.0 \cdot 10^{-4}$	1.2 - $2.4 \cdot 10^{-3}$	0.66 ± 0.04
		$49.0 \cdot 10^{-4}$	2.4 - $10.0 \cdot 10^{-3}$	0.71 ± 0.03
60	40 - 80	$8.5 \cdot 10^{-4}$	6.0 - $12.0 \cdot 10^{-4}$	0.55 ± 0.09
		$17.0 \cdot 10^{-4}$	1.2 - $2.4 \cdot 10^{-3}$	0.68 ± 0.06
		$49.0 \cdot 10^{-4}$	2.4 - $10.0 \cdot 10^{-3}$	0.69 ± 0.04
		$32.0 \cdot 10^{-3}$	1.0 - $10.0 \cdot 10^{-2}$	0.80 ± 0.06
120	80 - 160	$17.0 \cdot 10^{-4}$	1.2 - $2.4 \cdot 10^{-3}$	0.92 ± 0.16
		$49.0 \cdot 10^{-4}$	2.4 - $10.0 \cdot 10^{-3}$	0.64 ± 0.06
		$32.0 \cdot 10^{-3}$	1.0 - $10.0 \cdot 10^{-2}$	0.86 ± 0.07
240	160 - 320	$49.0 \cdot 10^{-4}$	2.4 - $10.0 \cdot 10^{-3}$	0.58 ± 0.10
		$32.0 \cdot 10^{-3}$	1.0 - $10.0 \cdot 10^{-2}$	0.69 ± 0.08
480	320 - 640	$32.0 \cdot 10^{-3}$	1.0 - $10.0 \cdot 10^{-2}$	0.74 ± 0.12
1000	640 - 10000	$32.0 \cdot 10^{-3}$	1.0 - $10.0 \cdot 10^{-2}$	0.81 ± 0.16

Acceptance uncertainty: +3/-3 %

Energy scale uncertainty of ±2 %: -4/+5 %

Normalization error: 4 %

Table 8: The fraction of events with a leading neutron at $x_L = 0.49$ in bins of x and Q^2.

$$0.52 < x_L < 0.58$$

Q^2 GeV^2	Q^2 range	$x_{\rm BJ}$	$x_{\rm BJ}$ range	*ratio* (%) *meas.* ± *stat*
7	4 - 10	$1.1 \cdot 10^{-4}$	8.0 - $15.0 \cdot 10^{-5}$	0.71 ± 0.05
		$2.1 \cdot 10^{-4}$	1.5 - $3.0 \cdot 10^{-4}$	0.70 ± 0.03
		$4.2 \cdot 10^{-4}$	3.0 - $6.0 \cdot 10^{-4}$	0.66 ± 0.04
		$8.5 \cdot 10^{-4}$	6.0 - $12.0 \cdot 10^{-4}$	0.73 ± 0.05
		$17.0 \cdot 10^{-4}$	1.2 - $2.4 \cdot 10^{-3}$	0.76 ± 0.06
15	10 - 20	$2.1 \cdot 10^{-4}$	1.5 - $3.0 \cdot 10^{-4}$	0.71 ± 0.06
		$4.2 \cdot 10^{-4}$	3.0 - $6.0 \cdot 10^{-4}$	0.76 ± 0.04
		$8.5 \cdot 10^{-4}$	6.0 - $12.0 \cdot 10^{-4}$	0.79 ± 0.04
		$17.0 \cdot 10^{-4}$	1.2 - $2.4 \cdot 10^{-3}$	0.72 ± 0.05
		$49.0 \cdot 10^{-4}$	2.4 - $10.0 \cdot 10^{-3}$	0.84 ± 0.05
30	20 - 40	$4.2 \cdot 10^{-4}$	3.0 - $6.0 \cdot 10^{-4}$	0.72 ± 0.07
		$8.5 \cdot 10^{-4}$	6.0 - $12.0 \cdot 10^{-4}$	0.72 ± 0.04
		$17.0 \cdot 10^{-4}$	1.2 - $2.4 \cdot 10^{-3}$	0.79 ± 0.05
		$49.0 \cdot 10^{-4}$	2.4 - $10.0 \cdot 10^{-3}$	0.81 ± 0.04
60	40 - 80	$8.5 \cdot 10^{-4}$	6.0 - $12.0 \cdot 10^{-4}$	0.75 ± 0.10
		$17.0 \cdot 10^{-4}$	1.2 - $2.4 \cdot 10^{-3}$	0.69 ± 0.06
		$49.0 \cdot 10^{-4}$	2.4 - $10.0 \cdot 10^{-3}$	0.71 ± 0.04
		$32.0 \cdot 10^{-3}$	1.0 - $10.0 \cdot 10^{-2}$	0.88 ± 0.06
120	80 - 160	$17.0 \cdot 10^{-4}$	1.2 - $2.4 \cdot 10^{-3}$	0.77 ± 0.15
		$49.0 \cdot 10^{-4}$	2.4 - $10.0 \cdot 10^{-3}$	0.80 ± 0.07
		$32.0 \cdot 10^{-3}$	1.0 - $10.0 \cdot 10^{-2}$	0.88 ± 0.07
240	160 - 320	$49.0 \cdot 10^{-4}$	2.4 - $10.0 \cdot 10^{-3}$	0.83 ± 0.12
		$32.0 \cdot 10^{-3}$	1.0 - $10.0 \cdot 10^{-2}$	0.97 ± 0.09
480	320 - 640	$32.0 \cdot 10^{-3}$	1.0 - $10.0 \cdot 10^{-2}$	0.88 ± 0.13
1000	640 - 10000	$32.0 \cdot 10^{-3}$	1.0 - $10.0 \cdot 10^{-2}$	0.86 ± 0.17

Acceptance uncertainty: +4/-3 %

Energy scale uncertainty of ±2 %: -4/+5 %

Normalization error: 4 %

Table 9: The fraction of events with a leading neutron at $x_L = 0.55$ in bins of x and Q^2.

$0.58 < x_L < 0.64$

Q^2 GeV^2	Q^2 range	$x_{\rm BJ}$	$x_{\rm BJ}$ range	*ratio* (%) *meas.* ± *stat*
7	4 - 10	$1.1 \cdot 10^{-4}$	8.0 - $15.0 \cdot 10^{-5}$	0.78 ± 0.05
		$2.1 \cdot 10^{-4}$	1.5 - $3.0 \cdot 10^{-4}$	0.79 ± 0.04
		$4.2 \cdot 10^{-4}$	3.0 - $6.0 \cdot 10^{-4}$	0.81 ± 0.04
		$8.5 \cdot 10^{-4}$	6.0 - $12.0 \cdot 10^{-4}$	0.78 ± 0.05
		$17.0 \cdot 10^{-4}$	1.2 - $2.4 \cdot 10^{-3}$	0.88 ± 0.06
15	10 - 20	$2.1 \cdot 10^{-4}$	1.5 - $3.0 \cdot 10^{-4}$	0.68 ± 0.06
		$4.2 \cdot 10^{-4}$	3.0 - $6.0 \cdot 10^{-4}$	0.77 ± 0.04
		$8.5 \cdot 10^{-4}$	6.0 - $12.0 \cdot 10^{-4}$	0.78 ± 0.04
		$17.0 \cdot 10^{-4}$	1.2 - $2.4 \cdot 10^{-3}$	0.85 ± 0.05
		$49.0 \cdot 10^{-4}$	2.4 - $10.0 \cdot 10^{-3}$	0.86 ± 0.05
30	20 - 40	$4.2 \cdot 10^{-4}$	3.0 - $6.0 \cdot 10^{-4}$	0.76 ± 0.07
		$8.5 \cdot 10^{-4}$	6.0 - $12.0 \cdot 10^{-4}$	0.80 ± 0.04
		$17.0 \cdot 10^{-4}$	1.2 - $2.4 \cdot 10^{-3}$	0.75 ± 0.04
		$49.0 \cdot 10^{-4}$	2.4 - $10.0 \cdot 10^{-3}$	0.84 ± 0.04
60	40 - 80	$8.5 \cdot 10^{-4}$	6.0 - $12.0 \cdot 10^{-4}$	0.69 ± 0.10
		$17.0 \cdot 10^{-4}$	1.2 - $2.4 \cdot 10^{-3}$	0.83 ± 0.06
		$49.0 \cdot 10^{-4}$	2.4 - $10.0 \cdot 10^{-3}$	0.87 ± 0.05
		$32.0 \cdot 10^{-3}$	1.0 - $10.0 \cdot 10^{-2}$	0.87 ± 0.06
120	80 - 160	$17.0 \cdot 10^{-4}$	1.2 - $2.4 \cdot 10^{-3}$	0.52 ± 0.12
		$49.0 \cdot 10^{-4}$	2.4 - $10.0 \cdot 10^{-3}$	0.80 ± 0.06
		$32.0 \cdot 10^{-3}$	1.0 - $10.0 \cdot 10^{-2}$	0.83 ± 0.06
240	160 - 320	$49.0 \cdot 10^{-4}$	2.4 - $10.0 \cdot 10^{-3}$	0.84 ± 0.12
		$32.0 \cdot 10^{-3}$	1.0 - $10.0 \cdot 10^{-2}$	1.04 ± 0.09
480	320 - 640	$32.0 \cdot 10^{-3}$	1.0 - $10.0 \cdot 10^{-2}$	0.89 ± 0.13
1000	640 - 10000	$32.0 \cdot 10^{-3}$	1.0 - $10.0 \cdot 10^{-2}$	0.82 ± 0.16

Acceptance uncertainty: +4/-4 %

Energy scale uncertainty of ±2 %: -4/+4 %

Normalization error: 4 %

Table 10: The fraction of events with a leading neutron at $x_L = 0.61$ in bins of x and Q^2.

$$0.64 < x_L < 0.7$$

Q^2 GeV^2	Q^2 range	$x_{\rm BJ}$	$x_{\rm BJ}$ range	*ratio* (%) *meas.* ± *stat*
7	4 - 10	$1.1 \cdot 10^{-4}$	8.0 - $15.0 \cdot 10^{-5}$	0.86 ± 0.06
		$2.1 \cdot 10^{-4}$	1.5 - $3.0 \cdot 10^{-4}$	0.91 ± 0.04
		$4.2 \cdot 10^{-4}$	3.0 - $6.0 \cdot 10^{-4}$	0.92 ± 0.05
		$8.5 \cdot 10^{-4}$	6.0 - $12.0 \cdot 10^{-4}$	1.00 ± 0.06
		$17.0 \cdot 10^{-4}$	1.2 - $2.4 \cdot 10^{-3}$	0.85 ± 0.06
15	10 - 20	$2.1 \cdot 10^{-4}$	1.5 - $3.0 \cdot 10^{-4}$	0.93 ± 0.07
		$4.2 \cdot 10^{-4}$	3.0 - $6.0 \cdot 10^{-4}$	0.93 ± 0.04
		$8.5 \cdot 10^{-4}$	6.0 - $12.0 \cdot 10^{-4}$	0.91 ± 0.05
		$17.0 \cdot 10^{-4}$	1.2 - $2.4 \cdot 10^{-3}$	0.97 ± 0.05
		$49.0 \cdot 10^{-4}$	2.4 - $10.0 \cdot 10^{-3}$	0.92 ± 0.05
30	20 - 40	$4.2 \cdot 10^{-4}$	3.0 - $6.0 \cdot 10^{-4}$	0.97 ± 0.08
		$8.5 \cdot 10^{-4}$	6.0 - $12.0 \cdot 10^{-4}$	0.86 ± 0.05
		$17.0 \cdot 10^{-4}$	1.2 - $2.4 \cdot 10^{-3}$	0.86 ± 0.05
		$49.0 \cdot 10^{-4}$	2.4 - $10.0 \cdot 10^{-3}$	0.95 ± 0.04
60	40 - 80	$8.5 \cdot 10^{-4}$	6.0 - $12.0 \cdot 10^{-4}$	0.89 ± 0.11
		$17.0 \cdot 10^{-4}$	1.2 - $2.4 \cdot 10^{-3}$	0.81 ± 0.06
		$49.0 \cdot 10^{-4}$	2.4 - $10.0 \cdot 10^{-3}$	0.92 ± 0.05
		$32.0 \cdot 10^{-3}$	1.0 - $10.0 \cdot 10^{-2}$	0.97 ± 0.07
120	80 - 160	$17.0 \cdot 10^{-4}$	1.2 - $2.4 \cdot 10^{-3}$	0.82 ± 0.15
		$49.0 \cdot 10^{-4}$	2.4 - $10.0 \cdot 10^{-3}$	0.91 ± 0.07
		$32.0 \cdot 10^{-3}$	1.0 - $10.0 \cdot 10^{-2}$	0.95 ± 0.07
240	160 - 320	$49.0 \cdot 10^{-4}$	2.4 - $10.0 \cdot 10^{-3}$	1.04 ± 0.13
		$32.0 \cdot 10^{-3}$	1.0 - $10.0 \cdot 10^{-2}$	0.90 ± 0.09
480	320 - 640	$32.0 \cdot 10^{-3}$	1.0 - $10.0 \cdot 10^{-2}$	1.10 ± 0.14
1000	640 - 10000	$32.0 \cdot 10^{-3}$	1.0 - $10.0 \cdot 10^{-2}$	0.98 ± 0.18

Acceptance uncertainty: +5/-5 %

Energy scale uncertainty of ±2 %: -4/+4 %

Normalization error: 4 %

Table 11: The fraction of events with a leading neutron at $x_L = 0.67$ in bins of x and Q^2.

$0.7 < x_L < 0.76$

Q^2 GeV^2	Q^2 range	$x_{\rm BJ}$	$x_{\rm BJ}$ range	*ratio* (%) *meas.* ± *stat*
7	4 - 10	$1.1 \cdot 10^{-4}$	8.0 - $15.0 \cdot 10^{-5}$	0.95 ± 0.06
		$2.1 \cdot 10^{-4}$	1.5 - $3.0 \cdot 10^{-4}$	0.90 ± 0.04
		$4.2 \cdot 10^{-4}$	3.0 - $6.0 \cdot 10^{-4}$	0.96 ± 0.05
		$8.5 \cdot 10^{-4}$	6.0 - $12.0 \cdot 10^{-4}$	0.98 ± 0.05
		$17.0 \cdot 10^{-4}$	1.2 - $2.4 \cdot 10^{-3}$	0.92 ± 0.06
15	10 - 20	$2.1 \cdot 10^{-4}$	1.5 - $3.0 \cdot 10^{-4}$	0.84 ± 0.07
		$4.2 \cdot 10^{-4}$	3.0 - $6.0 \cdot 10^{-4}$	0.88 ± 0.04
		$8.5 \cdot 10^{-4}$	6.0 - $12.0 \cdot 10^{-4}$	0.94 ± 0.05
		$17.0 \cdot 10^{-4}$	1.2 - $2.4 \cdot 10^{-3}$	1.02 ± 0.06
		$49.0 \cdot 10^{-4}$	2.4 - $10.0 \cdot 10^{-3}$	1.09 ± 0.05
30	20 - 40	$4.2 \cdot 10^{-4}$	3.0 - $6.0 \cdot 10^{-4}$	0.85 ± 0.08
		$8.5 \cdot 10^{-4}$	6.0 - $12.0 \cdot 10^{-4}$	0.83 ± 0.04
		$17.0 \cdot 10^{-4}$	1.2 - $2.4 \cdot 10^{-3}$	0.93 ± 0.05
		$49.0 \cdot 10^{-4}$	2.4 - $10.0 \cdot 10^{-3}$	0.96 ± 0.04
60	40 - 80	$8.5 \cdot 10^{-4}$	6.0 - $12.0 \cdot 10^{-4}$	1.03 ± 0.12
		$17.0 \cdot 10^{-4}$	1.2 - $2.4 \cdot 10^{-3}$	0.87 ± 0.06
		$49.0 \cdot 10^{-4}$	2.4 - $10.0 \cdot 10^{-3}$	0.91 ± 0.05
		$32.0 \cdot 10^{-3}$	1.0 - $10.0 \cdot 10^{-2}$	1.06 ± 0.07
120	80 - 160	$17.0 \cdot 10^{-4}$	1.2 - $2.4 \cdot 10^{-3}$	1.11 ± 0.17
		$49.0 \cdot 10^{-4}$	2.4 - $10.0 \cdot 10^{-3}$	0.83 ± 0.06
		$32.0 \cdot 10^{-3}$	1.0 - $10.0 \cdot 10^{-2}$	0.94 ± 0.07
240	160 - 320	$49.0 \cdot 10^{-4}$	2.4 - $10.0 \cdot 10^{-3}$	0.96 ± 0.13
		$32.0 \cdot 10^{-3}$	1.0 - $10.0 \cdot 10^{-2}$	1.01 ± 0.09
480	320 - 640	$32.0 \cdot 10^{-3}$	1.0 - $10.0 \cdot 10^{-2}$	1.10 ± 0.14
1000	640 - 10000	$32.0 \cdot 10^{-3}$	1.0 - $10.0 \cdot 10^{-2}$	1.16 ± 0.19

Acceptance uncertainty: +5/-5 %

Energy scale uncertainty of ±2 %: -2/+2 %

Normalization error: 4 %

Table 12: The fraction of events with a leading neutron at $x_L = 0.73$ in bins of x and Q^2.

$0.76 < x_L < 0.82$

Q^2 GeV^2	Q^2 range	$x_{\rm BJ}$	$x_{\rm BJ}$ range	*ratio* (%) *meas.* ± *stat*
7	4 - 10	$1.1 \cdot 10^{-4}$	8.0 - $15.0 \cdot 10^{-5}$	0.98 ± 0.06
		$2.1 \cdot 10^{-4}$	1.5 - $3.0 \cdot 10^{-4}$	0.83 ± 0.04
		$4.2 \cdot 10^{-4}$	3.0 - $6.0 \cdot 10^{-4}$	0.90 ± 0.04
		$8.5 \cdot 10^{-4}$	6.0 - $12.0 \cdot 10^{-4}$	0.86 ± 0.05
		$17.0 \cdot 10^{-4}$	1.2 - $2.4 \cdot 10^{-3}$	0.93 ± 0.06
15	10 - 20	$2.1 \cdot 10^{-4}$	1.5 - $3.0 \cdot 10^{-4}$	0.94 ± 0.07
		$4.2 \cdot 10^{-4}$	3.0 - $6.0 \cdot 10^{-4}$	0.89 ± 0.04
		$8.5 \cdot 10^{-4}$	6.0 - $12.0 \cdot 10^{-4}$	0.90 ± 0.05
		$17.0 \cdot 10^{-4}$	1.2 - $2.4 \cdot 10^{-3}$	0.83 ± 0.05
		$49.0 \cdot 10^{-4}$	2.4 - $10.0 \cdot 10^{-3}$	0.87 ± 0.05
30	20 - 40	$4.2 \cdot 10^{-4}$	3.0 - $6.0 \cdot 10^{-4}$	0.77 ± 0.07
		$8.5 \cdot 10^{-4}$	6.0 - $12.0 \cdot 10^{-4}$	0.89 ± 0.05
		$17.0 \cdot 10^{-4}$	1.2 - $2.4 \cdot 10^{-3}$	0.82 ± 0.05
		$49.0 \cdot 10^{-4}$	2.4 - $10.0 \cdot 10^{-3}$	0.89 ± 0.04
60	40 - 80	$8.5 \cdot 10^{-4}$	6.0 - $12.0 \cdot 10^{-4}$	0.91 ± 0.11
		$17.0 \cdot 10^{-4}$	1.2 - $2.4 \cdot 10^{-3}$	0.83 ± 0.06
		$49.0 \cdot 10^{-4}$	2.4 - $10.0 \cdot 10^{-3}$	0.89 ± 0.05
		$32.0 \cdot 10^{-3}$	1.0 - $10.0 \cdot 10^{-2}$	0.98 ± 0.07
120	80 - 160	$17.0 \cdot 10^{-4}$	1.2 - $2.4 \cdot 10^{-3}$	1.22 ± 0.18
		$49.0 \cdot 10^{-4}$	2.4 - $10.0 \cdot 10^{-3}$	0.67 ± 0.06
		$32.0 \cdot 10^{-3}$	1.0 - $10.0 \cdot 10^{-2}$	0.89 ± 0.07
240	160 - 320	$49.0 \cdot 10^{-4}$	2.4 - $10.0 \cdot 10^{-3}$	0.93 ± 0.12
		$32.0 \cdot 10^{-3}$	1.0 - $10.0 \cdot 10^{-2}$	0.84 ± 0.08
480	320 - 640	$32.0 \cdot 10^{-3}$	1.0 - $10.0 \cdot 10^{-2}$	0.60 ± 0.10
1000	640 - 10000	$32.0 \cdot 10^{-3}$	1.0 - $10.0 \cdot 10^{-2}$	0.89 ± 0.17

Acceptance uncertainty: +5/-6 %

Energy scale uncertainty of ±2 %: +2/-1 %

Normalization error: 4 %

Table 13: The fraction of events with a leading neutron at $x_L = 0.79$ in bins of x and Q^2.

$$0.82 < x_L < 0.88$$

Q^2 GeV^2	Q^2 range	$x_{\rm BJ}$	$x_{\rm BJ}$ range	*ratio* (%) *meas.* ± *stat*
7	4 - 10	$1.1 \cdot 10^{-4}$	$8.0 - 15.0 \cdot 10^{-5}$	0.73 ± 0.05
		$2.1 \cdot 10^{-4}$	$1.5 - 3.0 \cdot 10^{-4}$	0.71 ± 0.03
		$4.2 \cdot 10^{-4}$	$3.0 - 6.0 \cdot 10^{-4}$	0.65 ± 0.04
		$8.5 \cdot 10^{-4}$	$6.0 - 12.0 \cdot 10^{-4}$	0.74 ± 0.05
		$17.0 \cdot 10^{-4}$	$1.2 - 2.4 \cdot 10^{-3}$	0.74 ± 0.05
15	10 - 20	$2.1 \cdot 10^{-4}$	$1.5 - 3.0 \cdot 10^{-4}$	0.72 ± 0.06
		$4.2 \cdot 10^{-4}$	$3.0 - 6.0 \cdot 10^{-4}$	0.70 ± 0.03
		$8.5 \cdot 10^{-4}$	$6.0 - 12.0 \cdot 10^{-4}$	0.70 ± 0.04
		$17.0 \cdot 10^{-4}$	$1.2 - 2.4 \cdot 10^{-3}$	0.72 ± 0.04
		$49.0 \cdot 10^{-4}$	$2.4 - 10.0 \cdot 10^{-3}$	0.75 ± 0.04
30	20 - 40	$4.2 \cdot 10^{-4}$	$3.0 - 6.0 \cdot 10^{-4}$	0.73 ± 0.07
		$8.5 \cdot 10^{-4}$	$6.0 - 12.0 \cdot 10^{-4}$	0.65 ± 0.04
		$17.0 \cdot 10^{-4}$	$1.2 - 2.4 \cdot 10^{-3}$	0.64 ± 0.04
		$49.0 \cdot 10^{-4}$	$2.4 - 10.0 \cdot 10^{-3}$	0.68 ± 0.03
60	40 - 80	$8.5 \cdot 10^{-4}$	$6.0 - 12.0 \cdot 10^{-4}$	0.61 ± 0.09
		$17.0 \cdot 10^{-4}$	$1.2 - 2.4 \cdot 10^{-3}$	0.69 ± 0.05
		$49.0 \cdot 10^{-4}$	$2.4 - 10.0 \cdot 10^{-3}$	0.61 ± 0.04
		$32.0 \cdot 10^{-3}$	$1.0 - 10.0 \cdot 10^{-2}$	0.66 ± 0.05
120	80 - 160	$17.0 \cdot 10^{-4}$	$1.2 - 2.4 \cdot 10^{-3}$	0.72 ± 0.13
		$49.0 \cdot 10^{-4}$	$2.4 - 10.0 \cdot 10^{-3}$	0.63 ± 0.05
		$32.0 \cdot 10^{-3}$	$1.0 - 10.0 \cdot 10^{-2}$	0.60 ± 0.05
240	160 - 320	$49.0 \cdot 10^{-4}$	$2.4 - 10.0 \cdot 10^{-3}$	0.43 ± 0.08
		$32.0 \cdot 10^{-3}$	$1.0 - 10.0 \cdot 10^{-2}$	0.40 ± 0.05
480	320 - 640	$32.0 \cdot 10^{-3}$	$1.0 - 10.0 \cdot 10^{-2}$	0.40 ± 0.08
1000	640 - 10000	$32.0 \cdot 10^{-3}$	$1.0 - 10.0 \cdot 10^{-2}$	0.57 ± 0.13

Acceptance uncertainty: +6/-6 %

Energy scale uncertainty of ±2 %: +5/-8 %

Normalization error: 4 %

Table 14: The fraction of events with a leading neutron at $x_L = 0.85$ in bins of x and Q^2.

$0.88 < x_L < 1$

Q^2 GeV^2	Q^2 range	$x_{\rm BJ}$	$x_{\rm BJ}$ range	*ratio* (%) *meas.* ± *stat*
7	4 - 10	$1.1 \cdot 10^{-4}$	$8.0 - 15.0 \cdot 10^{-5}$	0.52 ± 0.04
		$2.1 \cdot 10^{-4}$	$1.5 - 3.0 \cdot 10^{-4}$	0.53 ± 0.03
		$4.2 \cdot 10^{-4}$	$3.0 - 6.0 \cdot 10^{-4}$	0.48 ± 0.03
		$8.5 \cdot 10^{-4}$	$6.0 - 12.0 \cdot 10^{-4}$	0.41 ± 0.03
		$17.0 \cdot 10^{-4}$	$1.2 - 2.4 \cdot 10^{-3}$	0.45 ± 0.04
15	10 - 20	$2.1 \cdot 10^{-4}$	$1.5 - 3.0 \cdot 10^{-4}$	0.51 ± 0.04
		$4.2 \cdot 10^{-4}$	$3.0 - 6.0 \cdot 10^{-4}$	0.45 ± 0.02
		$8.5 \cdot 10^{-4}$	$6.0 - 12.0 \cdot 10^{-4}$	0.44 ± 0.03
		$17.0 \cdot 10^{-4}$	$1.2 - 2.4 \cdot 10^{-3}$	0.43 ± 0.03
		$49.0 \cdot 10^{-4}$	$2.4 - 10.0 \cdot 10^{-3}$	0.38 ± 0.03
30	20 - 40	$4.2 \cdot 10^{-4}$	$3.0 - 6.0 \cdot 10^{-4}$	0.40 ± 0.04
		$8.5 \cdot 10^{-4}$	$6.0 - 12.0 \cdot 10^{-4}$	0.39 ± 0.03
		$17.0 \cdot 10^{-4}$	$1.2 - 2.4 \cdot 10^{-3}$	0.41 ± 0.03
		$49.0 \cdot 10^{-4}$	$2.4 - 10.0 \cdot 10^{-3}$	0.43 ± 0.02
60	40 - 80	$8.5 \cdot 10^{-4}$	$6.0 - 12.0 \cdot 10^{-4}$	0.52 ± 0.07
		$17.0 \cdot 10^{-4}$	$1.2 - 2.4 \cdot 10^{-3}$	0.34 ± 0.03
		$49.0 \cdot 10^{-4}$	$2.4 - 10.0 \cdot 10^{-3}$	0.38 ± 0.03
		$32.0 \cdot 10^{-3}$	$1.0 - 10.0 \cdot 10^{-2}$	0.34 ± 0.03
120	80 - 160	$17.0 \cdot 10^{-4}$	$1.2 - 2.4 \cdot 10^{-3}$	0.45 ± 0.09
		$49.0 \cdot 10^{-4}$	$2.4 - 10.0 \cdot 10^{-3}$	0.36 ± 0.04
		$32.0 \cdot 10^{-3}$	$1.0 - 10.0 \cdot 10^{-2}$	0.35 ± 0.04
240	160 - 320	$49.0 \cdot 10^{-4}$	$2.4 - 10.0 \cdot 10^{-3}$	0.41 ± 0.07
		$32.0 \cdot 10^{-3}$	$1.0 - 10.0 \cdot 10^{-2}$	0.22 ± 0.04
480	320 - 640	$32.0 \cdot 10^{-3}$	$1.0 - 10.0 \cdot 10^{-2}$	0.25 ± 0.06
1000	640 - 10000	$32.0 \cdot 10^{-3}$	$1.0 - 10.0 \cdot 10^{-2}$	0.20 ± 0.07

Acceptance uncertainty: +6/-6 %

Energy scale uncertainty of ±2 %: +25/-26 %

Normalization error: 4 %

Table 15: The fraction of events with a leading neutron at $x_L = 0.94$ in bins of x and Q^2.

$0.2 < x_L < 0.64$

Q^2 GeV^2	Q^2 range	y	y range	*ratio* (%) *meas.* ± *stat*
0.11	0.10 - 0.13	0.60	0.54 - 0.64	3.15 ± 0.43
		0.70	0.64 - 0.74	2.85 ± 0.39
0.15	0.13 - 0.17	0.40	0.37 - 0.45	3.72 ± 0.47
		0.50	0.45 - 0.54	2.76 ± 0.34
		0.60	0.54 - 0.64	3.49 ± 0.39
		0.70	0.64 - 0.74	2.76 ± 0.41
0.20	0.17 - 0.21	0.26	0.23 - 0.30	3.23 ± 0.41
		0.33	0.30 - 0.37	3.09 ± 0.38
		0.40	0.37 - 0.45	3.41 ± 0.38
		0.50	0.45 - 0.54	3.70 ± 0.43
		0.60	0.54 - 0.64	2.96 ± 0.43
		0.70	0.64 - 0.74	3.98 ± 0.63
0.25	0.21 - 0.27	0.20	0.16 - 0.23	3.23 ± 0.28
		0.26	0.23 - 0.30	3.46 ± 0.31
		0.33	0.30 - 0.37	3.24 ± 0.33
		0.40	0.37 - 0.45	4.04 ± 0.39
		0.50	0.45 - 0.54	3.28 ± 0.39
		0.60	0.54 - 0.64	3.83 ± 0.49
0.30	0.27 - 0.35	0.12	0.08 - 0.16	3.88 ± 0.29
		0.20	0.16 - 0.23	3.82 ± 0.30
		0.26	0.23 - 0.30	3.03 ± 0.30
		0.33	0.30 - 0.37	2.86 ± 0.32
		0.40	0.37 - 0.45	3.36 ± 0.40
		0.50	0.45 - 0.54	2.97 ± 0.41
0.40	0.35 - 0.45	0.12	0.08 - 0.16	3.05 ± 0.28
		0.20	0.16 - 0.23	3.02 ± 0.30
		0.26	0.23 - 0.30	3.61 ± 0.38
		0.33	0.30 - 0.37	3.94 ± 0.45
		0.40	0.37 - 0.45	4.45 ± 0.52
0.50	0.45 - 0.58	0.12	0.08 - 0.16	3.35 ± 0.33
		0.20	0.16 - 0.23	3.02 ± 0.34
		0.26	0.23 - 0.30	2.50 ± 0.36
0.65	0.58 - 0.74	0.20	0.16 - 0.23	4.01 ± 0.54
		0.26	0.23 - 0.30	3.46 ± 0.68

Acceptance uncertainty: +2/-2 %

Energy scale uncertainty of ±2 %: -4/+4 %

Normalization error: 4 %

Table 16: The fraction of events with a leading neutron at $x_L = 0.42$ in bins of y and Q^2 for the BPC region.

$0.64 < x_L < 0.82$

Q^2 GeV^2	Q^2 range	y	y range	*ratio* (%) *meas.* ± *stat*
0.11	0.10 - 0.13	0.60	0.54 - 0.64	2.62 ± 0.38
		0.70	0.64 - 0.74	2.91 ± 0.39
0.15	0.13 - 0.17	0.40	0.37 - 0.45	2.30 ± 0.36
		0.50	0.45 - 0.54	2.58 ± 0.32
		0.60	0.54 - 0.64	2.35 ± 0.31
		0.70	0.64 - 0.74	2.17 ± 0.36
0.20	0.17 - 0.21	0.26	0.23 - 0.30	2.25 ± 0.33
		0.33	0.30 - 0.37	2.94 ± 0.36
		0.40	0.37 - 0.45	2.69 ± 0.33
		0.50	0.45 - 0.54	2.30 ± 0.33
		0.60	0.54 - 0.64	2.81 ± 0.41
		0.70	0.64 - 0.74	2.16 ± 0.45
0.25	0.21 - 0.27	0.20	0.16 - 0.23	2.53 ± 0.24
		0.26	0.23 - 0.30	2.46 ± 0.25
		0.33	0.30 - 0.37	2.63 ± 0.28
		0.40	0.37 - 0.45	3.04 ± 0.33
		0.50	0.45 - 0.54	2.23 ± 0.31
		0.60	0.54 - 0.64	2.13 ± 0.36
0.30	0.27 - 0.35	0.12	0.08 - 0.16	2.55 ± 0.23
		0.20	0.16 - 0.23	2.64 ± 0.24
		0.26	0.23 - 0.30	2.03 ± 0.24
		0.33	0.30 - 0.37	2.24 ± 0.28
		0.40	0.37 - 0.45	2.12 ± 0.31
		0.50	0.45 - 0.54	2.61 ± 0.38
0.40	0.35 - 0.45	0.12	0.08 - 0.16	2.73 ± 0.25
		0.20	0.16 - 0.23	2.70 ± 0.28
		0.26	0.23 - 0.30	2.64 ± 0.31
		0.33	0.30 - 0.37	2.53 ± 0.35
		0.40	0.37 - 0.45	2.78 ± 0.40
0.50	0.45 - 0.58	0.12	0.08 - 0.16	2.63 ± 0.29
		0.20	0.16 - 0.23	2.87 ± 0.32
		0.26	0.23 - 0.30	2.37 ± 0.34
0.65	0.58 - 0.74	0.20	0.16 - 0.23	1.77 ± 0.34
		0.26	0.23 - 0.30	2.56 ± 0.57

Acceptance uncertainty: +5/-5 %

Energy scale uncertainty of ±2 %: -2/+2 %

Normalization error: 4 %

Table 17: The fraction of events with a leading neutron at $x_L = 0.73$ in bins of y and Q^2 for the BPC region.

$0.82 < x_L < 1$

Q^2 GeV^2	Q^2 range	y	y range	*ratio* (%) *meas.* ± *stat*
0.11	0.10 - 0.13	0.60	0.54 - 0.64	1.15 ± 0.23
		0.70	0.64 - 0.74	0.87 ± 0.19
0.15	0.13 - 0.17	0.40	0.37 - 0.45	1.19 ± 0.23
		0.50	0.45 - 0.54	1.10 ± 0.19
		0.60	0.54 - 0.64	0.82 ± 0.17
		0.70	0.64 - 0.74	0.89 ± 0.21
0.20	0.17 - 0.21	0.26	0.23 - 0.30	1.03 ± 0.20
		0.33	0.30 - 0.37	1.18 ± 0.20
		0.40	0.37 - 0.45	1.06 ± 0.19
		0.50	0.45 - 0.54	1.00 ± 0.19
		0.60	0.54 - 0.64	1.16 ± 0.24
		0.70	0.64 - 0.74	0.82 ± 0.25
0.25	0.21 - 0.27	0.20	0.16 - 0.23	0.96 ± 0.13
		0.26	0.23 - 0.30	0.79 ± 0.13
		0.33	0.30 - 0.37	1.41 ± 0.19
		0.40	0.37 - 0.45	1.03 ± 0.17
		0.50	0.45 - 0.54	0.94 ± 0.18
		0.60	0.54 - 0.64	1.09 ± 0.23
0.30	0.27 - 0.35	0.12	0.08 - 0.16	1.47 ± 0.16
		0.20	0.16 - 0.23	1.33 ± 0.15
		0.26	0.23 - 0.30	0.95 ± 0.15
		0.33	0.30 - 0.37	0.93 ± 0.16
		0.40	0.37 - 0.45	0.86 ± 0.18
		0.50	0.45 - 0.54	1.14 ± 0.23
0.40	0.35 - 0.45	0.12	0.08 - 0.16	1.33 ± 0.16
		0.20	0.16 - 0.23	1.15 ± 0.16
		0.26	0.23 - 0.30	1.12 ± 0.18
		0.33	0.30 - 0.37	0.93 ± 0.19
		0.40	0.37 - 0.45	0.92 ± 0.21
0.50	0.45 - 0.58	0.12	0.08 - 0.16	1.11 ± 0.17
		0.20	0.16 - 0.23	0.94 ± 0.17
		0.26	0.23 - 0.30	1.40 ± 0.24
0.65	0.58 - 0.74	0.20	0.16 - 0.23	0.92 ± 0.22
		0.26	0.23 - 0.30	1.21 ± 0.35

Acceptance uncertainty: +6/-6 %

Energy scale uncertainty of ±2 %: +14/-16 %

Normalization error: 4 %

Table 18: The fraction of events with a leading neutron at $x_L = 0.91$ in bins of y and Q^2 for the BPC region.

References

[1] ZEUS Collaboration, M. Derrick et al., Phys. Lett. B384 (1996) 388.

[2] H1 Collaboration, C. Adloff et al., Eur. Phys. J. C6 (1999) 587.

[3] ZEUS Collaboration, J. Breitweg et al., Nucl. Phys. B596 (2001) 3.

[4] ZEUS Collaboration, J. Breitweg et al., Eur. Phys. J. C1 (1998) 81.

[5] ZEUS Collaboration, J. Breitweg et al., Eur. Phys. J. C2 (1998) 237.

[6] H1 Collaboration, C. Adloff et al., Nucl. Phys. B619 (2001) 3.

[7] L. Frankfurt, W. Koepf and M. Strikman, Phys. Lett. B405 (1997) 367.

[8] L. Trentadue and G. Veneziano, Phys. Lett. B323 (1994) 201;
L. Trentadue, Nucl. Phys. Proc. Suppl. 39B,C (1995) 50;
L. Trentadue, Nucl. Phys. Proc. Suppl. 64 (1998) 152;
M. Grazzini, L. Trentadue, and G. Veneziano, Nucl. Phys. B519 (1998) 394;
For applications to HERA, see also
D. Graudenz, Nucl. Phys. B432 (1994) 351;
D. de Florian and R. Sassot, Phys. Rev. D56 (1997) 426;
D. de Florian and R. Sassot, Phys. Rev. D58 (1998) 054003.

[9] J.C. Collins, Phys. Rev. D57 (1998) 3051; Erratum - ibid, D61 (2000) 019902.

[10] J. Benecke et al., Phys. Rev. 188 (1969) 2159.

[11] T.T. Chou and C.N. Yang, Phys. Rev. D50 (1994) 590.

[12] A. Edin, G. Ingelman, and J. Rathsman, Phys. Lett. B366 (1996) 371;
A. Edin, G. Ingelman, and J. Rathsman, Z. Phys. C75 (1997) 57.

[13] H. Yukawa, Proc. Phys. Math. Soc. Japan 17 (1935) 48.

[14] J.D. Sullivan, Phys. Rev. D5 (1972) 1732.

[15] M. Bishari, Phys. Lett. B38 (1972) 510.

[16] R.D. Field and G.C. Fox, Nucl. Phys. B80 (1974) 367.

[17] V.R. Zoller, Z. Phys. C53 (1992) 443.

[18] B. Kopeliovich, B. Povh and I. Potashnikova, Z. Phys. C73 (1996) 125.

[19] A. Szczurek, N.N. Nikolaev and J. Speth, Phys. Lett. B428 (1998) 383.

[20] S.N. Ganguli and D.P. Roy, Phys. Rep. 67 (1980) 201.

[21] B.G. Zakharov and V.N. Sergeev, Sov. J. Nucl. Phys. 38 (1983) 947;
B.G. Zakharov and V.N. Sergeev, Sov. J. Nucl. Phys. 39 (1984) 448.

[22] M. Lusignoli, P. Pistilli and F. Rapuano, Nucl. Phys. B155 (1979) 394.

[23] P.D.B. Collins, *An Introduction to Regge Theory and High Energy Physics*, Cambridge University Press (1977).

[24] A.R. Erwin et al., Phys. Rev. Lett. 6 (1961) 628.

[25] E. Pickup, D.K. Robinson, and E.O. Salant, Phys. Rev. Lett. 7 (1961) 192; Erratum - ibid, 472.

[26] B. Robinson et al., Phys. Rev. Lett. 34 (1975) 1475.

[27] J. Engler et al., Nucl. Phys. B84 (1975) 70.

[28] W. Flauger and F. Mönnig, Nucl. Phys. B109 (1976) 347.

[29] J. Hanlon et al., Phys. Rev. Lett. 37 (1976) 967;
J. Hanlon et al., Phys. Rev. D20 (1979) 2135.

[30] G. Hartner, Ph.D. Thesis, McGill University (1977), (unpublished).

[31] Y. Eisenberg et al., Nucl. Phys. B135 (1978) 189.

[32] V. Blobel et al., Nucl. Phys. B135 (1978) 379.

[33] H. Abramowicz et al., Nucl. Phys. B166 (1980) 62.

[34] G. Bellettini et al., Phys. Lett. B45 (1973) 69. Phys. Rev. D60 (1999) 114023.

[35] N.N. Nikolaev, J. Speth and B.G. Zakharov, hep-ph/9708290 (1997).

[36] U. D'Alesio and H.J. Pirner, Eur. Phys. J. A7 (2000) 109.

[37] ZEUS Collaboration, M. Derrick et al., Z. Phys. C72 (1996) 399.

[38] NA24 Collaboration, C. De Marzo et al., Phys. Rev. D36 (1987) 8.

[39] WA70 Collaboration, M. Bonesini et al., Z. Phys. C37 (1988) 535.

[40] NA3 Collaboration, J. Badier et al., Z. Phys. C18 (1983) 281.

[41] NA10 Collaboration, B. Betev et al., Z. Phys. C28 (1985) 15.

[42] E537 Collaboration, E. Anassontzis et al., Phys. Rev. D38 (1988) 1377.

[43] E615 Collaboration, J.S. Conway et al., Phys. Rev. D39 (1989) 92.

[44] E609 Collaboration, A. Bordner et al., Z. Phys. C72 (1996) 249.

[45] ZEUS Collaboration, U. Holm (ed.), *The ZEUS Detector*, Status Report (unpublished), DESY, 1993, available on http://www-zeus.desy.de/bluebook/bluebook.html.

[46] N. Harnew et al., Nucl. Instr. and Meth. A279 (1989) 290;
B. Foster et al., Nucl. Phys. Proc. Suppl. 32 (1993) 181;
B. Foster et al., Nucl. Instr. and Meth. A338 (1994) 254.

[47] M. Derrick et al., Nucl. Instr. and Meth. A309 (1991) 77;
A. Andresen et al., Nucl. Instr. and Meth. A309 (1991) 101;
A. Caldwell et al., Nucl. Instr. and Meth. A321 (1992) 356;
A. Bernstein et al.,Nucl. Instr. and Meth. A336 (1993) 23.

[48] ZEUS Collaboration, J. Breitweg et al., Phys. Lett. B407 (1997) 432.

[49] ZEUS Collaboration, M. Derrick et al., Phys. Lett. B293 (1992) 465;
ZEUS Collaboration, M. Derrick et al., Z. Phys. C63 (1994) 391;
J. Andruszkow et al., Preprint DESY 01-041, 2001.

[50] S. Bhadra et al., Nucl. Instr. and Meth. A394 (1997) 121.

[51] S. Bhadra et al., *Proceedings of the Seventh International Conference on Calorimetry in High Energy Physics*, Tucson, Arizona, USA, November 9-14, 1997, E. Cheu et al. (eds.), World Scientific, Singapore (1998), p. 295.

[52] S. Bhadra et al., Nucl. Instr. and Meth. A354 (1995) 479.

[53] H. Holtmann et al., Phys. Lett. B338 (1994) 363.

[54] S. Bentvelsen, J. Engelen and P. Kooijman, *Proceedings of the 1991 Workshop on Physics at HERA*, Volume 1, W. Buchmüller and G. Ingelman (eds.) DESY, Hamburg (1992), p. 23;
K. C. Hoeger, ibid., p. 43.

[55] ZEUS Collaboration, M. Derrick et al., Z. Phys. C65 (1995) 379.

[56] GEANT 3.13, R. Brun et al., CERN-DD/EE/84-1 (1987).

[57] A. Arbuzov et al., Comp. Phys. Comm. 94 (1996) 128.

[58] ZEUS Collaboration, S. Chekanov et al., Nucl. Phys. B627 (2002) 3.

[59] A. Donnachie and P. V. Landshoff, Phys. Lett. B296 (1992) 227;
A. Donnachie and P. V. Landshoff, Phys. Lett. B437 (1998) 408.

[60] M. Klasen and G. Kramer, Phys. Lett. B508 (2001) 259.

[61] R.D. Peccei and A. Pignotti, Phys. Rev. Lett. 26 (1971) 1076.

[62] ZEUS Collaboration, J. Breitweg et al., Phys. Lett. B487 (2000) 53.

[63] ZEUS Collaboration, J. Breitweg et al., Eur. Phys. J. C7 (1999) 609.

[64] ZEUS Collaboration, M. Derrick et al., Z. Phys. C68 (1995) 569.

[65] S.D. Drell and K. Hiida, Phys. Rev. Lett. 7 (1961) 199;
R.T. Deck, Phys. Rev. Lett. 13 (1964) 169.

[66] A.W. Thomas and C. Boros, Eur. Phys. J. C9 (1999) 267.

[67] N.N. Nikolaev et al., Phys. Rev. D60 (1999) 014004.

[68] J. Pumplin, Phys. Rev. D7 (1973) 795;
J. Pumplin, Phys. Rev. D8 (1973) 2249.

[69] J. Erwin et al., Phys. Rev. Lett. 35 (1975) 980.

[70] P.D. Higgins et al., Phys. Rev. D19 (1979) 731.

[71] S.J. Barish et al., Phys. Rev. D12 (1975) 1260.

[72] F.T. Dao et al., Phys. Rev. Lett. 30 (1973) 34.

[73] R. Vogt, Prog. Part. Nucl. Phys. 45 (2000) S105.

[74] E.M. Levin and L.L. Frankfurt, Pis'ma Zh. Eksp. Teor. Fiz. 2 (1965) 105 [JETP Lett. 2 (1965) 65];
H.J. Lipkin and F. Scheck, Phys. Rev. Lett. 16 (1966) 71;
J.J.J. Kokkedee and L. Van Hove, Nuovo Cimento A42 (1966) 711.

[75] A.E.L. Dieperink and S.J. Pollock, Z. Phys. A348 (1994) 117.

[76] M. Glück, E. Reya and A. Vogt, Z. Phys. C53 (1992) 651;
M. Glück, E. Reya and A. Vogt, Z. Phys. C53 (1992) 127;
M. Glück, E. Reya and A. Vogt, Z. Phys. C67 (1995) 433.

[77] P. J. Sutton et al., Phys. Rev. D45 (1992) 2349.

[78] G. Altarelli et al., Nucl. Phys. B69 (1974) 531.

[79] G. Altarelli, S. Petrarca and F. Rapuano, Phys. Lett. B373 (1996) 200.

[80] N.N. Nikolaev, J. Speth and V.R. Zoller, Phys. Lett. B473 (2000) 157.

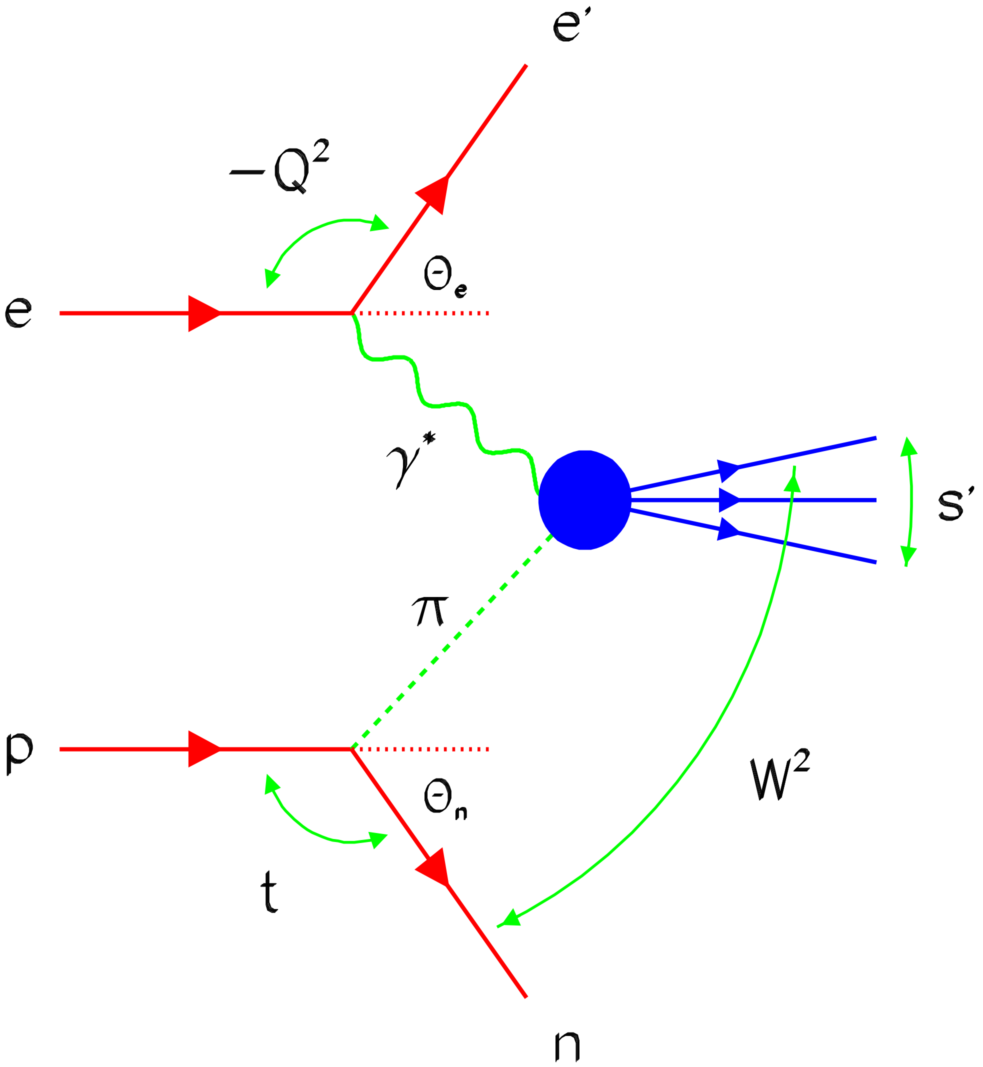

Figure 1: A schematic diagram for the one-pion-exchange model as applied to $ep \rightarrow e'Xn$ showing the Lorentz invariant variables s', Q^2, W^2 and t. Also shown is the definition of the scattering angle of the positron, θ_e, and the production angle of the neutron, θ_n. In the ZEUS coordinate system, the polar angle of the positron is $\theta = \pi - \theta_e$.

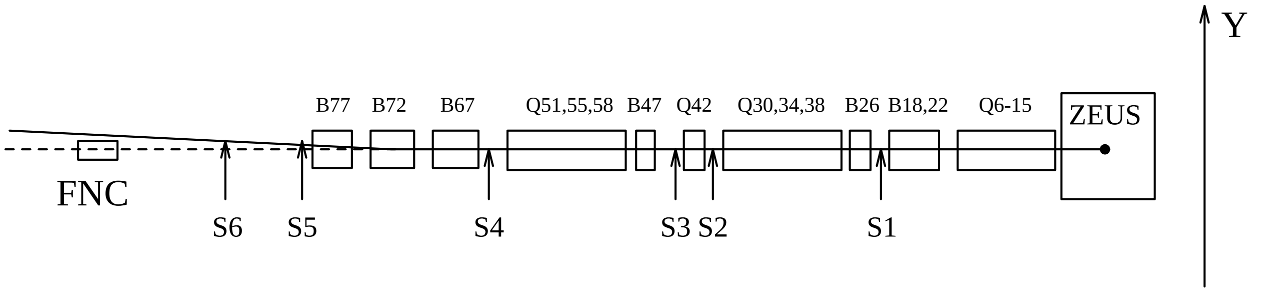

Figure 2: A schematic elevation view of the forward proton beam line from the central detector to the FNC at $Z = +106$ m. Magnets are labelled by B (dipoles) or Q (quadrupoles) and a number which is their nominal distance from the interaction point in meters. S1 through S6 label the positions of the six leading proton spectrometer (LPS) stations. Between 65 and 80 m, the proton beam line is bent upwards by 6 mrad by three bending magnets which form a momentum analyzer for stations S5 and S6 of the LPS. The neutron exit window is located at $Z = +96$ m, immediately following S6.

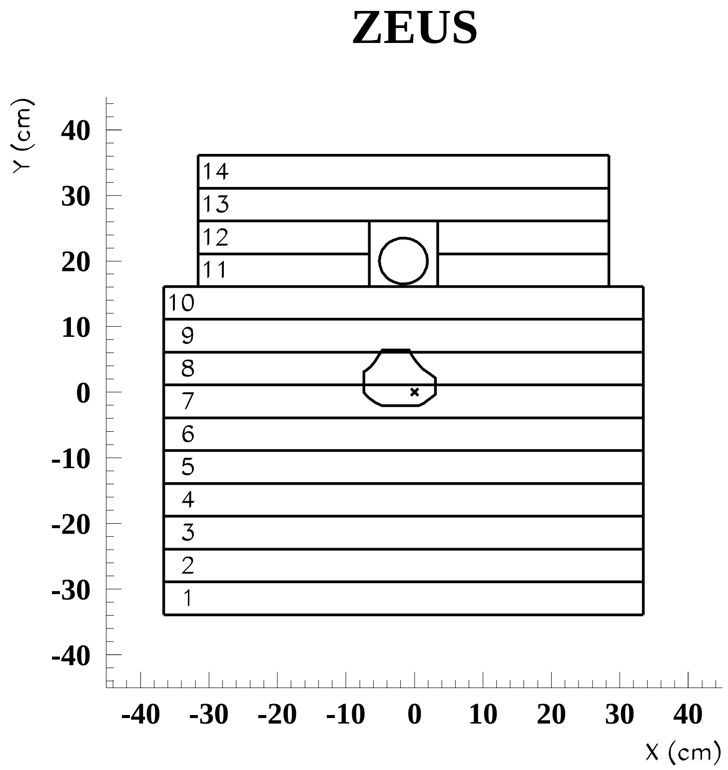

Figure 3: A schematic view of the FNC, looking towards the interaction region. The calorimeter is segmented vertically into 14 towers. The window of geometric acceptance defined by the apertures of the HERA beam-line elements is outlined in towers 7–9. The zero-degree point is marked by an ×. Towers 11 and 12 have a 10×10 cm^2 hole to accommodate the proton beampipe.

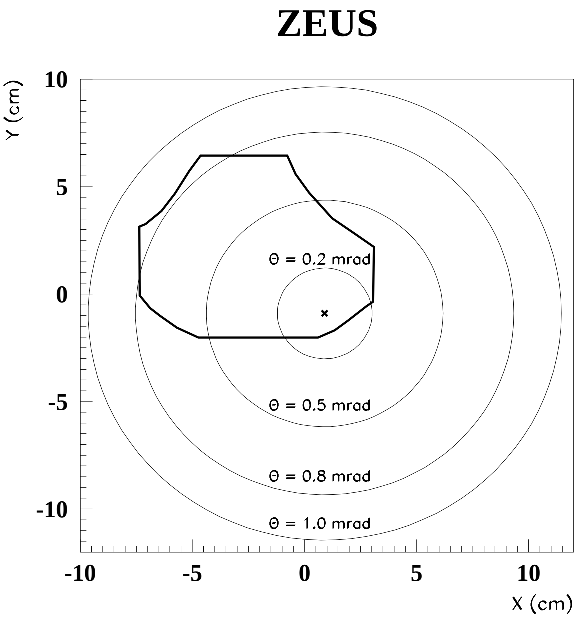

Figure 4: Contours of constant neutron production angle compared to the window of the geometric acceptance defined by the apertures of the HERA beam-line elements (thick irregular curve). The zero-degree point is marked by an ×.

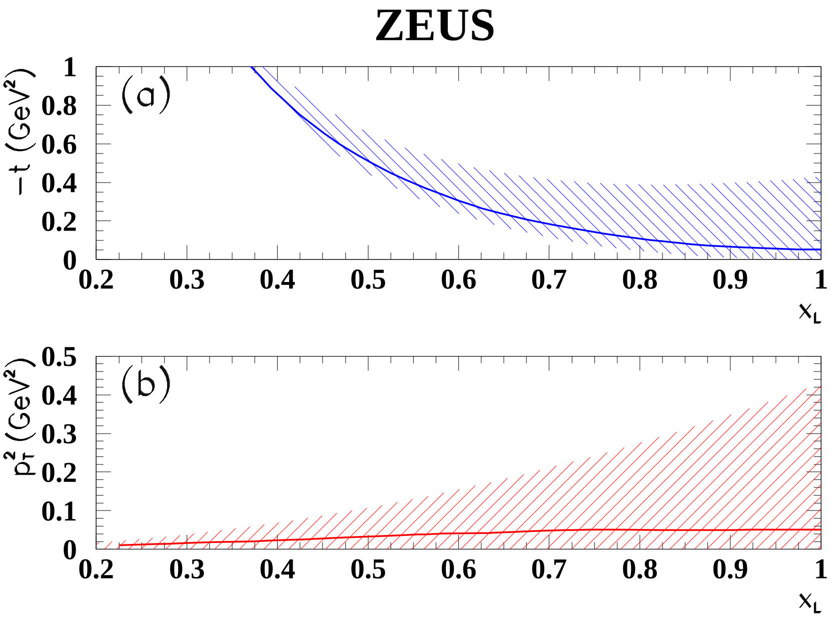

Figure 5: The kinematic regions in (a) t and (b) p_T^2 covered by the angular acceptance of the FNC (θ <0.8 mrad) are shown as shaded bands. The solid lines indicate the average t and p_T^2 values, uncorrected for acceptance, as a function of x_L.

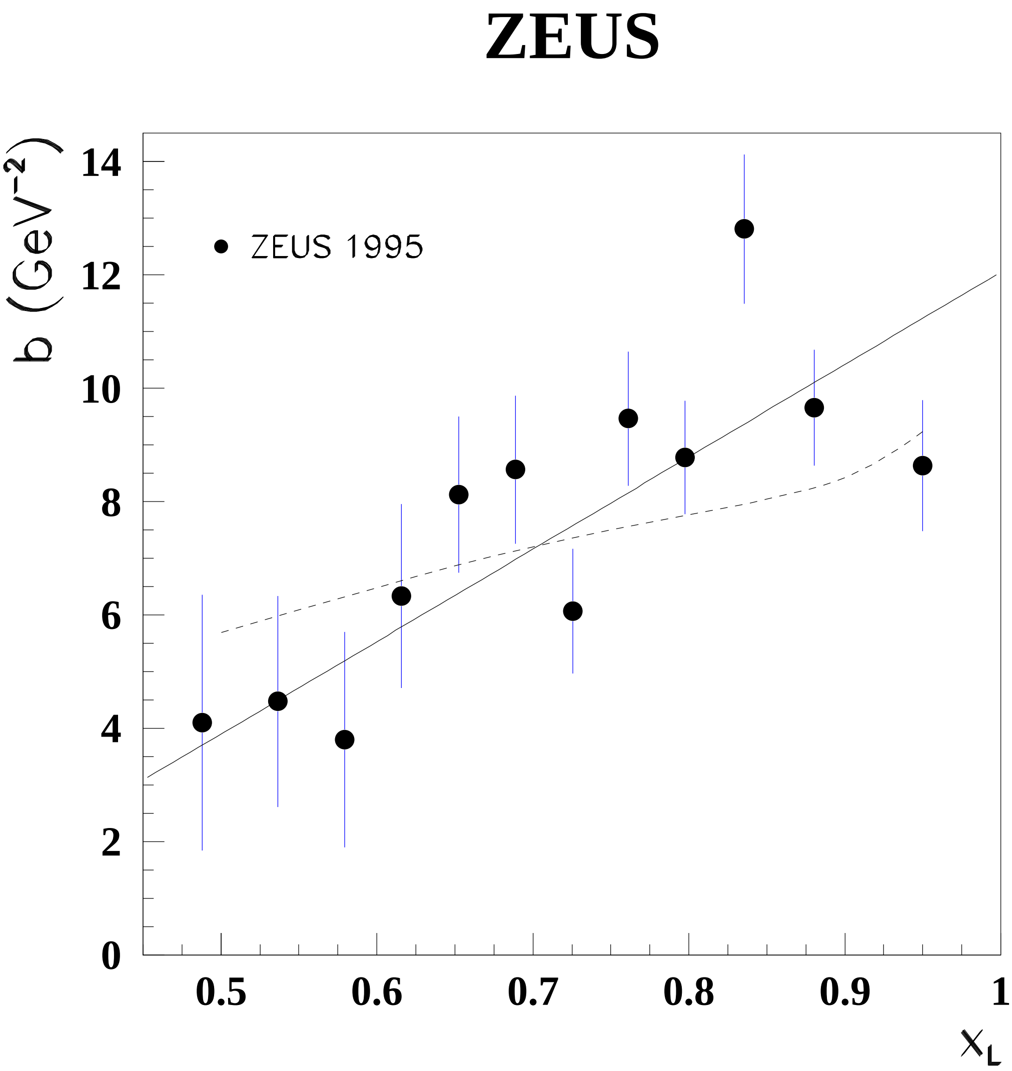

Figure 6: The slope, b, of the exponential p_T^2 distribution as a function of x_L for the 1995 DIS data set. The solid line is given by $b(x_L) = (16.3x_L - 4.25)$ GeV^{-2}. The dashed line is the result obtained using the effective flux of Eq. (8). The vertical error bars display the statistical uncertainties only.

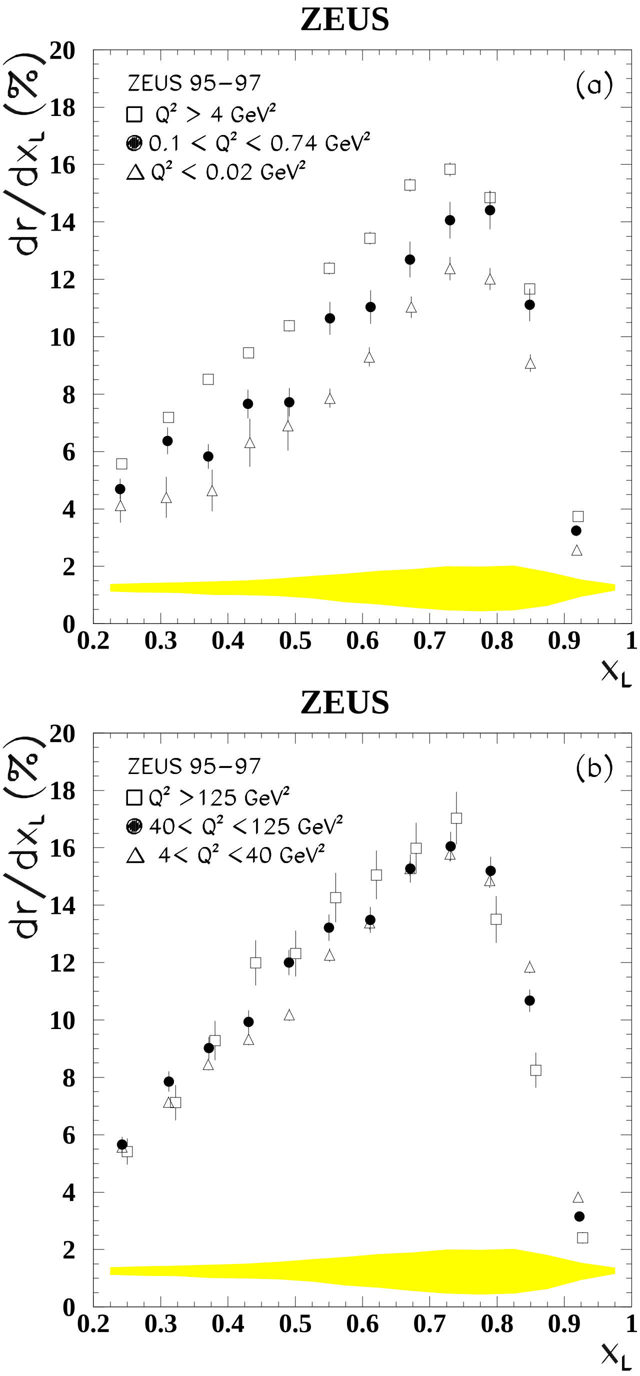

Figure 7: (a) Energy spectra, dr/dx_L, of neutrons with $\theta_n < 0.8$ mr in PHP, in the intermediate-Q^2 region and in DIS. The PHP data have a trigger-correction uncertainty of 2.5% which can move them relative to the intermediate-Q^2 and DIS data and, for $x_L > 0.52$, have an additional normalisation uncertainty of ±4%. (b) Energy spectra, dr/dx_L, of neutrons with $\theta_n < 0.8$ mr in DIS for three Q^2 selections. The points in (b) are offset slightly in x_L for improved visibility. The shaded bands show the systematic uncertainty due to the acceptance of the FNC. There is also a normalisation uncertainty of ±5 (±4)% for the PHP (intermediate-Q^2 and DIS) data. The energy-scale uncertainty of ±2% is equivalent to a stretch or compression along the abscissa. Not shown are the correlated normalisation uncertainties due to the energy-scale uncertainty given in Table 1.

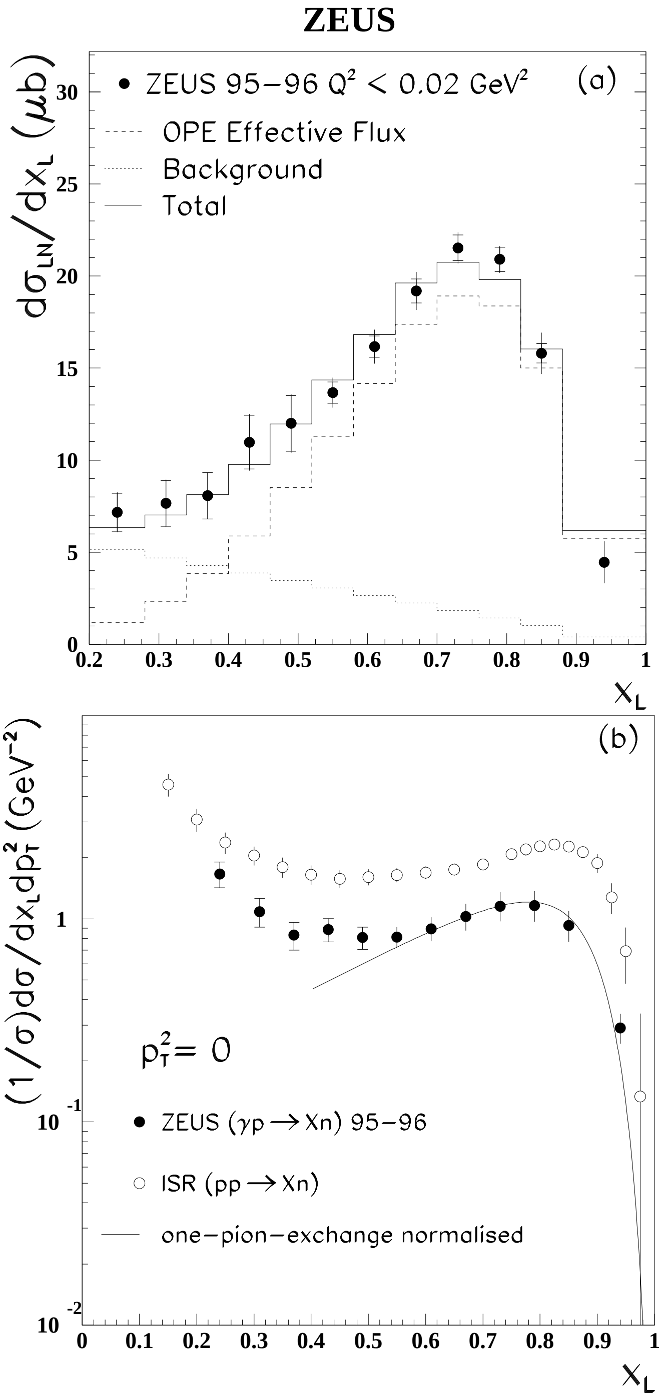

Figure 8: (a) The differential cross section for photoproduction of leading neutrons with $\theta_n < 0.8$ mrad, $d\sigma^{\mathrm{LN}}/dx_L$, at $\langle W \rangle = 207$ GeV. The solid histogram shows the result of a fit to the data using the OPE effective flux factor, f_{eff} of Eq. (8), shown as the dashed histogram, plus a background term $\propto (1 - x_L)$, shown as the dotted histogram. (b) The normalised cross section for $\gamma p \to Xn$ at $p_T^2 = 0$ (solid points). Also shown (open circles) are data from the ISR for $pp \to Xn$ [28]. The curve is the expectation of the one-pion-exchange model for hadron-hadron data scaled by 0.41. In both (a) and (b), the statistical uncertainties are shown by the inner error bars and the statistical and systematic uncertainties added in quadrature by the outer bars. Points for $x_L < 0.5$ ($x_L > 0.5$) are dominated by statistical (systematic) uncertainties (see Table 1).

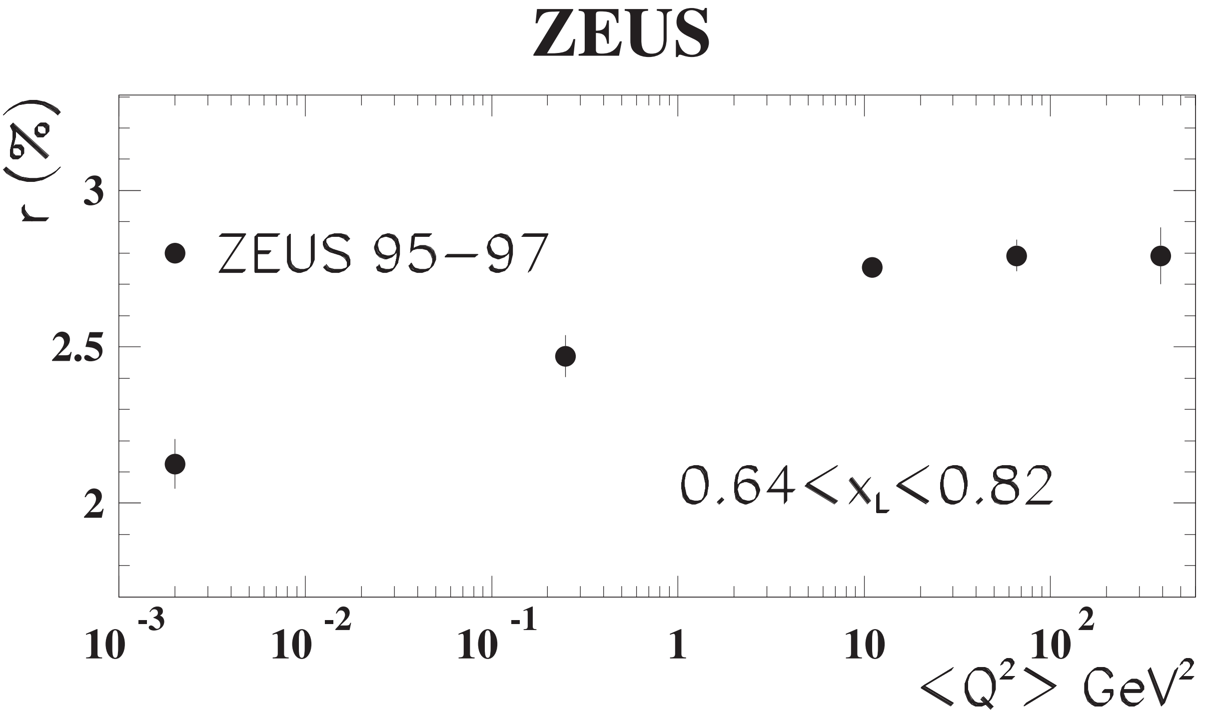

Figure 9: The ratio r for $0.64 < x_L < 0.82$ as a function of Q^2. The ratio r is plotted at the average value of Q^2 for the bin.

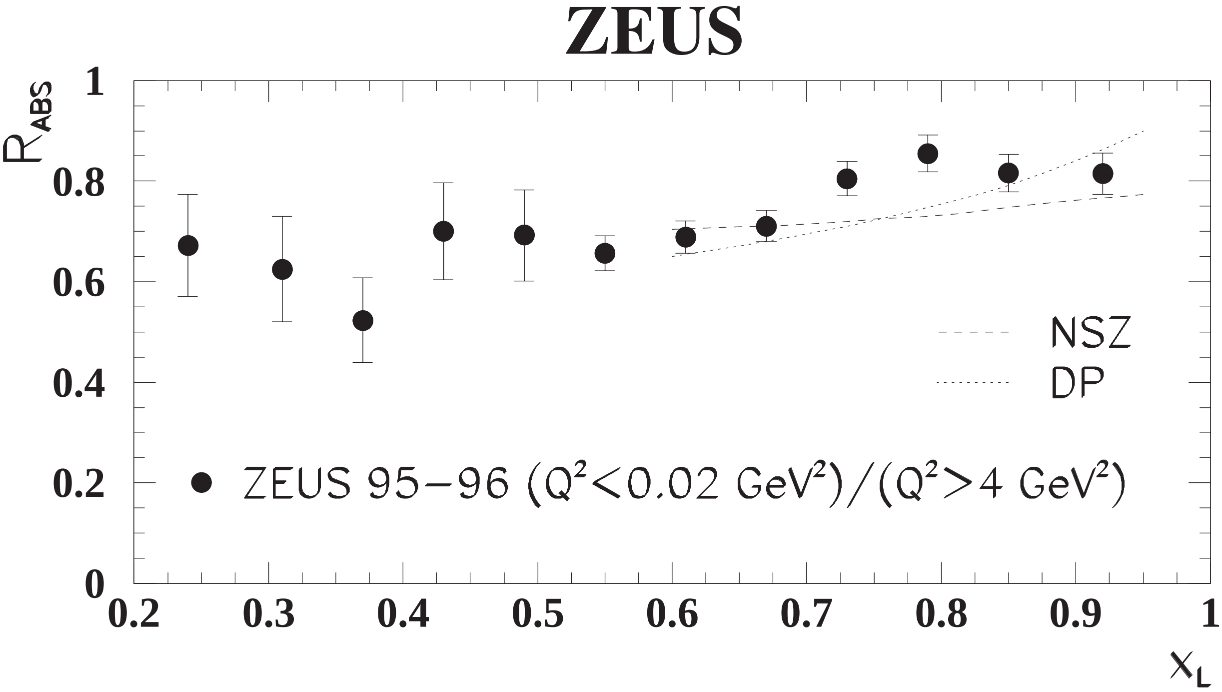

Figure 10: The ratio of the neutron energy spectrum in PHP to that in DIS. The curves labelled NSZ [35] and DP [36] are theoretical predictions of the effects of absorption, ($Q^2 < 0.02$ GeV^2)/($Q^2 > 10$ GeV^2). The vertical bars display the statistical uncertainties.

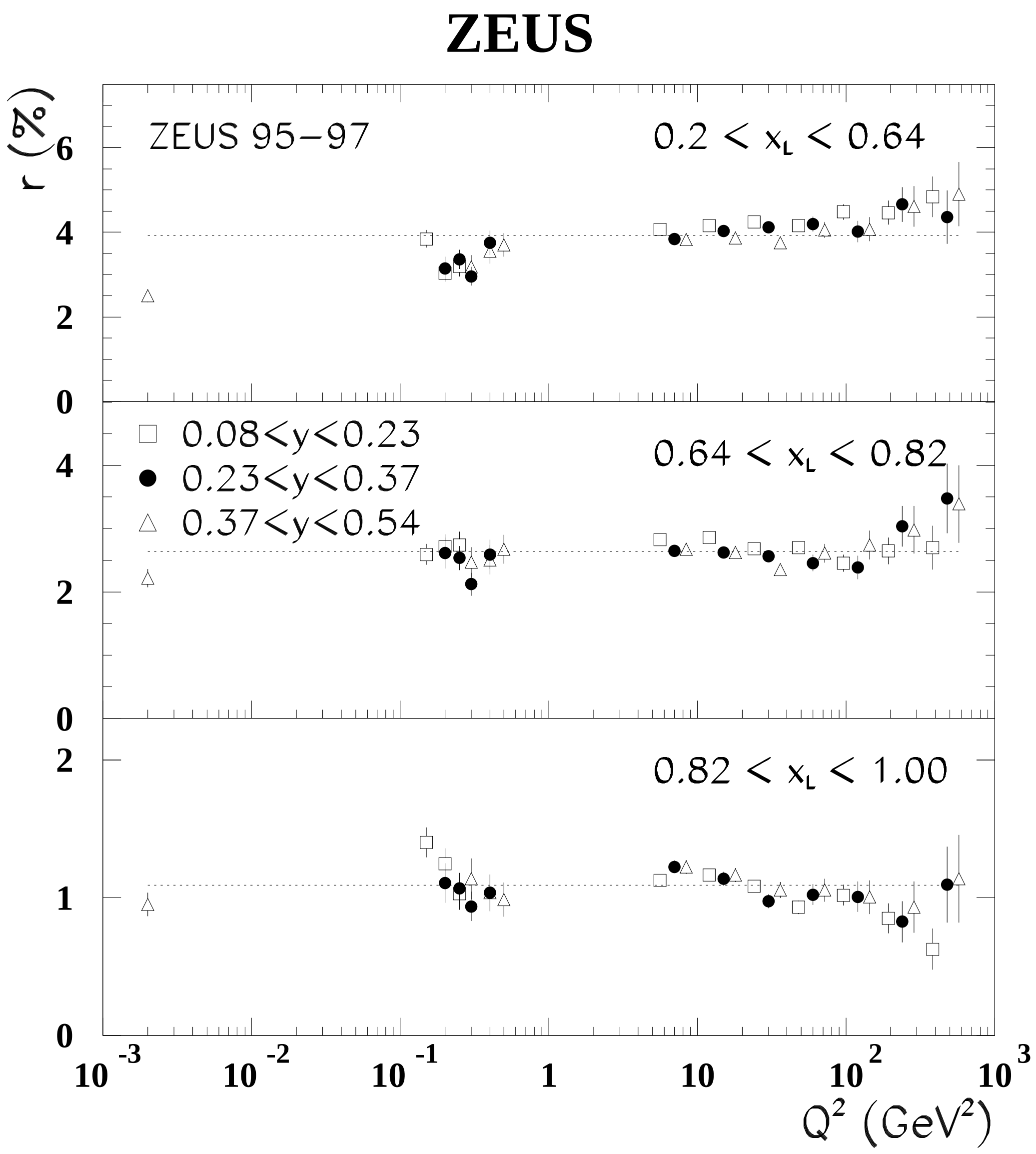

Figure 11: Neutron production ($\theta_n \leq 0.8$ mrad) as a fraction of the inclusive cross section in the PHP ($Q^2 < 0.02$ GeV^2), intermediate-Q^2 ($0.1 < Q^2 < 0.74$ GeV^2) and DIS ($Q^2 > 4$ GeV^2) kinematic regions as a function of Q^2 in bins of y and x_L. The PHP point is plotted at the average value of $\langle Q^2 \rangle = 2 \cdot 10^{-3}$ GeV^2 for the sample. The DIS points are offset in Q^2 for visibility. The horizontal dotted lines are plotted at the mean r of the plot to guide the eye. Only statistical uncertainties are plotted for the DIS and intermediate-Q^2 regions. For the PHP point, the uncertainty plotted is the statistical uncertainty added in quadrature with the PHP relative normalisation uncertainty.

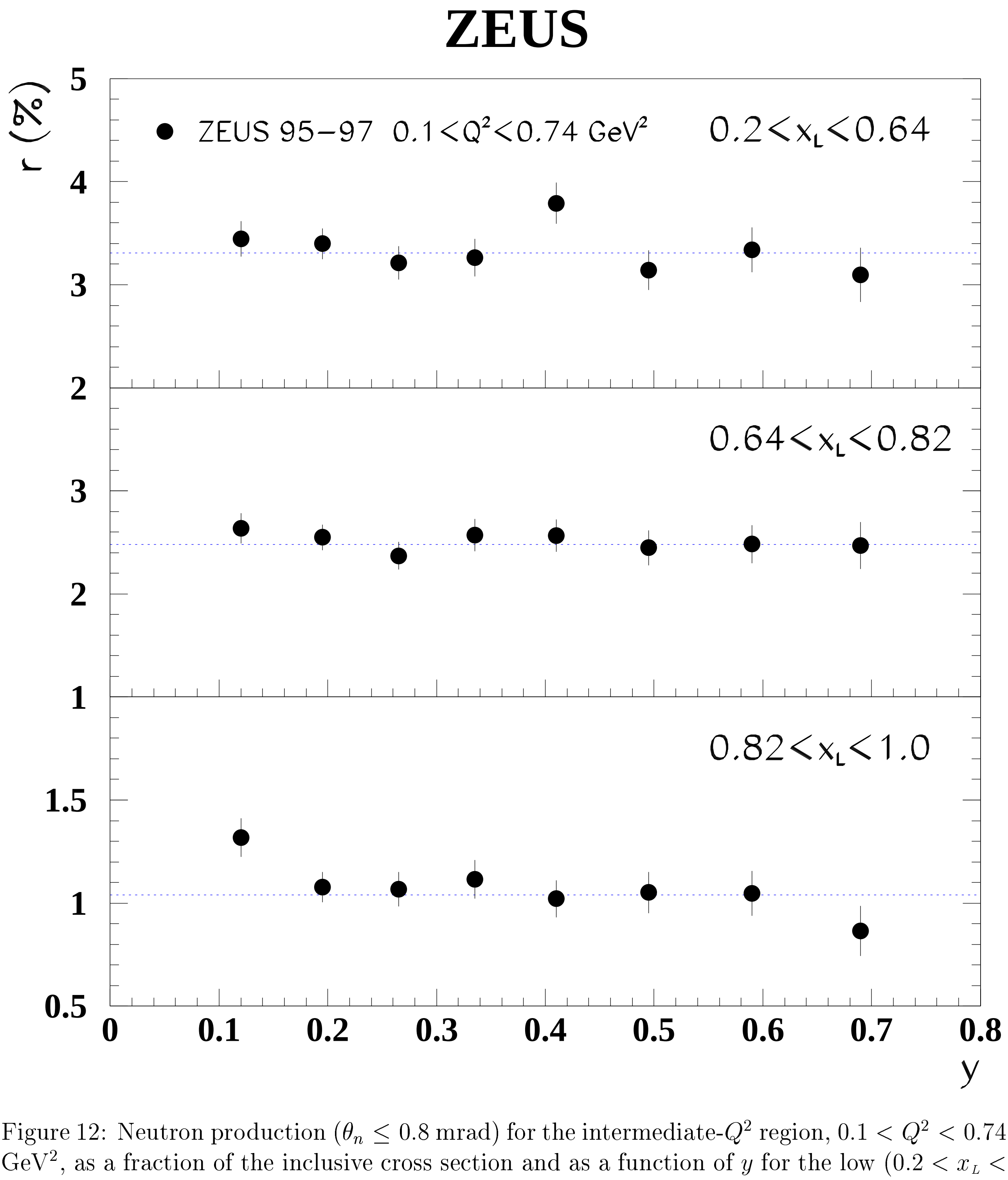

Figure 12: Neutron production ($\theta_n \leq 0.8$ mrad) for the intermediate-Q^2 region, $0.1 < Q^2 < 0.74$ GeV^2, as a fraction of the inclusive cross section and as a function of y for the low ($0.2 < x_L < 0.64$), medium ($0.64 < x_L < 0.82$), and high ($0.82 < x_L < 1$) x_L ranges. The dotted lines show the mean values of the ratio for each x_L range. Not shown are the correlated systematic uncertainties given in Table 1.

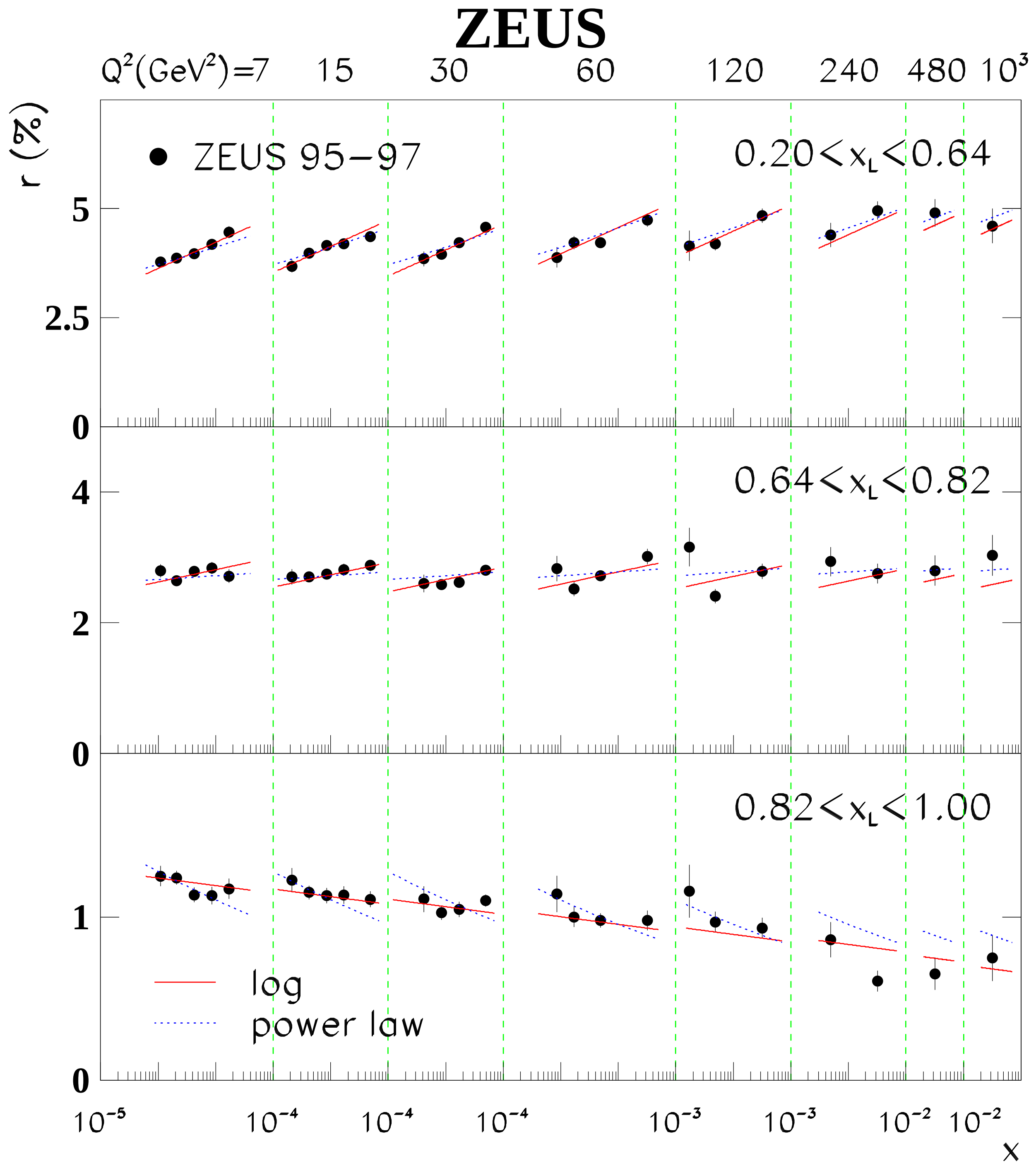

Figure 13: Neutron production ($\theta_n \leq 0.8$ mrad) for the DIS region, $Q^2 > 4$ GeV^2, as a fraction of the inclusive cross section and as a function of x for the low ($0.2 < x_L < 0.64$), medium ($0.64 < x_L < 0.82$), and high ($0.82 < x_L < 1$) x_L ranges, in the indicated bins of Q^2. The dotted lines show the result of fitting a power law in x to the ratio. The solid lines show the result of a fit to the ratio linear in both $\ln x$ and $\ln Q^2$, as discussed in the text. Not shown are the correlated systematic uncertainties given in Table 1.

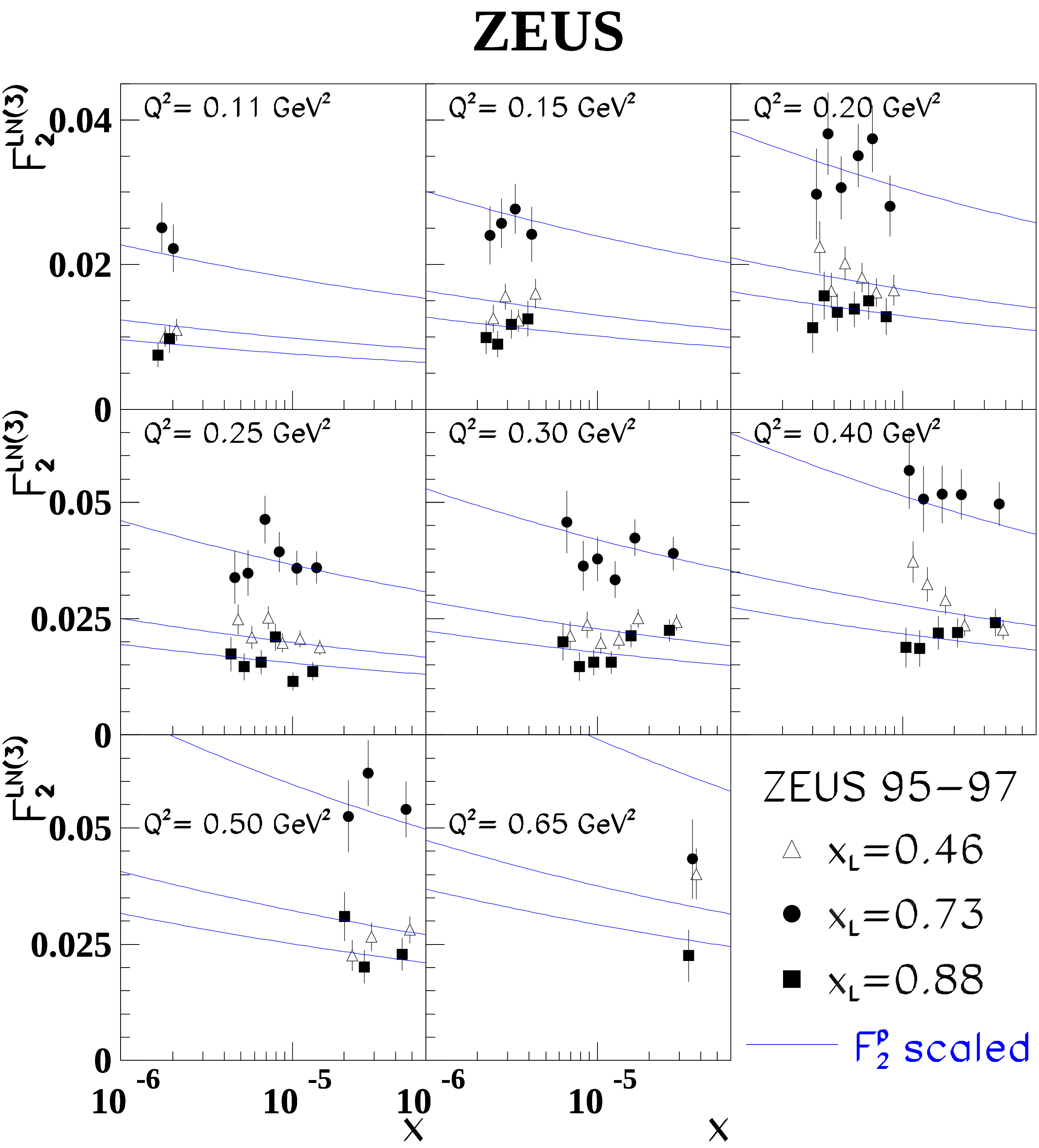

Figure 14: $F_2^{LN(3)}$ for $\theta_n < 0.8$ mrad for $0.20 < x_L < 0.64$, $0.64 < x_L < 0.82$ and $0.82 < x_L < 1.0$ in the intermediate-Q^2 region, $0.1 < Q^2 < 0.74$ GeV^2, as a function of x. The uncertainties shown are statistical added in quadrature with the uncertainties from the ZEUS Regge fit to F_2. The curves show $F_2(x, Q^2)$ for the proton scaled by the average value of r divided by the bin width Δx_L. Not shown is an additional correlated systematic uncertainty of ±8.8% from the acceptance, the energy scale and the overall normalisation uncertainty.

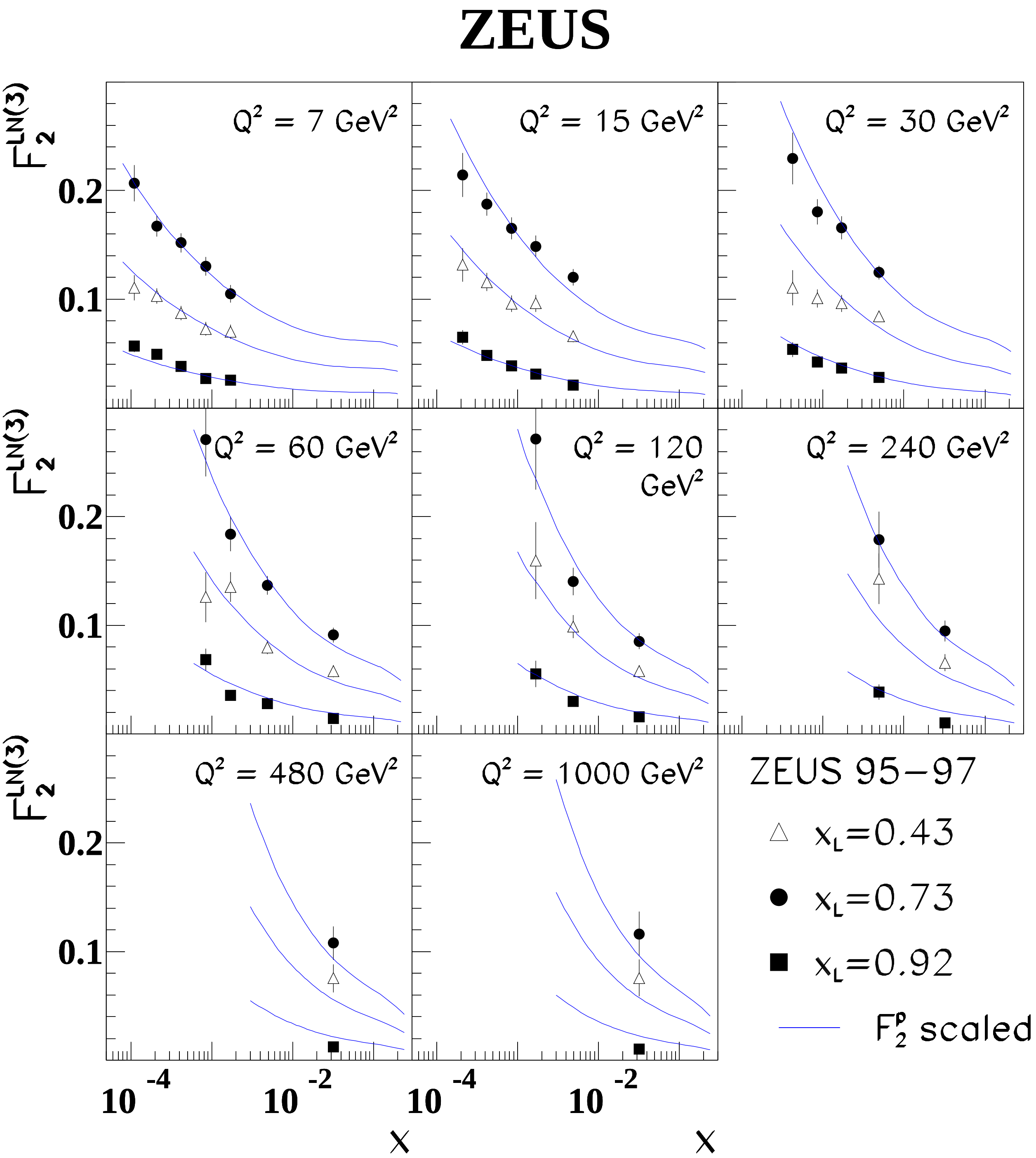

Figure 15: $F_2^{\mathrm{LN}(3)}$ for $\theta_n < 0.8$ mrad for $0.40 < x_L < 0.46$, $0.70 < x_L < 0.76$ and $0.88 < x_L < 1.0$ in the DIS region, $Q^2 > 4$ GeV^2, as a function of x. The uncertainties shown are statistical added in quadrature with the uncertainties from the ZEUS NLO QCD fit. The curves show $F_2(x, Q^2)$ for the proton scaled by the average value of r divided by the bin width Δx_L. Not shown is an additional correlated systematic uncertainty of ±8.8% from the acceptance, the energy-scale and the overall normalisation uncertainty.

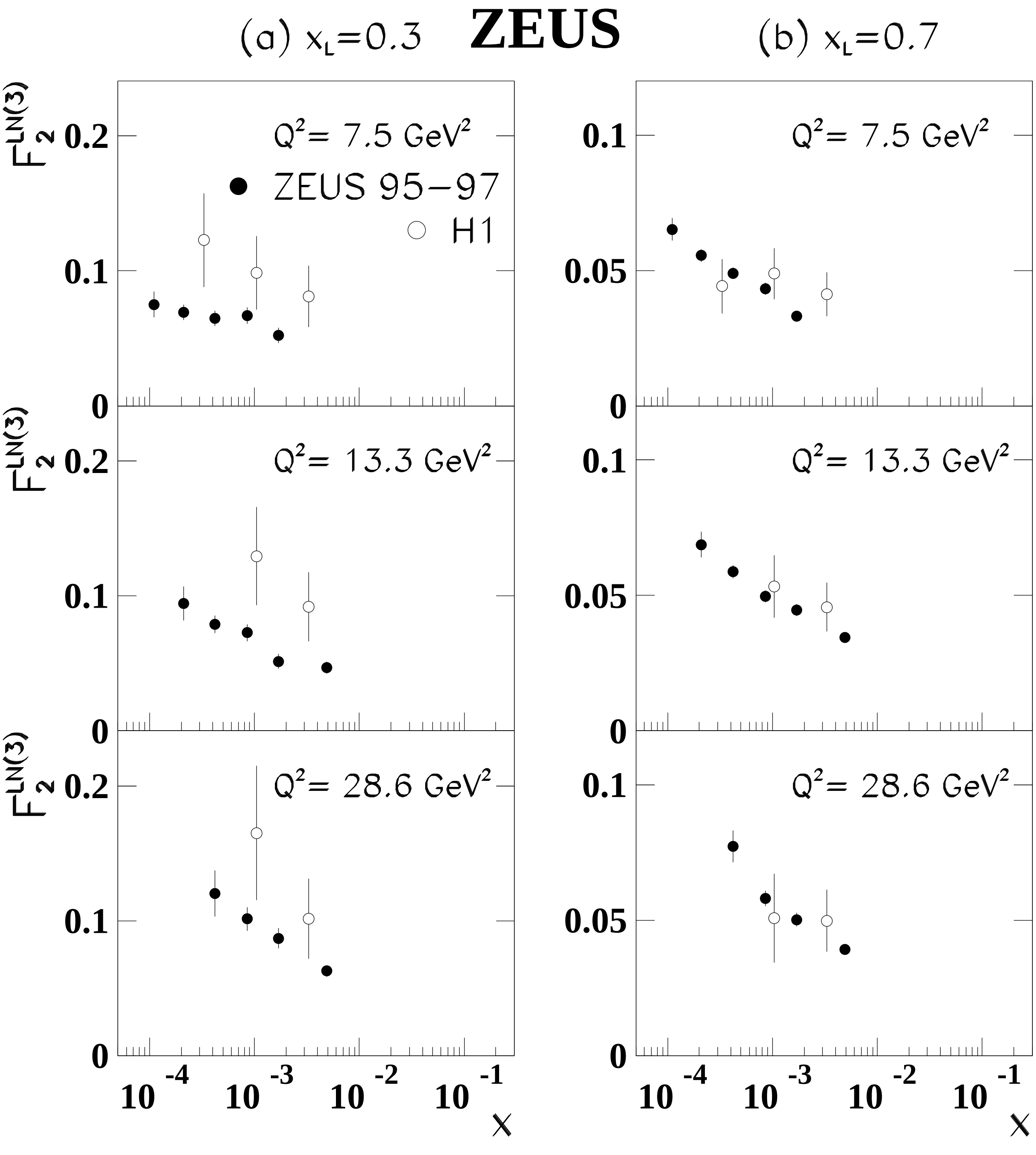

Figure 16: A comparison of the ZEUS and H1 values of $F_2^{\mathrm{LN}(3)}$ at (a) $x_L = 0.3$, where the p_T ranges covered by the two measurements coincide, and (b) $x_L = 0.7$, where the ZEUS data have been adjusted to the transverse-momentum range covered by H1, $p_T < 0.2$ GeV, using the form of Eq. (12). For ZEUS, the statistical uncertainties are added in quadrature with that from the ZEUS NLO QCD fit. A normalisation uncertainty of 6.7% (7%) remains at $x_L = 0.3$ (0.7) due to the acceptance, energy scale and overall normalisation uncertainties. For H1, the statistical and systematic uncertainties were added in quadrature. The uncertainties on the H1 points are dominated by the x_L-dependent uncertainties and so are strongly correlated. There is an additional normalisation uncertainty of 5.7% (not shown).

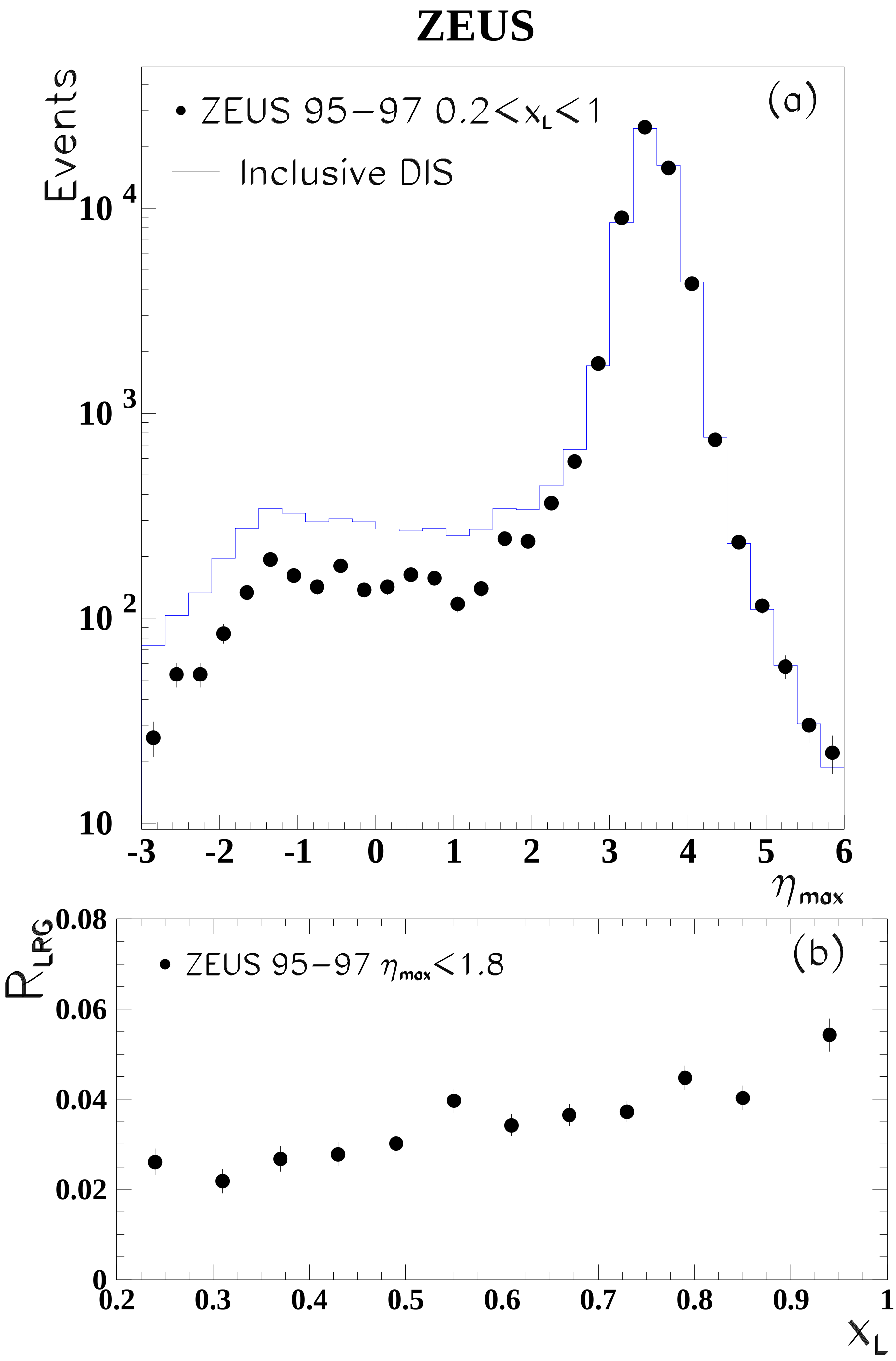

Figure 17: (a) The $\eta_{\max}$ distribution in DIS for neutron-tagged events (points). The histogram shows the inclusive $\eta_{\max}$ distribution, normalised to the neutron-tagged data for $\eta_{\max} > 1.8$; (b) the fraction, $\mathrm{R}_{\mathrm{LRG}}$, of leading neutron events with $Q^2 > 4$ GeV^2 passing the LRG criterion $\eta_{\max} < 1.8$, as a function of x_L.

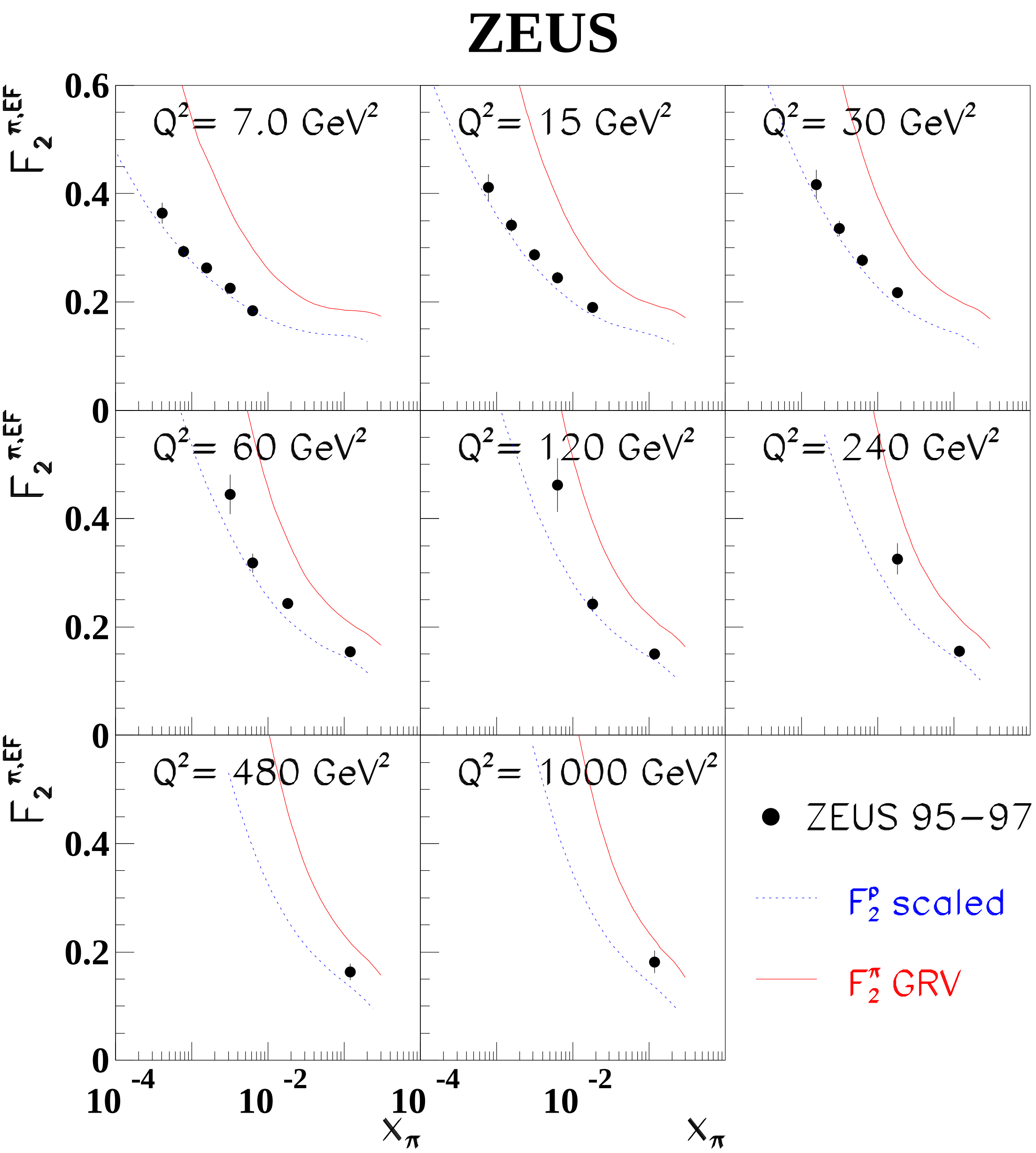

Figure 18: F_2^π as a function of x_π for the pion in bins of Q^2 determined for $0.64 < x_L < 0.82$, using Eq. (19). The pion flux used to determine F_2^π is the effective OPE flux (EF) used in hadron-hadron charge-exchange reactions, Eq. (8). The uncertainty shown on $F_2^{\pi,\mathrm{EF}}$ arises from the statistical uncertainty due to the leading neutron added in quadrature with the uncertainty on F_2. Not shown are the correlated systematic uncertainties given in Table 1. The dotted lines are $F_2(x, Q^2)$ for the proton, scaled by 0.361. The solid curves are F_2^π from the GRV parameterisation [76].

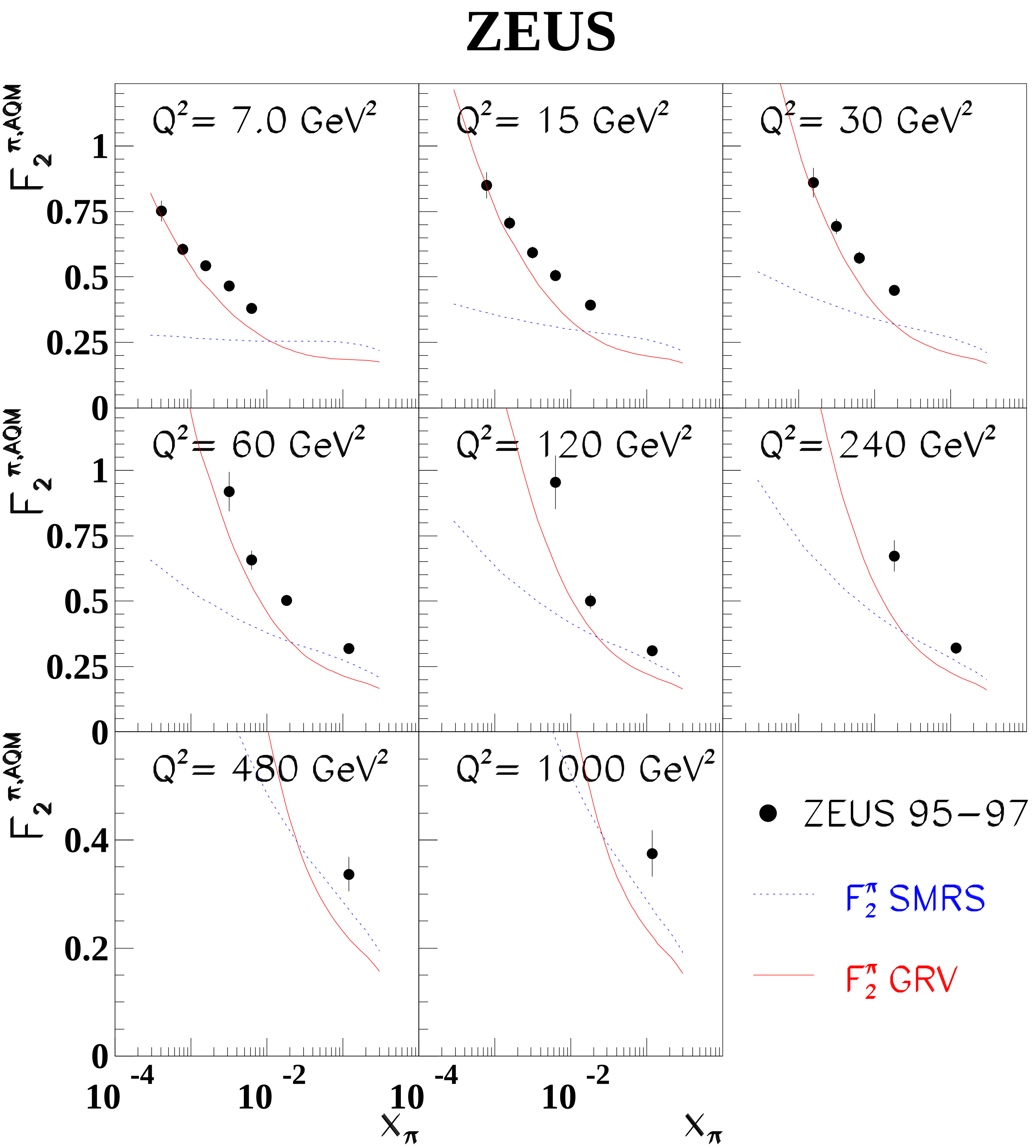

Figure 19: F_2^π as a function of x_π for the pion in bins of Q^2 determined for $0.64 < x_L < 0.82$. The pion flux used to determine F_2^π is the flux obtained using the additive quark model (AQM) of Eq. (21). The uncertainty shown on $F_2^{\pi,\mathrm{AQM}}$ arises from the statistical uncertainty due to the leading neutron added in quadrature with the uncertainty on F_2. Not shown are the correlated systematic uncertainties given in Table 1. The solid curves are F_2^π from the GRV parameterisation [76] while the dotted curves are from the Sutton *et al.* parameterisation [77].